Fall 2012

Probing physical properties at the nanoscale using atomic force microscopy

Lindsay Rachel Ditzler
University of Iowa

PROBING PHYSICAL PROPERTIES AT THE NANOSCALE USING ATOMIC FORCE MICROSCOPY

by

Lindsay Rachel Ditzler

An Abstract

Of a thesis submitted in partial fulfillment
of the requirements for the Doctor of
Philosophy degree in Chemistry
in the Graduate College of
The University of Iowa

December 2012

Thesis Supervisor: Assistant Professor Alexei Tivanski

ABSTRACT

Techniques that measure physical properties at the nanoscale with high sensitivity are significantly limited considering the number of new nanomaterials being developed. The development of atomic force microscopy (AFM) has lead to significant advancements in the ability to characterize physical properties of materials in all areas of science: chemistry, physics, engineering, and biology have made great scientific strides do to the versatility of the AFM. AFM is used for quantification of many physical properties such as morphology, electrical, mechanical, magnetic, electrochemical, binding interactions, and protein folding. This work examines the electrical and mechanical properties of materials applicable to the field of nano-electronics. As electronic devices are miniaturized the demand for materials with unique electrical properties, which can be developed and exploited, has increased. For example, discussed in this work, a derivative of tetrathiafulvalene, which exhibits a unique loss of conductivity upon compression of the self-assembled monolayer could be developed into a molecular switch. This work also compares tunable organic (tetraphenylethylene tetracarboxylic acid and bis(pyridine)s assemblies) and metal-organic (Silver-stilbizole coordination compounds) crystals which show high electrical conductivity. The electrical properties of these materials vary depending on their composition allowing for the development of compositionally tunable functional materials. Additional work was done to investigate the effects of molecular environment on redox active 11-ferroceneyl-1 undecanethiol (Fc) molecules. The redox process of mixed monolayers of Fc and decanethiol was measured using conductive probe atomic force microscopy and force spectroscopy. As the concentration of Fc increased large, variations in the force were observed. Using these variations the number of oxidized molecules in the monolayer was determined. AFM is additionally capable of investigating interactions at the nanoscale, such as ligand-receptor interactions. This work examines the interactions between the

enzyme dihydrofolate reductase (DHFR), a widely investigated enzyme targeted for cancer and antimicrobial pharmaceutical, and methotrexate (MTX), a strong competitive inhibitor of DHFR. The DHFR was immobilized on a gold substrate, bound through a single surface cysteine, and maintained catalytic activity. AFM probe was functionalized with MTX and the interaction strength was measured using AFM. This work highlights the versatility of AFM, specifically force spectroscopy for the quantification of electrical, mechanical, and ligand-receptor interactions at the nanoscale.

Abstract Approved: _____

Thesis Supervisor

_____

Title and Department

_____

Date

PROBING PHYSICAL PROPERTIES AT THE NANOSCALE USING ATOMIC FORCE MICROSCOPY

by

Lindsay Rachel Ditzler

A thesis submitted in partial fulfillment
of the requirements for the Doctor of
Philosophy degree in Chemistry
in the Graduate College of
The University of Iowa

December 2012

Thesis Supervisor: Assistant Professor Alexei V. Tivanski

Graduate College
The University of Iowa
Iowa City, Iowa

CERTIFICATE OF APPROVAL

_____

PH.D. THESIS

_____

This is to certify that the Ph.D. thesis of

Lindsay Rachel Ditzler

has been approved by the Examining Committee
for the thesis requirement for the Doctor of Philosophy
degree in Chemistry at the December 2012 graduation.

Thesis Committee: _____
Alexei V. Tivanski, Thesis Supervisor

_____
Amnon Kohen

_____
Leonard MacGillivray

_____
Christopher Cheatum

_____
Markus Wohlgenant

To my parents David and Gianna Ditzler, grandparents Robert and Loretta Huenefeld, and sister Sara Ditzler for there love and support.

Nothing exists except atoms and empty space;
everything else is opinion.
Democritus

ACKNOWLEDGMENTS

I am sincerely grateful to the following scientists and scholars for their collaboration, mentorship, and collegiality over the course of my academic career thus far: Dr. Amnon Kohen, Dr. Leonard MacGillivray, Dr. Christopher Pigge, Dr. Chandana Karunitilaka, Dr. Arundhuti Sen, Dr. Dejuan-Kresimir Bucar, Dr. Pradeep Kapadia, Dr. Jonas Baltrusaitis, Kristin Kester, Suman Ghorai, Thilini Raspunge, Holly Morris, and Mitch Chilton all collaborators at the University of Iowa; Dr. Audra Sostarecz, and Dr. Richard Kieft at Monmouth College. Also, thanks to the faculty and staff in the University of Iowa Department of Chemistry for facilitating research.

Thank you to my family and friends for supporting me through out this processes. You always brought me confidence and happiness when I doubted myself. Thank you to John Sander for helping me though every step of this process.

Finally, Dr. Alexei Tivanski, due to your instruction I have grown as a scientist and found confidence I didn't know I had. Thank you so much for pushing me to work hard and prove myself. I think your instruction has improved my scientific skills and abilities. Also, thank you to the Tivanski group members past and present. I have always enjoyed the collaborative environment that we have created in the group. I treasure my experiences and look forward to your future accomplishments.

ABSTRACT

Techniques that measure physical properties at the nanoscale with high sensitivity are significantly limited considering the number of new nanomaterials being developed. The development of atomic force microscopy (AFM) has lead to significant advancements in the ability to characterize physical properties of materials in all areas of science: chemistry, physics, engineering, and biology have made great scientific strides do to the versatility of the AFM. AFM is used for quantification of many physical properties such as morphology, electrical, mechanical, magnetic, electrochemical, binding interactions, and protein folding. This work examines the electrical and mechanical properties of materials applicable to the field of nano-electronics. As electronic devices are miniaturized the demand for materials with unique electrical properties, which can be developed and exploited, has increased. For example, discussed in this work, a derivative of tetrathiafulvalene, which exhibits a unique loss of conductivity upon compression of the self-assembled monolayer could be developed into a molecular switch. This work also compares tunable organic (tetraphenylethylene tetracarboxylic acid and bis(pyridine)s assemblies) and metal-organic (Silver-stilbizole coordination compounds) crystals which show high electrical conductivity. The electrical properties of these materials vary depending on their composition allowing for the development of compositionally tunable functional materials. Additional work was done to investigate the effects of molecular environment on redox active 11-ferroceneyl-1 undecanethiol (Fc) molecules. The redox process of mixed monolayers of Fc and decanethiol was measured using conductive probe atomic force microscopy and force spectroscopy. As the concentration of Fc increased large, variations in the force were observed. Using these variations the number of oxidized molecules in the monolayer was determined. AFM is additionally capable of investigating interactions at the nanoscale, such as ligand-receptor interactions. This work examines the interactions between the

enzyme dihydrofolate reductase (DHFR), a widely investigated enzyme targeted for cancer and antimicrobial pharmaceutical, and methotrexate (MTX), a strong competitive inhibitor of DHFR. The DHFR was immobilized on a gold substrate, bound through a single surface cysteine, and maintained catalytic activity. AFM probe was functionalized with MTX and the interaction strength was measured using AFM. This work highlights the versatility of AFM, specifically force spectroscopy for the quantification of electrical, mechanical, and ligand-receptor interactions at the nanoscale.

TABLE OF CONTENTS

LIST OF TABLES

LIST OF FIGURES

CHAPTER 1

INTRODUCTION TO ATOMIC FORCE MICROSCOPY

1.1 Introduction

Atomic Force microscopy (AFM) is one of the most versatile forms of microscopy for the characterization of physical properties. AFM uniquely offers higher resolution imaging capabilities owing to piconewton force sensitivity and nanometer positional accuracy.[1,2] The techniques ability to measure forces gives rise to various spectroscopic analyses, surface modifications, and molecular manipulations.[1] This high-resolution microscopy gained interest in fields across the scientific spectrum which includes applications in physics, materials science, chemistry and biology.[2] Today, AFM is used in the quantification of various physical properties; including: morphology,[3] electrical,[4] mechanical,[5] magnetic,[6,7] electrochemical,[8] binding interactions,[9,10] protein folding,[11] and many other properties at the nanoscale. The capabilities of AFM are ever-advancing to concur new problems; AFM has attained atomic resolution,[12] looked at single molecule kinetics,[13] and mapped protein placement with in cell walls.[14]

AFM was developed in 1986 to overcome the limitations of scanning tunneling microscopy (STM) and light microscopes.[15,16] STM consists of raster scanning a metal tip at a constant tunneling current in order to obtain an image.[16] STM is capable of reaching atomic resolution, and therefore, has provided great advancements beyond the resolution limitations of light microscopes.[16] However, atomic resolution is only attainable for highly conductive uniform samples under vacuum conditions.[15,16] In addition, STM lacks the ability to monitor the forces experienced by the sample.[15] AFM has overcame both of these obstacles by enabling the imaging of nonconductive

substrates while measuring forces with pN resolution.[15] Importantly, AFM, permits measurements to be performed under ambient conditions and solvent environments, thus, permitting the investigation of samples in stable environments (i.e. proteins in buffers).

1.2 Basics of AFM

AFM is primarily used to examine surface morphology, topography, as well as, measure interaction forces between the tip and sample (*i.e.* force spectroscopy). AFM consists of a sharp nanometer-sized probe attached to a springboard or V-shaped cantilever which is positioned over a surface deposited sample as shown in Figure 1.1a. Piezoelectric scanners control subnanometer movements in the x, y, and z dimensions, then images are compiled line-by-line as the sample is raster scanned. Additionally, a laser beam is focused on the back-tip of the cantilever to measure changes in cantilever deflection. Forces between the sample and the probe caused either by sample topography changes or the forces between the sample and the probe result in cantilever deflection. These changes in deflection are converted to force using Hooke's law, which allows for the quantification of forces on the pN scale and the employment of force spectroscopy.

The most common operating modes of AFM are contact and intermittent contact (or tapping) mode. Each operation mode has its own advantages and disadvantages. When contact mode is used, the cantilever is moved along the surface while maintaining a constant force, or cantilever deflection. The cantilever is displaced in the z-dimension using the piezoelectric device to maintain a constant force while line-by-line topographic images are collected. However, contact mode imaging exerts high local pressures and stresses, which can damage samples, therefore, is recommended for hard samples. Intermittent contact mode is better suited for soft samples such as biological materials.

The cantilever is excited into oscillations near the resonant frequency of the cantilever. The instrument then maintains constant oscillation amplitudes and taps along the surface. Akin to contact mode, any displacement in the z dimension is a measure of the height variation on the sample.

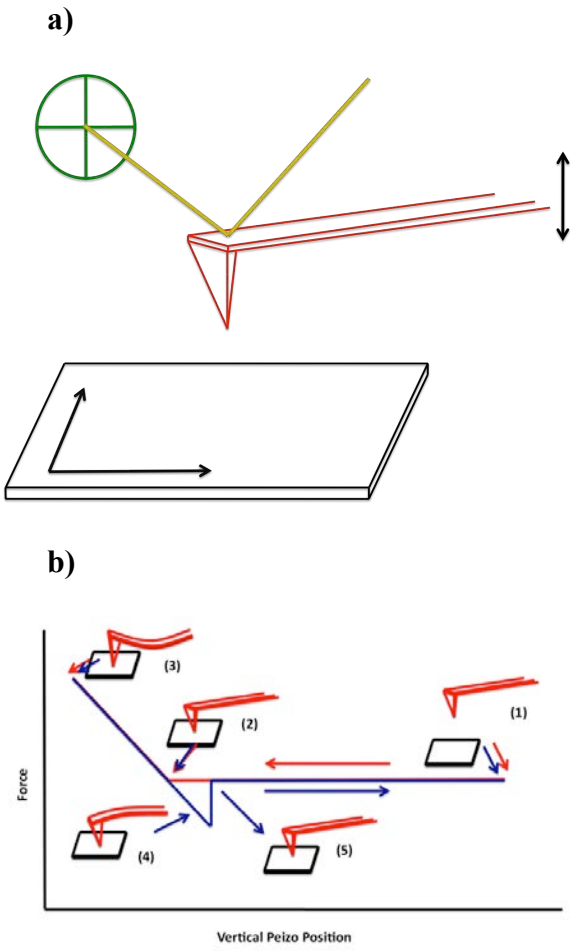

Figure 1.1. Basics of AFM a) Schematic representation of atomic force microscope components and b) representative force-distance measurement used in force spectroscopy.

Force spectroscopy is used to examine specific interaction forces between the tip and sample at forces as low as 10 pN. A typical measurement is diagramed in Figure

1.1b, where the tip starts far from the surface (1), comes in contact with the surface (2), applies a specific loading force to the sample (3), and then the process is repeated in reverse wherein the tip retracts from the surface. When an interaction between the tip and sample occurs step (4) is observed. At the point the tip overcomes the force holding it at the surface the tip breaks away form the sample (5), and retracts to its original position (1). Therefore, this process enables force spectroscopy and allows for the direct quantification of interaction strength between the probe and the sample.

Force spectroscopy can be applied at an air or a liquid interface (e.g. organic solvent or water). The results of force spectroscopy measurements vary greatly depending on the experimental conditions. For example, capillary adhesion forces (~10-20 nN) in air are often large enough to mask interactions such as van der waals (<0.04 nN),[17] hydrogen bonding (<0.2 nN),[18] and covalent bond forces (S-Au 1.4 nN and Si-C 2 nN).[19] If the capillary adhesion is larger than the interaction of interest then a liquid interface is applicable to allow detection of small interactions between the tip and sample. However, solvent selection is important to experimental success as solvent can change or mask the properties of materials.[20] Solvent selection was key in the experimental design of the work described within this dissertation.

1.4 Dissertation Outline

The scope of the dissertation examines the utility and application of AFM to investigate physical properties of nanomaterials; with primary focus on the electrical properties of monolayer systems (tetrathiafulvalene and decanethiol), organic semiconducting crystals (organic assemblies and metal organic complexes). Also, the electrochemical processes of mixed decanethiol and ferrocenyl-decanethiol were

investigated. Studies utilized conducting probe AFM (CP-AFM), which is capable of measuring force, bias, and currents simultaneously and independently. Using CP-AFM, electrical properties such as resistivity, conductivity, and electron mobility were measured. CP-AFM consists of a conductive probe and substrate, which is capable of measuring current as small at a few picoamperes. The final section of this dissertation focuses on measuring the strength of specific interactions between the ligand-receptor complex dihydrofolate reductase (DHFR) and methotrexate (MTX) using molecular recognition force spectroscopy. In a typical experiment, the AFM probe is functionalized with MTX and the enzyme forms a self-assembled monolayer. By allowing the tip and sample to interact the DHFR can bind MTX and subsequently the complex is ruptured allowing for the quantification of the interaction between the ligand and the receptor. Through these studies, and the future endeavors of this work, we hope to develop increased understanding of nanoscale interactions and processes.

CHAPTER 2
ELECTROMECHANICAL PROPERTIES OF TETRATHIAFULVALENE DERIVATIVES SELF-ASSEMBLED MONOLAYERS STUDIED BY CONDUCTING PROBE ATOMIC FORCE MICROSCOPY

2.1 Introduction

Extensive research has been done in the past to understand the charge transport of metal-self-assembled monolayers (SAMs)-metal junctions,[21-26] in particular utilizing organic molecular systems.[27-30] Among these molecular systems, conjugated organic molecules have found considerable attention due to their improved electrical conduction characteristics at the nanojunction. However, obtaining a reliable electrical contact to these nanometer scale SAMs can be practically challenging; nevertheless the conduction characteristics of conjugated molecules with a single and a double thiol linkers have been successfully investigated using recent CP-AFM studies.[31,32]

The most widely used method to fabricate these metal-molecule-metal junctions utilizes thiol linkers between two Au electrodes. It is well established that the efficiency of electron transport in molecular junctions[33,34] and the contact geometry with which the thiol links to the gold substrate are the key to the construction of a reliable molecular electronic device with efficient electrical conduction properties.[35] In particular, recent CP-AFM experiments demonstrated an enhanced electrical conduction for the double

---

This chapter was published in the *Journal of Physical Chemistry C* [Ditzler, and Tivanski (2010) Electromechanical Properties of Tetrethiafulvalene Derivatives Self-assembled Monolayers Studied by Conducting Probe Atomic Force Microscopy, 114, pp. 4429].

thiol, dithiocarboxylate, anchoring group linker on both sides of a biphenyl conjugated molecule relative to biphenyl with single thiol-gold contacts.[32] The authors suggested that the reason for the improved conduction is the stronger electronic coupling between the molecule and Au electrodes as a result of dithiocarboxylate anchoring group despite having a larger tunneling distance than the single thiol-gold contact. Li and coworkers[36] have noticed a similar trend in their computational studies and showed that the conductance enhancement *via* dithiocarboxylate is not only due to the better molecule-metal electrode overlap, but also due to the disparity in the electronic structure of this system as shown by their molecular orbital energy calculations.

Charge transfer properties of highly conductive tetrathiafulvalene (TTF) based molecular nanowires have been widely fabricated and characterized in the past. TTF has been an attractive candidate in these studies because of its high quasi-one dimensional electrical conduction properties and three stable redox-states.[37,38] A study using a combination of several surface characterization techniques suggests that SAMs of TTF derivatives on Au with various alkyl chain lengths have remarkably high conductive properties.[31] That work demonstrates a new type of indirect linkage between TTF and gold by two thiol groups where the opposite end of the molecule binds to a long alkyl chain and how the tilt of the loosely packed alkyl chains together with SAMs of TTF lead to large currents. Arrays of functionalized TTF derivatives have been successfully synthesized in the past,[39,40] however, not many systems have been utilized to fabricate the molecular wires other than the TTF itself.

In the present study, SAMs of symmetric TTF and 1-decanethiol were prepared and CP-AFM was used to probe the molecular conduction properties of the two films at

the molecular nanojunction. Decanethiol serves as a control as it is a well-studied molecule of a comparable length to the TTF molecular length. Electrical conduction characteristics of decanethiol have been extensively investigated in the past,[41,42] making it an ideal candidate for the comparison with the TTF.[31] The resistance of the TTF SAM and how it changes with the applied force were measured and, as expected, TTF showed significantly higher electrical conduction characteristics relative to the decanethiol with unique resistance-force dependence.

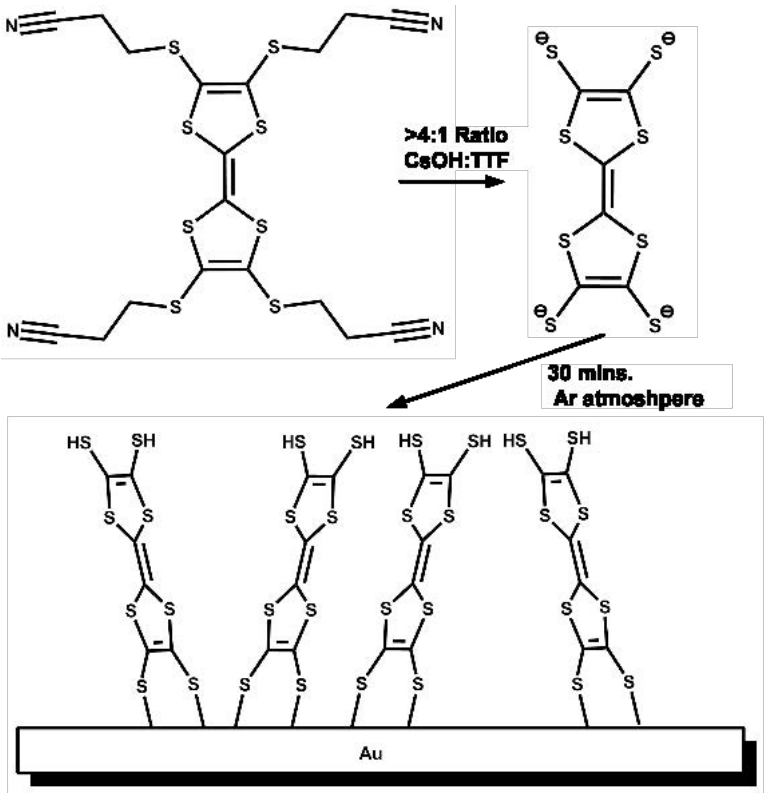

Figure 2.1. Preparation of the TTF thiolates and a schematic of the TTF SAM structure.

2.2 Experimental Section

2.2.1 SAMs Preparation

Ultraflat gold surfaces were fabricated using the template-stripping process.[43] Briefly, thermally evaporated gold surfaces on mica substrates (V-I grade, SPI Supplies, Westchester, PA) were glued face down using epoxy glue (Epotek 377, Epoxy Technology, Billerica, MA) on cleaned glass slides. The surfaces were then thermally cured in an oven for at least 2 hours at 150 °C. Finally, the ultraflat gold surfaces were obtained by stripping the mica with tetrahydrofuran. The resulting gold surfaces were rinsed in ethanol and dried in a stream of nitrogen gas. The root-mean-square roughness of the gold surfaces was typically less than 0.5 nm over 5 μm.

All 1-decanethiol (C_{10}, Sigma-Aldrich Corp., St. Louis, MO) self-assembled monolayers (SAMs) were formed by exposing the freshly prepared ultraflat Au surface to 2 mM C_{10} solution in ethanol for at least 12 hours and then were rinsed in ethanol and dried in a stream of nitrogen gas. The TTF derivative was synthesized according to a method developed by Svenstrup and co-workers.[40] The TTF derivative was prepared as thiolates by deprotecting the end groups (Figure 2.1) with an excess of cesium hydroxide monohydrate following the method developed by Becher and co-workers.[39,40] Briefly, cesium hydroxide monohydrate (Sigma-Aldrich, St. Louis, MO) and 18 μM TTF were dissolved in degassed ethanol (>4:1 mol ratio) and stirred for 30 minutes under a stream of argon gas. The Au substrate was then immersed into the solution for at least 30 minutes to form the monolayer, schematic shown in Figure 1. After the assembly, the substrate was rinsed with ethanol, sonicated for fifteen minutes to remove any physisorbed molecules and subsequently dried in a stream of nitrogen gas. All

preparations were performed at room temperature, and all samples were used immediately after the preparation.

2.2.2 Conducting Probe (CP) AFM Measurements

Topographic height imaging, force and electrical conduction measurements were performed in contact mode using a commercial atomic force microscope (MFP 3D, Asylum Research, Santa Barbara, CA) with conducting probe module (ORCA, Asylum Research, Santa Barbara, CA). Platinum-coated silicon cantilevers (Mikromasch, San Jose, CA) with a tip radius of curvature of ~35 nm and a reported spring constant of ~0.63 N/m were used in these experiments. The actual cantilever spring constants were determined with the built-in thermal noise method.[44] Cantilevers were cleaned in piranha solution (1:3 of 30% H_2O_2/98% H_2SO_4) for 2 minutes, rinsed in ultrapure water (> 18 MΩ•cm) for 1 minute followed by drying under vacuum. *Caution! Piranha solution is a very strong oxidant and is extremely dangerous to work with; gloves, goggles, and a face shield should be worn.*

Current-voltage (*I-V*) curves at different contact forces were collected by lowering the Pt-coated AFM probe onto different sample regions and measuring the electrical current through the monolayer junction as the surface bias was swept (typically at a rate of 0.6 V/s). A maximum absolute surface bias of around 1 V was used here as for the higher biases a noticeable sweep-to-sweep variation in the repeated measurements of current-voltage characteristics can be observed. Furthermore, a new clean tip was used in an event of decreased electrical conduction between the tip and the sample due to the deterioration of the probe after multiple measurements. The number of images collected was limited to preserve the conductive coating of the AFM probe. Almost all *I-V* curves

were collected at a loading force of 6 nN except for the study of the effect of applied force (pressure) on the electrical conductance, where loading forces up to 40 nN were applied. All experiments reported here were performed in an insulating bicyclohexyl solvent (99.0%, Fluka, Switzerland) in order to reduce water contamination and decrease the adhesion forces between the probe and the sample. The CP-AFM measurements were performed on three different samples of the TTF SAMs and three samples for of the decanethiol SAMs, using two tips per sample.

2.3 Results and Discussion

2.3.1 SAM Formation and Characterization

The formation of uniform self-assembled monolayers (SAMs) of both tetrathiafulvalene (TTF) and decanethiol (C_{10}) on ultraflat gold (Au) surfaces was verified using contact-mode AFM topographic height imaging. Figure 2.2 shows representative AFM height images of both TTF and C_{10} SAMs with various types of defects. Images were collected at approximately 2 nN tip loading force in bicyclohexyl solvent. Contact-mode imaging forces were limited to up to 2 nN to avoid damaging of the conductive coating on the AFM tip and to decrease tip contamination. Figure 2.2(a) shows uniformly bound TTF molecules onto the Au surface with no apparent aggregation on the sample surface. A number of pit-like defects, also commonly referred to as vacancy islands,[31] can be clearly visualized. The maximum height variation is ~1 nm, similar to the molecular length of the TTF molecule, 1.28 nm, thus implying a single monolayer coverage. The molecular lengths of the TTF and C_{10} were estimated using the Cambridge Structural Database. While a parallel orientation is possible, it is not expected to produce the uniform film with the observed height variation as shown in

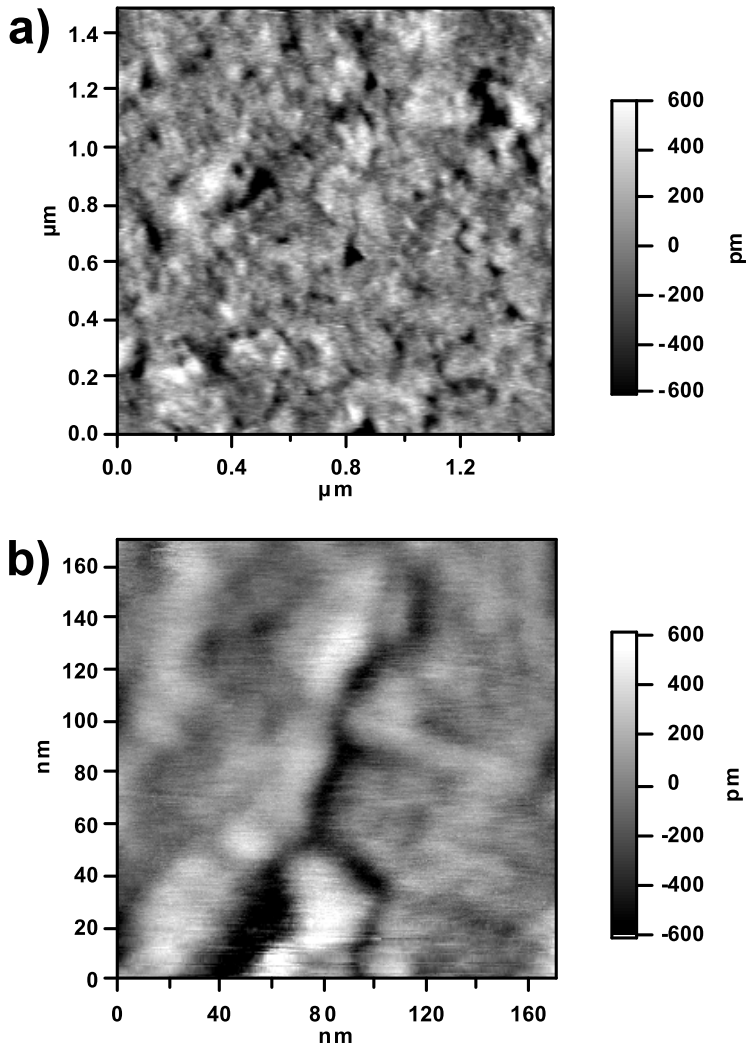

Figure 2.2. Constant-force AFM height images of a TTF (a) and a C_{10} (b) SAMs.

Figure 2.2 and goes against conductive measurements presented below where a significantly higher conduction would be observed if the molecules were to lie flat on the surface. Similar observations were previously reported for a series of double-thiol terminated norbornylogs[45] SAMs, where less than 10% of molecules were determined to orient parallel to the Au surface. Figure 2.2(b) shows height image for the C_{10} SAM

where domain formations are evident, which is a common characteristic of n-alkanethiol monolayers due to the tilt angle of the molecules.[46,47] Here, the domain boundary of C_{10} SAM can be clearly seen with the depth of approximately 1.2 nm. The molecular length of decanethiol is 1.56 nm and the molecular tilt angle (relative to the substrate normal) is ~30°,[48-51] hence, the observed height variations are consistent with the single monolayer of C_{10}. Finally, no signs of aggregation were evident for the C_{10} SAMs, similar to the TTF SAMs. Therefore, based on the above evidence, we conclude that both TTF and C_{10} SAMs are indeed forming uniform monolayers.

2.3.2 CP-AFM and Electrical Properties of TTF and C_{10} Monolayers.

Electrical conduction measurements were performed using CP-AFM by contacting the Pt-coated AFM probe onto different sample regions at different fixed tip loading forces, and measuring the current through the junction as the surface bias was swept. Multiple sample positions, free from any obvious defects, were chosen for conductive measurements and repeated current-voltage (*I-V*) curves at different loading forces over different sample regions were collected. The *I-V* curves were collected within ±1 Volt bias range. Higher biases were not applied because of an increased possibility of chemically modifying the molecule. Because of a finite AFM tip−SAM contact resistance, a nonzero loading force was required to make good electrical contact between the conductive probe and the SAM. The minimum tip loading force of 6 nN was found to be necessary to obtain reproducible current-voltage curves. All *I-V* curves recorded over different sample regions for the loading force of 6 nN had a similar shape with some variations in the current values. The current variations were less than one

order of magnitude and primarily originated from the variation in the number of molecules forming the junction on different SAMs positions. Therefore, an average of a number of *I-V* curves collected with the AFM tip contacting different sample positions was estimated to obtain a representative current-voltage characteristics for both molecular systems.

Figure 2.3 shows the averaged *I-V* curves for TTF (x) and C_{10} (□) SAMs in bicyclohexyl solvent under a fixed loading force of 6 nN. Each data point represents the mean value of current for a series of repeated measurements on different sample positions under a particular surface bias. The standard deviation of the averaged current values at different biases is similar to the size of the symbol. The measured *I-V* curves clearly indicate the TTF SAM is significantly more conductive than the decanethiol, which is expected for a conjugated molecule. Another readily observable feature is the smooth asymmetry of the *I-V* curve for the TTF SAM, where the current magnitude is 4.24 nA and -6 nA for the +0.5 V and -0.5 V surface biases, respectively. The asymmetry is likely due to the inherent asymmetry of the nanojunction because of the difference between metal-molecule contacts – covalent Au-S chemical bonds at the substrate side and weaker Pt-S bonding on the tip side. Additionally, as will be discussed in more details below, significant changes in the charge density inside the molecule can occur and its contribution to the potential profile across the junction can result in the asymmetrical response.[52,53] We note that unlike the TTF data, the *I-V* curve for the C_{10} SAM is symmetrical, consistent with numerous literature results,[31,41,42] even though the junction is asymmetrical. This apparent contradiction is most likely due to the difference in the potential tunneling barriers between the conjugated TTF and the decanethiol molecules.

To quantify these results, the *I-V* curves are compared to the Simmons model for nonresonant tunneling through metal-insulator-metal junction,[54-57] in which the temperature independent current *I* (in A) is given by

$$I = \frac{\sigma e^2}{2\pi h L^2}\left\{\left(\Phi_0 - \chi V\right)\exp\left[-K_e\alpha\left(\Phi_0 - \chi V\right)^{1/2}\right] - \left(\Phi_0 + (1-\chi)V\right)\exp\left[-K_e\alpha\left(\Phi_0 + (1-\chi)V\right)^{1/2}\right]\right\} \quad (1)$$

where K_e equals,

$$K_e = 4\pi L/h\left(2m_e e\right)^{1/2} \quad (2)$$

and m_e is the free electron mass, σ is the cross-sectional area of the tunneling junction, *L* is the length of the tunneling barrier, α is the unitless parameter, χ is the asymmetry factor, Φ_0 is the barrier height, and *V* is the applied surface bias. If the model of an electron tunneling through a rectangular barrier applies then the unitless parameter α equals 1. Deviations from this simple model are manifest as $\alpha \neq 1$, and can arise from a nonrectangular shape of the barrier and/or an effective mass ($m^* = m_e\alpha^2$) for the tunneling electrons through the junction.[54] The asymmetry factor χ is a measure of the different electrochemical potential shifts at the tip and the substrate due to the inherent asymmetry of the nanojunction.[52] If the nanojunction is symmetrical then $\chi = 0.5$ leading to a symmetrical *I*(*V*) theoretical dependence. Deviations from the symmetrical junction are manifest as $\chi \neq 0.5$ and can arise from the change in the charge density inside the molecule and inherent asymmetry of the junction.[52]

The cross-sectional area of the tunneling junction *σ* can be approximated as the mechanical contact area between the conductive probe and the sample. The contact area

can be estimated using a Hertzian elastic contact model.[58] According to the model, the mechanical contact radius a between a spherical tip of radius r penetrating into a uniform elastic film may be estimated as

$$a^2 = \left(\frac{Fr}{K}\right)^{2/3} \quad (3)$$

where F is the loading force and K is an effective modulus equaling,

$$K = \frac{4}{3}\left[\frac{1-\nu_{Pt}^2}{E_{Pt}} + \frac{1-\nu_S^2}{E_S}\right]^{-1} \quad (4)$$

and E_s, v_s, E_{Pt}, and v_{Pt} are the Young's modulus and the Poisson's ratio of the sample and the Pt-coated AFM tip, respectively. The Poisson ratio for most materials is between 0.25 and 0.5,[31,58] and thus assuming $v_{Pt} \approx v_s \approx 0.33$, an effective modulus can be approximated as $K=1.5E_{Pt}E_s/(E_{Pt}+E_{Pt})$. Since the same 6 nN loading force was used to obtain $I(V)$ curves for both molecular systems, the contact area between the AFM tip and SAMs is expected to be the same if one assumes similar elasticity modulus E_s for both films. Although appropriate measured values for elasticity modulus are not available, assuming E_{Pt}=170 GPa,[54] E_s=7 GPa[31,59], and tip radius of curvature as 35 nm, the contact area between the tip and both SAMs for the loading force of 6 nN would be 23.8 nm^2. Assuming the uncertainty (standard deviation) in the elasticity modulus of the SAM is ±2 GPa and the deviation in the tip radius of curvature between different AFM probes is ±5 nm, the propagation error analysis can be used to estimate the uncertainty (standard deviation) in the contact area to be ±5.3 nm^2. Therefore, the cross-sectional area of the tunneling junction σ is estimated to be 23.8 ± 5.3 nm^2. The lengths of the potential barriers for TTF (L) 1.28 nm and C_{10} (L) 1.56 nm were estimated from the Cambridge Structural Database molecular lengths.

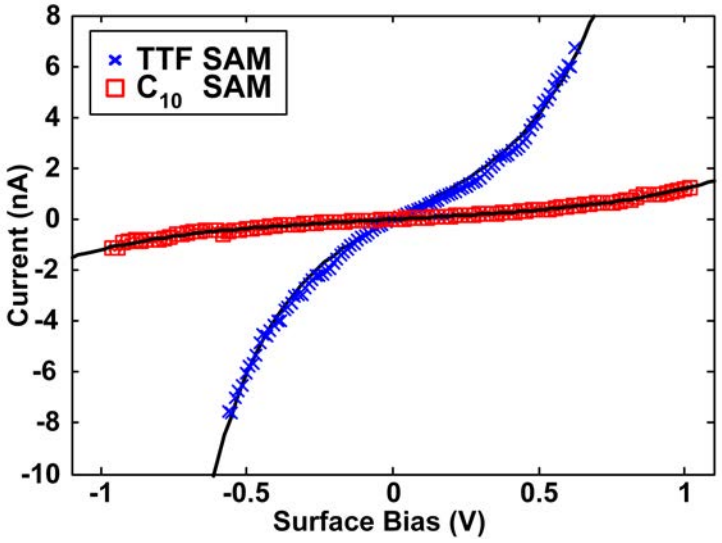

Figure 2.3. Averaged current-voltage (*I-V*) curves for TTF (x) and C_{10} (□) SAMs in bicyclohexyl solvent under a fixed loading force of 6 nN. Each data symbol represents the mean value of current at a particular surface bias and the solid lines are fits to the Simmons model.

The averaged *I-V* curves for the TTF and C_{10} SAMs were fit using eq. 1, by adjusting three parameters Φ_0, α and χ. Since the *I-V* curve for the C_{10} SAM is symmetrical, the χ value has been constrained to χ =0.5 and only two parameters were used to fit the C_{10} SAM data. In the case of the TTF SAM, the unitless parameter α was constrained to α = 1, as otherwise physically unreasonable fitted α value slightly over 1 was found. Thus, only two parameters, Φ_0 and χ, were used to fit the *I-V* curve for the TTF SAM. The solid lines in Figure 2.3 represent the best-fit curves. The parameters obtained from the fits are Φ_0 = 0.72 eV, α = 1 and χ = 0.44 for the TTF SAM and Φ_0 = 1.51 eV, α = 0.67 and χ = 0.5 for the C_{10} SAM. As expected, the potential barrier for the conjugated TTF system is significantly lower than that for the C_{10} SAM. The tunneling

decay coefficient, β_0 for both C_{10} and TTF SAMs can be obtained from the fitted values for the unitless parameter α and the tunneling potential barrier Φ_0 using equation 5.[32]

$$\beta_0 = \frac{2(2m_e)^{1/2}}{\hbar}\alpha\sqrt{\Phi_0} \quad (5)$$

The calculated β_0 values are 8.5 nm^{-1} and 8.7 nm^{-1} for the C_{10} and TTF SAMs, respectively. It is important to mention that the Simmons model oversimplifies the charge transport mechanism as it ignores important contributions such as superexchange or hoping mechanisms.[20,60-64] This is especially relevant if the applied bias becomes comparable with the tunneling potential barrier, as in the case for the TTF junction. Nonetheless, a number of literature reports have shown that fitting the Simmons model to the *I-V* data instead of the current-tunneling distance data produces parameters in good agreement with those obtained from the current-distance fits.[63] The tunneling decay coefficient values for the C_{10} and TTF junctions obtained in the present study are consistent with the values reported in the literature.[61,62] Specifically, the tunneling decay coefficient estimated for the TTF is comparable to the values reported for different conjugated molecules with various molecular lengths. [61] The relatively low tunneling decay coefficient of the TTF and low tunneling potential barrier indicate that the TTF SAMs possess efficient charge transport characteristics making them promising building blocks for molecular wires.

All *I-V* curves for both molecular systems display linear current-voltage region within ±0.2 V surface bias, consistent with the Ohm's law. A straight line fit the linear Ohmic region between -0.2 to 0.2 V and the SAM resistance value was calculated as the inverse fitted slope value. Repeated *I-V* measurements at various sample positions were taken for both the TTF and C_{10} SAMs and the resistance value for each measurement was

calculated in this bias range. Figure 2.4 shows a histogram plot of the TTF SAM resistance values for all *I-V* measurements obtained at the loading force of 6 nN in bicyclohexyl solvent. The histogram was generated with the bin size of 0.04 GΩ. The TTF SAMs resistance histogram shows the distribution of the resistance measurements, the mean resistance for all the measurements is $\langle R_{TTF} \rangle = 0.21 \pm 0.01$ GΩ. A similar analysis has been performed for the C_{10} SAM and the mean resistance value has been estimated as $\langle R_{C10} \rangle = 1.6 \pm 0.37$ GΩ. The mean resistance value obtained for the decanethiol SAM is in a reasonable agreement (~6 lower) with the value reported by Wold *et al*.[53] in cyclohexane solvent. The deviation is likely due to the differences in the tip radii of curvature used and in the magnitude of the loading force.

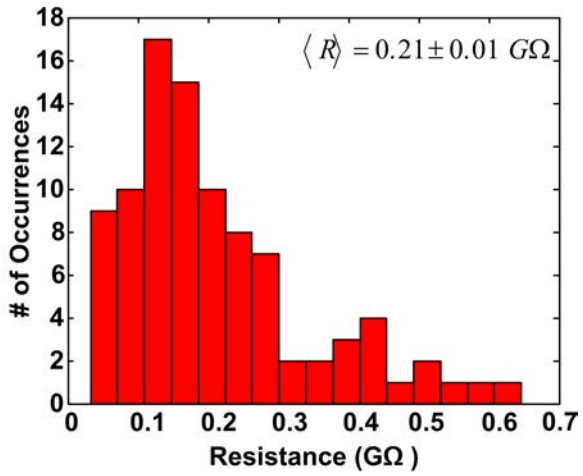

Figure 2.4. Resistance distribution for the TTF SAM collected at the loading force of 6 nN.

The measured mean resistance values for both molecular systems are approximately 1.6 and 0.21 GΩ for the C_{10} and TTF junction, respectively. The number of molecules in direct mechanical contact with the AFM probe in the junction is different for

these two samples due to the difference in the E_{Pt}, E_s, and surface coverage. Thus, it is valuable to scale the SAM resistance value to a single molecule. The surface coverage for a closely packed C_{10} SAM is approximately 0.25 nm^2 per molecule.[62] In the case of the TTF SAM, the distance between two thiol groups of the TTF unit is 0.33 nm,[31] which corresponds to an area per molecule of 0.34 nm^2. This number is consistent with that previously used for other molecular systems with similar molecule-gold contact geometry.[31,45] If close packing is assumed then the scaled single molecule resistance would provide an upper limit to the resistance. By using the above estimates for the contact area at a loading of 6 nN and the area per molecule, and assuming close packing for both SAMs, there are 95 ± 20 and 70 ± 15 molecules forming the junction for the C_{10} and TTF SAMs, respectively. The number of molecules can be used to scale measured SAM resistance to a single molecule resistance by multiplying the mean SAM resistance with the appropriate number of molecules. The single molecule resistance obtained by using this approach is 950 ± 22 GΩ for the C_{10} molecule and 14.7 ± 3.4 GΩ for the TTF molecule. Here, the error is dominated by the uncertainty in the determination of the contact area, as described above. The molecular resistance value estimated for the TTF molecule is in good agreement with a recent CP-AFM study[31] on a similar molecular system, where the single molecule resistance of 25.7 GΩ was measured. The higher molecular resistance observed in that work is likely due to the presence of relatively long alkyl chains at the end of the TTF unit, which form an insulating layer between the AFM probe and the TTF units thus leading to the increase in the resistance. It is worthwhile to mention that such scaling to a single molecule resistance may differ from the actual single molecule measurements due to differences in molecular environment and molecular

interactions. In the case of the actual single molecule measurements, the charge transfer mechanism is predominantly through-bond, while the conductive measurements that involve an ensemble of molecules often involves a combination of through-bond and through-space charge transport.[20]

By modeling TTF molecules as cylinders with a cross-sectional area of 0.34 nm^2 and a length s = 1.28 nm, the molecular resistivity can be estimated from the measured single molecule resistance. The TTF molecule displayed resistivity of 390 Ω•cm. The value is comparable with the intrinsic resistivity of bulk germanium (~65 Ω•cm). This result indicates a remarkable conductivity for an organic molecule suggesting that the dithiol contact geometry such as that for the TTF unit provides a better overlap of the electronic wave functions of the molecule and substrate. Previous studies[31,32] have also reported that a significant enhancement of the electrical conduction can be obtained by using contact geometries other than single thiol-gold chemical bond. Current studies provide another example of such alternative contact geometry and suggest that the molecular systems based on the TTF unit can be used as efficient metal-molecule interconnects with efficient charge transfer properties.

Since all the measurements reported so far were performed in an insulating bicyclohexyl solvent, it is important to relate these measurements to the ambient environment. This permits quantification of an effect the surrounding solvent medium plays on the electrical conduction through the organic SAMs. Therefore, the CP-AFM measurements were also performed in air using the same loading force of 6 nN. The resistance for both SAMs in air was measured and the results indicate that both the TTF and the C_{10} SAMs exhibit significantly larger resistance in air as compared with the

bicyclohexyl solvent. The mean resistance values obtained for the TTF and C_{10} SAM in air at the loading force of 6 nN are 0.55 ± 0.08 GΩ and 9.7 ± 0.12 GΩ, respectively. The resistance obtained for the decanethiol SAM in air is again consistent with the values reported by Wold et al[42] and Engelkes et al[41] but as mentioned earlier, the slight variations are due to the different experimental conditions. The increase in the measured resistance is somewhat surprising, as one would expect the opposite trend. This is due to the presence of the capillary adhesion force of ~7-10 nN that adds to the applied loading force of 6 nN and thus making the interaction force between the AFM probe and the sample larger than in solvent where the capillary force is practically eliminated. The increase in the interaction force increases the contact area and hence number of molecules forming the junction. Thus, lower SAM resistance or higher electrical conduction is expected. The fact that the opposite trend was observed points to a formation of a contamination layer with a variable thickness as has been investigated by Engelkes and coworkers.[41] Therefore, it is evident that the experimental medium plays a vital role and can sometime change the contact resistance by orders of magnitude as suggested by Gosvami et al.[60] The use of an organic solvent (bicyclohexyl in this case) decreases the possibility of forming a sample contamination layer and also significantly decreases the capillary forces due to water condensation, thus allowing us to measure molecular resistance under low stress region.

Finally, as the CP-AFM allows the electrical measurements under controlled applied load, an effect of the loading force on the SAMs resistance was measured. A series of repeated *I-V* measurements under different loading forces, namely at 6, 12, 19.6, 26.6, 33.3 and 40 nN, were performed to determine how the loading force influences the

electrical conduction of these molecular junctions. To avoid a possibility of irreversibly damaging the molecular SAM structure with force that can effect subsequent measurements, the *I-V* curves were measure at different force sequences at various SAM locations, i.e. experiments were performed from the lowest loading force up to the highest, then on a different sample spot from the highest force to the lowest as well as at various random combinations. Measured current values were comparable within similar bias ranges and same applied loading forces with some degree of variation presumably due to the variation in the number of molecules forming the nanojunction. All *I-V* curves displayed functional shapes similar to that shown in Figure 2.3. Similar to the resistance estimates at the loading force of 6 nN, straight lines fit the linear Ohmic regions and the inverse slope was used to estimate the junction resistance.

Figure 2.5 shows the averaged junction resistance *versus* loading force for the C_{10}(a) and the TTF(b) SAMs. Symbols correspond to the averaged resistance values and the error bars represent the standard deviation of the mean for a series of ~50 repeated *I-V* measurements at different sample regions under a particular loading force. A clear increase in the TTF junction resistance is observed for the loading forces between 6 and 26.6 nN with the decrease in the resistance at 33 nN. The effect is highly reproducible and, as mentioned previously, special care was given to insure that the effect is not an artifact. As will be discussed below, the effect is unusual and typical molecular systems display an opposite trend. The dependence observed for the TTF SAM is in sharp contrast with the C_{10} SAM, where a decrease in the junction resistance with an increase in the loading force is observed, as can be seen in Figure 2.5a. The inset in Figure 2.5a shows log-log plot of the C_{10} junction resistance *versus* loading force. A clear power-law

scaling regime is observed, which can be fit by a straight line (solid lines in Figure 5a), with the fitted resistance scaling as $(\text{force})^{-1.88}$.

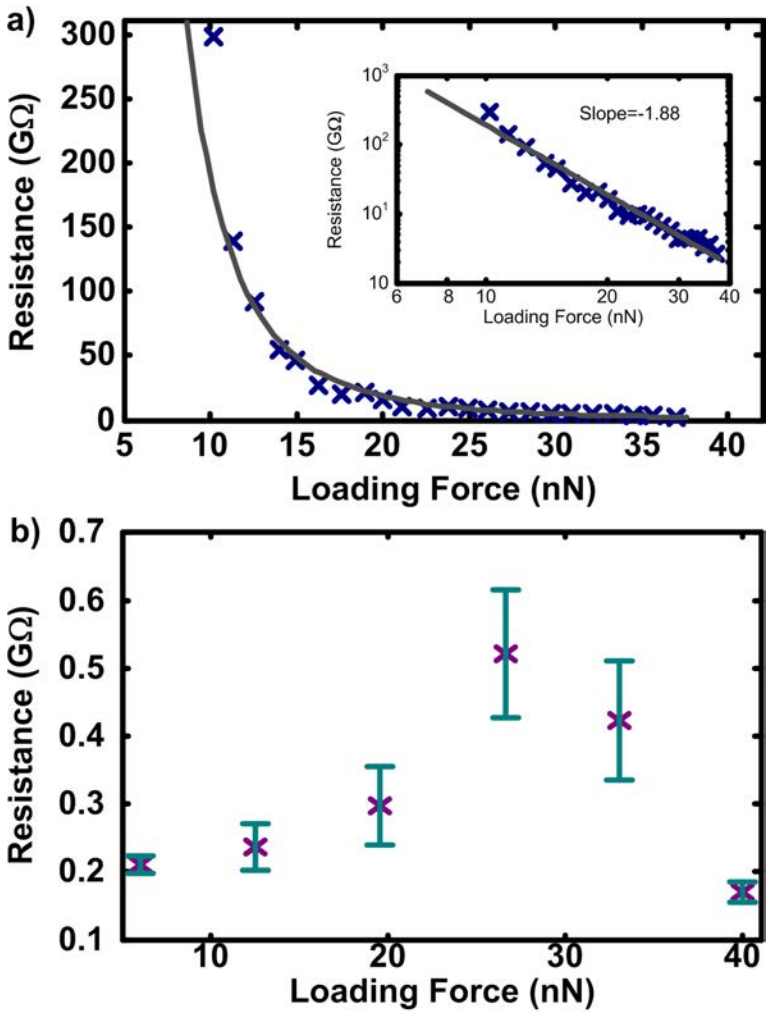

Figure 2.5. Plots of averaged junction resistance *versus* loading force for a TTF (a) and a C_{10} (b)monolayers. Crosses are averaged data and the error bars represent the standard deviation of the mean for a series of ~50 repeated measurements at different sample regions under a particular loading force. The inset shows log-log plot of the C_{10} junction resistance versus loading force. The power law exponent is determined as ~ - 1.88 from the slope of a linear fit.

Possible factors which can change the observed junction resistances under applied interaction force are: (a) change in the contact area between the AFM tip and the sample,

(b) change in the tunneling distance between two electrodes due to film compression, and (c) intra- and interchain order of the molecular film. As the loading force increases, the contact area will increase and the tunneling distance will decrease. Therefore, factors (a) and (b) will always lead to the decrease in the junction resistance with an increase in the loading force. The change in the molecular film structure under compression can both lead to a decrease or an increase in the junction resistance.[20] In the case of the C_{10} SAM, the observed power law decrease in the resistance with an increase in the loading force can be quantified by estimating an increase in the contact area and the decrease in the tunneling length as decanethiol molecules tilt in response to the compression.[20] As the chain-to-chain coupling between alkanethiol chains is relatively low, the interchain charge transfer mechanism in alkanethiol SAMs is not efficient within the range of applied forces studied.

Although we do not have *direct* proof of the molecular mechanism of the observed increase in the junction resistance for the TTF SAM as the loading force increases, we argue it originates from the change in intermolecular interactions as AFM probe compresses the molecular film. For conjugated molecular SAMs such as the TTF, intermolecular interactions (e.g., π-π interaction) are likely to contribute to the electrical conduction.[64] A recent scanning tunneling microscopy study[64] has demonstrated that the TTF molecules exhibit strong intermolecular electronic coupling leading to an enhanced lateral charge mobility and thus higher electrical conduction. Therefore, as the loading force increases, the compression apparently influences the molecular order as the AFM probe pushes or penetrates the monolayer thus decreasing the electronic coupling between neighboring TTF units. This in turn leads to the observed increase in the

junction resistance even though the number of molecules in direct mechanical contact with the AFM probe is increasing due to the increase in the contact area. Theoretical calculations performed by Magoga[65] and Joachim[33] support this hypothesis by showing that well-ordered molecular film structure can result in a decrease in the tunneling resistance. In that work, the resonance of molecular orbitals of conjugated molecules was shown to enhance the tunneling resistance by a well-ordered structure, while the molecular disordering leads to an increase in the resistance. This is consistent with the measurements shown in Figure 5a where an increase in resistance with applied force was observed. The observed decrease in the junction resistance at 33 nN is likely caused by the combination of factors (a) and (b) which start to dominate the response and the resistance above 40 nN is expected to decrease in the manner similar to that observed for the C_{10} SAM. As a final note, such nonlinear response of the TTF SAM resistance to the applied loading force may have practical applications as a possible nano-switch device where the current flow through the SAM can be efficiently controlled by the applied pressure.

2.4 Conclusions

In summary, the electrical conduction through TTF SAMs on gold was investigated using conducting probe atomic force microscopy (CP-AFM). CP-AFM was used to estimate the single TTF molecule resistance 14.7 ± 3.4 GΩ, which corresponds to the estimated resistivity of 390 Ω•cm. A single molecule resistance of a comparable length decanethiol is 950 ± 22 GΩ; this clearly indicates that the TTF molecule is remarkably conductive making it a promising candidate as a building block for molecular wires. Based on the molecular junction resistance versus loading force measurements, an

unusual increase in the resistance with an increase in force is observed. The unique dependence is attributed to the change in the intermolecular electronic coupling between the TTF molecules under compression. This study supports the premises that molecule-gold contact geometries other than simple single thiol-gold bond offer a possibility to significantly improve the electrical conduction through molecular systems thus making them valuable candidates for the future molecular devices.

CHAPTER 3

SEMICONDUCTING ORGANIC ASSEMBLIES PREPARED FROM TETRAPHENYLETHYLENE TETRACARBOXYLIC ACID AND BIS(PYRIDINE)S VIA CHARGE-ASSISTED HYDROGEN BONDING

3.1 Introduction

Achieving an ability to control the form of supramolecular constructs resulting from assembly of organic molecules in the solid state is a central aim of crystal engineering. It is anticipated that precise control over solid state assembly processes will facilitate the synthesis of complex functional materials imbued with desirable optical, electronic, magnetic, and/or physical properties starting from carefully chosen yet relatively simple molecular precursors.[66-68] In turn, organic materials assembled in this manner may exhibit distinct advantages over their inorganic counterparts in terms of *inter alia* performance, miniaturization, and mechanical flexibility.

In particular, the design of organic semiconductors is an area of research that may benefit greatly from development of successful crystal engineering synthetic strategies. The magnitude and efficiency of charge transport in solid state materials (crystals, films, polymers) composed of single-component redox-active organic compounds or multi-component combinations of electron donor/acceptor organic compounds has been shown to critically depend on the relative orientation of molecular constituents. For example,

---

This chapter was published in the *Journal of American Chemical Society* [Kapadia, Ditzler, Tivanski, and Pigge (2011) Semiconducting Organic Assemblies Prepared from Tetrephenylethylene Tetracarboxylic Acid and Bis(pyridines)s via Charge Assisted Hydrogen Bonding, 133, pp. 8490-8493].

numerous theoretical and empirical studies involving the prototypical organic conductor tetrathiafulvalene (TTF) and TTF derivatives indicate that charge mobility is enhanced when TTF components assemble in face-to-face intermolecular orientations.[69,70] Likewise, the presence of extended co-facial arene-arene contacts in polyacenes (a second family of organic conductors which includes tetracenes, pentacenes, perylenes, etc) also leads to greater conductivity.[71,72] Consequently, several studies have described efforts aimed at directing (controlling) solid state assembly processes of TTF's and polyacenes in order to optimize the electronic properties of bulk material.[73-80]

We are interested in utilizing tetraarylethylenes as starting materials in crystal engineering approaches to a range of functional materials. Tetraarylethylenes comprise a family of organic compounds that possess interesting opto-electronic molecular properties, such as low redox potentials and solid state photoluminescence.[81-86] Substituted tetraarylethylene frameworks can be conveniently prepared in only a few synthetic operations so that functional groups important in directing intermolecular interactions (e.g., H-bond donors or acceptors) can be easily incorporated. Coupled with the reasonably well-defined shape and geometry of the tetraphenylethylene core, these compounds are seemingly attractive solid state supramolecular building blocks. Toward this end, we have prepared an electron-rich tetraarylethylene derivative symmetrically functionalized with four acetic acid groups. We report here the successful crystallization of this tetraarylethylene derivative with several bis(pyridine) reagents to afford highly conducting organic materials. We also demonstrate that the charge transport properties of these crystals can be tuned as a function of the bis(pyridine) component.

3.2 Experimental

3.2.1 Crystal Formation

Tetraphenylethylene tetracarboxilic acid and bis(pyridines) were synthesized following reported procedures by Kapadia et. al.[87] Single crystals were formed through slow solvent evaporation and crystal structures were determined using single crystal x-ray analysis.[87] To form microcrystalline samples for measurements in CP-AFM studies a solution of **1** in methanol (10 mL) was added a solution of bis(pyridine) in acetone (10 mL) at room temperature. The molar ratio of **1** to bis(pyridine) was 1:1 in each case. The solution was thoroughly mixed and then allowed to evaporate to near dryness over 5-6 days. The solid residue, formed during this time, was collected by filtration and washed sequentially with methanol and acetone. Solid samples were then dried under vacuum at room temperature for 3 h to yield microcrystalline materials, which were characterized by PXRD.

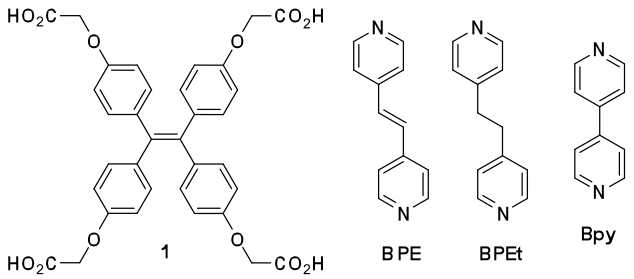

Figure 3.1. Crystal components used in this study.

3.2.2 TDOS Calculations

X-ray structural data obtained for **1**·**BPE**, **1**·**BPEt**, and **1**·**Bpy** was subjected to further quantum chemical refinement. Geometry optimization was performed using a hybrid B3LYP Hamiltonian[88,89] and all electron 6-31G(d) basis sets for C, N, C and H

atoms with H basis set having outer shell exponents of 0.1613 and 1.1 $bohr^{-2}$, previously successfully used in urea electronic structure calculations.[90] Radial and angular points of the grid were generated through Gauss–Legendre radial quadrature and Lebedev two-dimensional angular point distributions with a pruned grid of 75 radial and 974 angular points. Structure optimizations were performed using analytical energy gradients with respect to atomic coordinates,[91-93] within a quasi-Newton scheme combined with the Broyden–Fletcher–Goldfarb–Shannon scheme for Hessian updating.[94-97] Convergence was checked on both gradient components and nuclear displacements and was signaled when RMS gradient was 0.0003 and RMS displacement was 0.0012. Only atom positions were optimized while the unit cell parameters were kept fixed. Symmetry relationships were fully exploited in these calculations. Truncation criteria for bielectronic integrals were set to 7, 7, 7, 20 and 50 with shrinking factors of 4. For density of states (DOS) projection calculations, shrinking factors of 6 were used to get a denser grid and a more accurate DOS representation. Periodic *ab initio* solid state program suite CRYSTAL'09 was used in all calculations[98,99]; it uses the functions localized on atoms as the basis for expansion of the crystalline orbitals via linear combination of atomic orbitals (LCAO) technique.

3.2.3 Substrate and Sample Formation

The sample substrates were formed by thermally depositing Au on mica (V-I grade, SPI Supplies, Westchester, PA) substrates. Crystals were then suspended in hexanes (1 mg/mL) and deposited to the Au substrate. Samples were dried in air for 20 minutes to allow the solvent to evaporate and then immediately used for the conductivity measurements.

3.2.4 CP-AFM Measurements

Topographic height imaging and *I-V* measurements were performed using a commercially available atomic force microscope (MFP 3D, Asylum Research, Santa Barbara, CA) with a conducting probe module (ORCA, Asylum Research, Santa Barbara, CA). Samples were first imaged using AC mode imaging to determine crystal morphology. All imaging and measurements were collected using a diamond coated tip (NANOSENSORS, Switzerland) with a tip radius of curvature of 150 ± 50 nm and spring constant of 0.02-0.77 N/m. Crystals with heights between 20 and 300 nm were used for the *I-V* measurements. All *I-V* measurements were performed in an insulating bicyclohexyl solvent (99.0%, Fluka, Switzerland) in order to reduce water contamination and decrease the adhesion force caused by capillary forces between the AFM probe and sample due to water layer formation on the tip-surface interface. For these experiments force was held constant for all measurements at 50 nN. This force was found to be sufficient for a stable electrical contact. The bias was swept over various ranges, depending on the crystal thickness. For a thinner crystal, a smaller bias range was used to prevent saturation of the current. A combination of large applied forces and high current density may result in irreversible changes in crystal morphology. For that reason all crystals were imaged after the conductive measurements. Only crystals showing no obvious morphological changes were used for the data analysis.

3.3 Results and Discussion

3.3.1 Formation of Tetraphenylethylene Tetracarboxilic Acid Cocrystals

The compounds used in this study are illustrated in Figure 3.1. The tetracid **1** was easily prepared from the corresponding tetraphenol[100] via alkylation with ethyl bromoacetate followed by ester saponification. We initially envisioned that the carboxylic acid groups in **1** would each serve as H-bond donors along vectors approximating the sp^2 geometry of the central alkene carbons (despite the flexibility of the OCH_2 linkers connecting the acid groups to the tetraphenylethylene core). We reasoned that combining the tetratopic H-bond donor **1** with linear ditopic H-bond acceptors, such as bis(pyridine)s **BPE**, **BPEt**, or **Bpy**, may afford 2D sheet structures with alternating rows of tetraphenylethylene and bis(pyridine) components. Stacking of these 2D sheets could then result in potentially electroactive crystalline architectures featuring segregated columns of electron rich and electron deficient components (i.e., **1** and bis(pyridine), respectively).

Combining **1** with two molar equivalents of **BPE**, **BPEt**, or **Bpy** in a mixture of acetone and methanol did in fact lead to deposition of single crystals upon slow solvent evaporation. Contrary to expectations, however, co-crystals of 1:1 stoichiometry were obtained in each case as determined by single crystal X-ray diffractometry. The structure of **1**·**BPE** illustrates many features common to all three structures. Molecules of **1** adopt propeller-like conformations typical of tetraphenylethylenes in the solid state.[101] Two of the carboxylic acid residues of **1** are engaged in charge-assisted H-bonding with pyridine nitrogen atoms. From the position of the hydrogen atoms and the nearly equal C-O bond

lengths in the relevant carboxylic acid residues, we conclude that transfer of a proton to the pyridine has occurred so that the H-bonding interaction can be described as involving a pyridinium H-bond donor and a carboxylate H-bond acceptor (N···O distance = 2.59 Å). Each molecule of BPE bridges two adjacent molecules of **1** (as we originally envisaged) to generate 2D layers (Figure 3.2a). Disordered solvent molecules (not shown) occupy the voids between adjacent molecules of **1**.

The remaining carboxylic acid residues in **1**·**BPE** are involved in mediating the stacking of 2D layers through H-bonding interactions with carboxylate groups in adjacent layers. Two views of the extended packing are shown in Figs. 3.2b,c. As a consequence of these stacking interactions, individual 2D layers are aligned 180º in a slightly offset fashion down the *c* axis to produce an *abab*-type pattern. This results in well-defined segregated columns of **1** and **BPE** (Fig. 3.2c).

The single crystal structure of **1**·**BPEt** was found to be isostructural with **1**·**BPE**. Charge-assisted H-bonding between formally anionic carboxylate groups on **1** and dicationic bis(pyridinium)ethane units result in 2D layers analogous to that shown in Fig. 3.2a. Layers are then stacked as shown in Figs. 3.2b,c via additional $CO_2H\cdots{}^{-}O_2C$ hydrogen bonds. The only difference between the two structures is the presence of a π bond linking the two pyridinium groups in **BPE** – a structural feature that appears to exert significant influence over the conductivity of the material (*vide infra*).

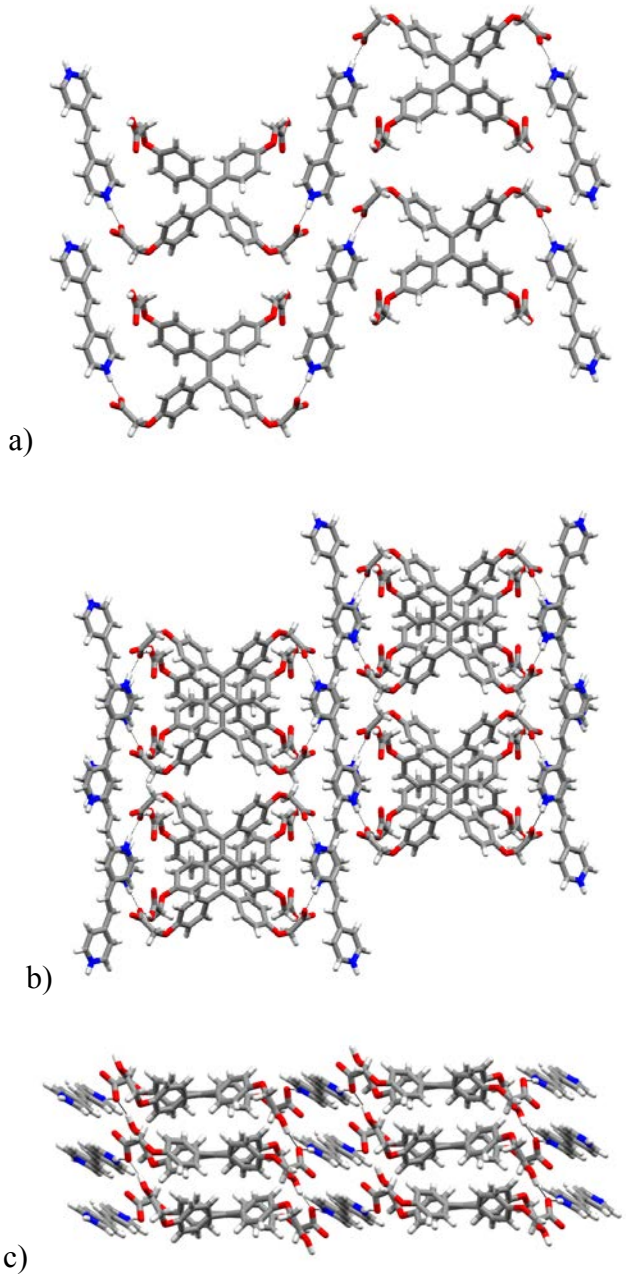

Figure 3.2. Structures a) 2D layer formed by charge-assisted H-bonding between **1** and **BPE** viewed down *c* (H-bonds shown as black lines). b) Stacking of 2D layers (down *c*) mediated by $CO_2H\cdots{}^{-}O_2C$ H-bonding. c) View of the crystal down *b* illustrating the segregated columns of **1** and **BPE**. Disordered solvate molecules omitted for clarity. Crystals of **1**·**BPEt** are isostructural with **1**·**BPE**.

The structure of **1**·**Bpy** also features bis(pyridine) units bridging molecules of **1** via charge-assisted H-bonding. In this case, however, the crystal participants are arranged in a step-like fashion rather than distinct layers. Nonetheless, segregated columns of **1** are clearly evident (Fig. 3.3). These columns are separated by layers of **Bpy** molecules oriented with their long axis roughly parallel with the direction of tetraarylethylene stacks.

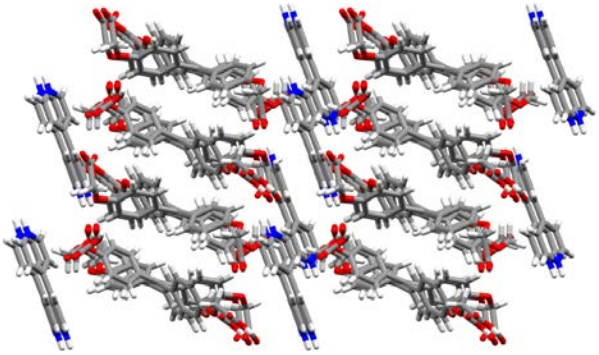

Figure 3.3. View of **1**·**Bpy** slightly offset from the *b* axis illustrating columns of **1** flanked by layers of **Bpy**. Disordered solvate molecules omitted for clarity.

Notably, the color of these crystals was found to vary from pink to orange to pale yellow as the bis(pyridine) component changed from **BPE** to **Bpy** to **BPEt**. Coloration may indicate varying levels of charge-transfer interaction in the solid state, presumably facilitated by the electron donating ability of **1** and the electron accepting abilities of the bis(pyridine)s (which are expected to be enhanced by their conversion to bis(pyridinium) species in the crystals). Structural evidence for charge-transfer interactions, however, was not apparent from X-ray data. For example, elongation of the central alkene C=C bond in **1** (as might be expected if **1** acquires partial radical cation character) was not observed. This bond length ranged between 1.358 and 1.363 Å in the crystals examined,

and these values are similar to the bond length reported for tetraanisylethylene (1.359 Å) and significantly shorter than the bond length reported for tetraanisylethylene radical cation (1.417 Å).[101] Consequently, electronic characteristics of these crystals were explored using DFT calculations.

3.3.2 Calculating the total density of states for the TPE samples

Experimentally obtained X-ray data was subjected to quantum mechanical analysis in the form of total density of states calculations (TDOS) in order to identify the crystalline orbitals involved in charge-transfer processes.[102] Atomic projections of density of states for **1**·**BPE** is shown in Fig. 3.4 (top) as the sum of contributions from 1) all carbon atoms, 2) C=C bonds, 3) O-C bonds, and 4) CO_2 functional groups in **1**, and 5) nitrogen, 6) carbon atoms in **BPE**, and 7) C=C in **BPE** (bottom to top in Fig. 3.4). The carbocycles in **1** emerged as the major contributors to the highest occupied crystalline orbital (HOCO) located at ~ –4.5 eV. The pyridyl carbon atoms and the C=C in **BPE** are calculated to be the dominant contributors to the lowest unoccupied crystalline orbital (LUCO) located at ~ –3.5 eV in Fig. 3.4a. The relatively small bandgap found in **1**·**BPE** (1.28 eV) provides a basis for the apparent charge-transfer interactions. Similar computational treatment of **1**·**Bpy** and **1**·**BPEt** (Fig. 3.4b and 3.4c, respectively) yielded HOCO levels of comparable energy (–4.5 eV). The LUCO levels, however, were shifted to slightly higher energies resulting in increased bandgap values of 2.47 eV and 1.99 eV, respectively (see Table 1).

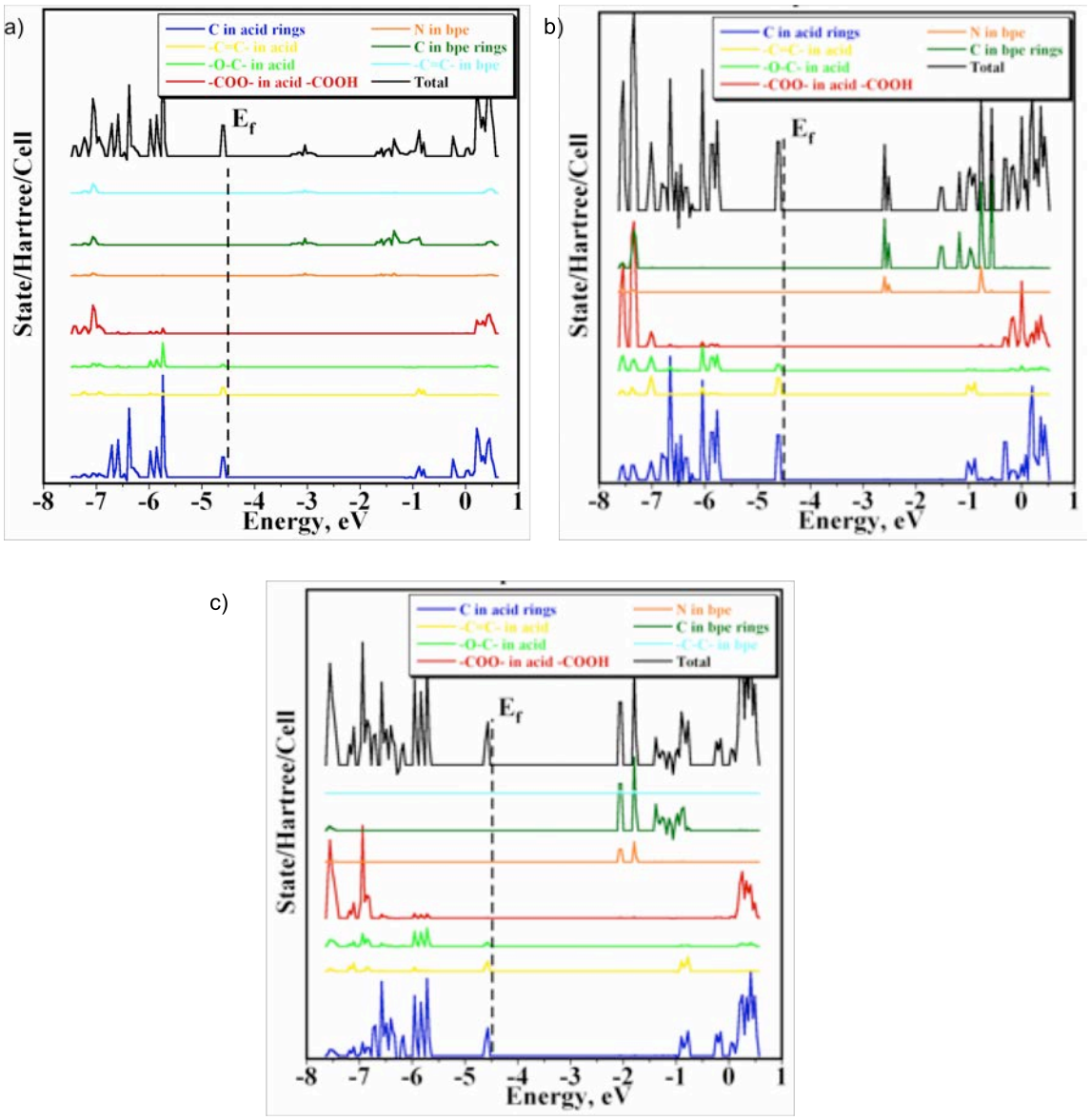

Figure 3.4. TDOS calculation for a) **1**·**BPE**, b) **1**·**Bpy**, c) **1**·**BPEt**. Fermi energy (E_f, dashed line) corresponds to the energy of the HOCO.

3.3.4 Quantifying the electrical properties using CP-AFM

The electrical properties of these co-crystalline assemblies were examined using conducting probe atomic force microscopy (CP-AFM). Bulk microcrystalline samples were prepared in good yield by concentration of equimolar solutions of **1** and **BPE**,

BPEt, and **Bpy**. Samples prepared in this way were found to be homogeneous and possessed forms identical to those found in single crystals as determined by PXRD shown in Figure 3.5. All three microcrystalline samples were also found to be thermally stable up to ~175 ºC as determined by TGA.

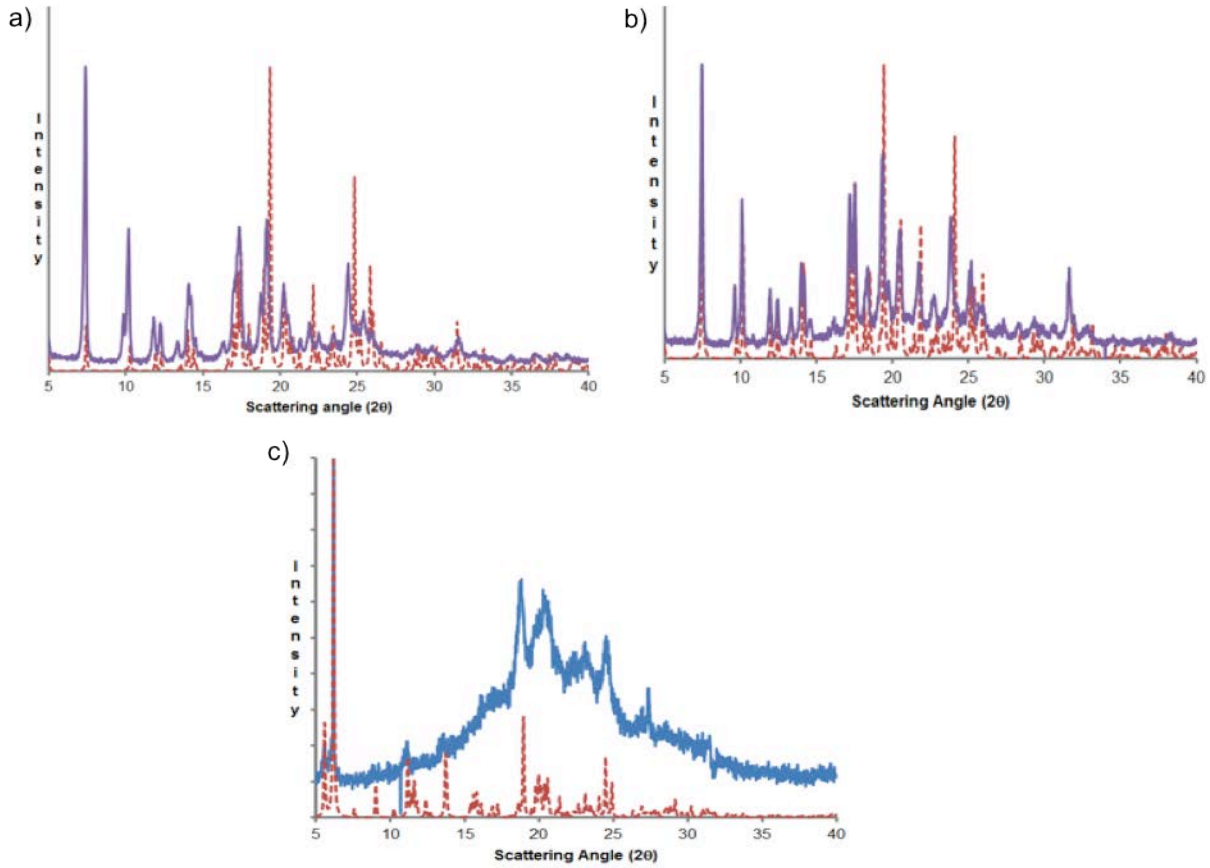

Figure 3.5. Comparison of calculated (dashes) and observed (solid) PXRD pattern obtained from bulk microcrystalline samples of **1**·**BPE**, **1**·**BPEt**, and **1**·**Bpy**.

For the CP-AFM studies, each sample was deposited on thermally evaporated Au substrate and imaged to determine crystal morphology and shape. A typical crystal image for **1**·**BPE** is shown in Fig. 3.6a. Crystals prepared from **BPEt** and **Bpy** were similar in appearance. Electrical measurements were performed on individual crystals in

an insulating organic solvent (bicyclohexyl) to prevent water layer contamination. Each measurement was collected under 50 nN of force, which provided sufficient contact between the crystal and the tip without damaging the crystal. The voltage bias range was then swept and the tip retracted from the surface. Each crystal was subjected to 15 current-voltage (*I-V*) measurements, and then the crystal was reimaged for comparison to the original image. Crystals exhibiting significant differences in images collected before and after conductivity measurements were not used in data analysis. Representative *I-V* curves are shown in Fig. 3.6b for **1**·**BPE**, **1**·**Bpy**, and **1**·**BPEt**. Note that the *I-V* curve for

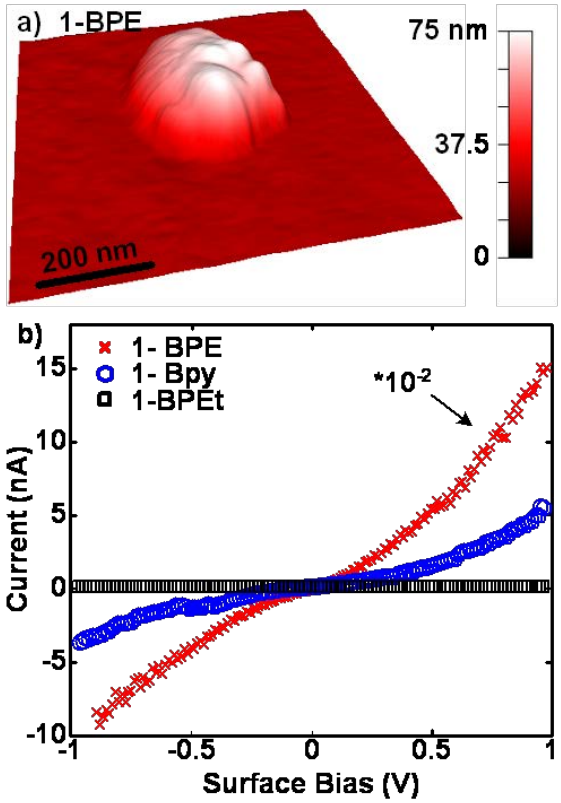

Figure 3.6. Representative 3D crystal image for **1**·**BPE**. b) Representative *I-V* curves for **1**·**BPE** (red crosses), **1**·**Bpy** (blue circles), and **1**·**BPEt** (black squares). The **1**·**BPE** curve is scaled downward by a factor of 100 to fit on the indicated axes.

1·**BPE** has been divided by a factor of 100 in order to be displayed on the same scale as the curves for the other two samples. From the representative data shown in Fig. 3.6b it is clear that crystals of **1**·**BPE** are highly conductive, while **1**·**Bpy** is moderately conductive and **1**·**BPEt** shows virtually no current throughout the voltage bias of the measurement.

The resistance (R) of individual **BPE** and **Bpy** crystals was calculated using the linear region of the *I-V* curves (bias range of ±0.15 V). This bias range was fit to Ohm's Law to obtain the resistance, and this value; along with values for crystal height (measured directly from AFM images) and probe-sample contact area were used to determine resistivity. Using the Hertzian elastic contact model, the contact area can be determined.[58,103,104]According to the model, the mechanical contact radius a between a spherical tip of radius r penetrating into a uniform elastic film may be estimated as

$$a^2 = \left(\frac{Fr}{K}\right)^{2/3} \quad (1)$$

where, F is the loading force and K is an effective modulus equaling

$$K = \frac{4}{3}\left[\frac{1-\nu_{Tip}^2}{E_{Tip}} + \frac{1-\nu_S^2}{E_S}\right]^{-1} \quad (2)$$

and E_S, ν_S, E_{Tip}, and ν_{Tip} are the Young's modulus and the Poisson's ratio of the sample and the silicon nitride AFM tip, respectively. The Poisson ratio for most materials is between 0.25 and 0.5,[58,103,104] and thus assuming $\nu_{Tip} \approx \nu_S \approx 0.33$, an effective modulus can be approximated as $K=1.5E_{Tip}E_S/(E_{Tip}+E_S)$. The elastic modulus of the diamond tip is 1220 GPa.[105] The E_S for similar materials was assumed to be 350 MPa.[106-109] Using the above parameters, the contact area between the diamond-coated AFM tip and crystal is estimated to be 1850 ± 50 nm^2.

The mean resistivity (ρ) for each crystal was then calculated and plotted in Figure 3.7. The error bars indicate the range of resistivity's determined from 15 separate *I-V* measurements. The mean resistivity for each sample was then calculated as the average over all crystals. This data, along with related conductivity values (σ), are shown in Table 3.1. The resistivity for **1**·**BPEt** crystals could not be determined due to the absence of measureable current within the detection limit of the instrument (10 pA). Thus, the resistivity value shown in Table 1 (2.4 x 10^6 W·cm) represents a lower limit.

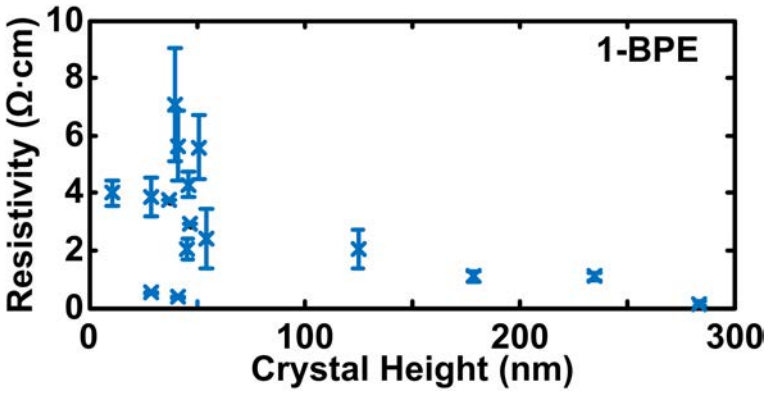

Figure 3.7. Resistivity vs. Crystal Height for **1**·**BPE.**

Finally, we attempted to calculate effective charge mobilities (μ_{eff}) for the two conductive crystal samples using the space-charge limited current model.[110,111] This approach was not suited to these samples, however, as the data in both cases exhibited a non-linear *I* vs. V^2 relationship. Thus, charge mobilities were estimated using a simple empirical model advanced by Brown that relates electron mobility to conductivity ($m = s^{0.76}$) as shown in Table 1.[112,113]

Table 3.1. Physical and electrical properties of 1·bis(pyridine) crystals.

Crystal	color	Bandgap[a]	r (W·cm)	s ($S \cdot cm^{-1}$)	m_{eff} ($cm^2/V \cdot s$)[c]
1·BPE	pink	1.28 eV	3.6 ± 0.9	0.28 ± 0.06	0.38 ± 0.05
1·Bpy	orange	1.99 eV	213 ± 70	$(4.7 \pm 1.3) \bullet 10^{-3}$	$(1.7 \pm 0.4) \bullet 10^{-2}$
1·BPEt	yellow	2.47 eV	$> 2.4 \bullet 10^{6}$	nc[b]	nc

[a]Determined computationally from TDOS calculations. [b]Not calculated. [c]$m = s^{0.76}$.[112,113]

The data obtained from CP-AFM conductivity studies clearly show that **1·BPE** and **1·Bpy** function as crystalline organic semiconductors. Indeed, the estimated m_{eff} for **1·BPE** (0.38 $cm^2/V \cdot s$) is comparable to charge mobilities determined for single crystals and crystalline films of well-established polyacene and thiophene-based organic conducting materials.[73-80,114] Moreover, the results also demonstrate an ability to tune the conducting properties of these tetraarylethylene crystals as a function of bis(pyridine) agent. The most conjugated bis(pyridine) reagent (**BPE**) afforded crystals with **1** exhibiting conductivity approximately two orders of magnitude greater than crystals obtained from 4,4'-bipyridine, while co-crystals derived from **1** and non-conjugated **BPEt** were insulators. These conducting properties correlate nicely with TDOS computational studies that revealed a systematic lowering of crystalline conduction bands (LUCO's) in the crystal series **1·BPEt**, **1·Bpy**, and **1·BPE** (compare Figs. 4). Coupled with the nearly identical HOCO energies across the series, the net effect of LUCO lowering was a narrowing of crystal bandgap energy.

3.4 Conclusions

Currently the relative contributions of **1** and the bis(pyridine) moieties in governing charge mobility are not known. The high conductivity exhibited by **1·BPE**

and the absence of conductivity in **1**·**BPEt** despite their isostructural crystalline networks seemingly suggests a crucial role for the bis(pyridine) units as principal charge carriers. In the case of **1**·**BPE**, the combination of protonated **BPE** molecules arranged in roughly co-facial orientations and p-conjugation between facially stacked rings might facilitate charge transport in two dimensions (see Fig. 3.2b). In line with this conjecture, the diminished conjugation in **1**·**Bpy** may contribute to the attenuated conductivity in this sample while the absence of conjugation in **BPEt** renders this crystal an insulator. This model relegates **1** to the role of a crystalline scaffold that properly orients and activates (through protonation/H-bonding) the pyridine components for charge transport. In this regard, other relatively simple polycarboxylic acids may fulfill a similar function and studies exploring this possibility are underway. Alternatively, **1** may also contribute in some degree to the conducting properties of these assemblies as a consequence of intermolecular arene edge-to-face interactions and/or participation in extended H-bonded networks.[115,116] The synthetic accessibility of additional tetraarylethylene and bis(pyridine) derivatives should facilitate formulation of systematic structure-activity studies designed to shed light on this issue.

In conclusion, we have successfully prepared and characterized a series of stable crystals from acetic acid-substituted tetraphenylethylene and three bis(pyridine)s. Two of these supramolecular assemblies were found to exhibit conductivities comparable to those of established organic semiconductors as determined through CP-AFM. Importantly, the conducting properties of these multi-component crystals can be modulated as a function of bis(pyridine) partner, opening exciting opportunities for

construction of new tunable electro-active organic materials. This study also illustrates the potential of tetraarylethylenes to serve as attractive supramolecular building blocks.

CHAPTER 4
NANOCRYSTALS OF DINUCLEAR AG-PYRIDINE COMPLEX EXHIBIT HIGH ELECTRICAL CONDUCTIVITY

4.1 Introduction

The design of functional solid-state materials with desirable properties lies at the core of crystal engineering. Crystal engineering is under increasing development[117] with emerging applications in areas such as reactivity,[118] porosity,[119] and magnetism.[120] In this context, the development of electronic materials such as organic semiconductors using principles of crystal engineering remains in early stages. Applications of functional organic semiconductors are projected to envelope a trillion dollar industry based on flexible electronics, smart cards, and solar panels among others.[121] A current challenge lies in a necessity to achieve face-to-face π-stacking of semiconductor molecules in the solid state. Indeed, crystal engineering offers an opportunity to design organic semiconductor materials with structurally- and electrically-favorable arrangements of molecules.[122] The relevance of extending concepts of crystal engineering to nanoscale electronics is also particularly important since electronic materials of nanoscale dimensions exhibit promise in the development of solar cells[123] and optoelectronic devices.[124] Furthermore, nanocrystalline materials uniquely offer long-range order and well-defined molecular packing with a large surface to volume ratio and decreased size, which are characteristics that are highly applicable in the field of electronics.

In recent years whereas purely organic π-rich molecules (e.g. pentacene) have been pursued as building blocks of semiconductor materials, the integration of metal atoms into such materials with favorable charge mobilities is at a nascent stage of

development. The directionality of coordination bonds supported by transition-metal-ions can be exploited to achieve face-to-face stacking that leads to favorable enhancement of conductivity in solids.[125] In this regard, a metal-organic complex that exhibits relatively high conductivity is $[Ag_2(ophen)_2]$ (where: ophen = [1,10]phenanthrolin-2-one). The solid consists of two Ag(I) ions that each coordinate to two N-atoms and a single O-atom to form a chelation complex that stacks face-to-face to afford a solid with a reported conductivity of 14 $S \cdot cm^{-1}$.[122] Indeed, a major tenet in the field of crystal engineering is that supramolecular synthons can be employed as reliable means tune properties of molecular solids. Moreover, in the case of solids based on Ag(I), both the Ag···Ag interaction and Ag-N(pyridyl) bond are ubiquitous in crystal engineering; however, both remain unexplored for applications in controlling the properties of semiconductor materials.

Here, we report a Ag-based metal-organic solid, in the form of $[Ag_2(4\text{-stilbz})_4][CO_2CF_3]_2$ (where: 4-stilbz = *trans*-1-(4-pyridyl)-2-(phenyl)ethylene) that exhibits high conductivity. The solid is sustained by Ag···N(pyridine) bonds that align the stilbazoles into a face-to-face π-stacked geometry. Additionally, components of the solid are designed to undergo a [2+2] photodimerization, which results in a 20 percent increase in conductivity. We also show a critical dependency of anion effects as the substitution of an alternative silver anion in an isostructural complex, $[Ag_2(4\text{-stilbz})_4][CF_3SO_3]_2$, showed no measureable current. The focus of this work is crystalline $[Ag_2(4\text{-stilbz})_4][CO_2CF_3]$.[126] The complex is sustained by Ag-N(pyridine) bonds (Ag-N1: 2.161 Å Ag-N2: 2.150 Å) and an Ag···Ag force (3.437 Å). Collectively, the two types of bonds align the stilbazoles into a face-to-face π-stacked structure. The complex self-

assembles to give 1D quadruple-stacked arrays that lie canted to one another. Given that the stilbazoles assume face-to-face π-stacking, we sought to determine whether the geometry was suitable to facilitate electronic communication through the π-electrons.

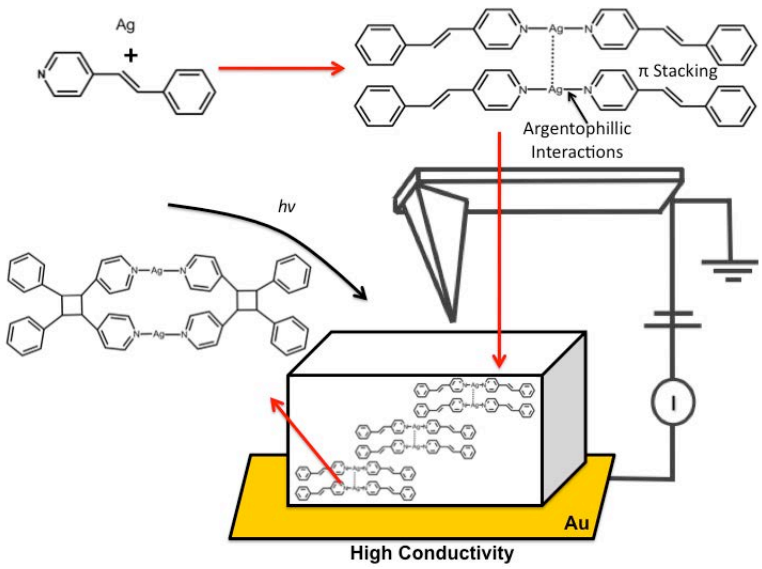

Figure 4.1. Schematic Representation of the Experimental Approach

4.2 Experimental

4.2.1 Synthesis and Characterization of Silver Coordination Complexes

A round bottom flask was charged with bromobenzene (10 g, 0.063 mol), 4-vinylpyridine (6.695 g, 0.063 mol), $PdCl_2(PPh_3)_2$ (1.26 g, 2.8 mol %), and potassium carbonate (12.5 g, 0.09 mol) in 100 mL DMF. The solution was refluxed overnight. The solution was cooled and poured over ≈ 500 mL of ice. The precipitate was filtered and purified via sublimation to afford white crystals.

Compound $[Ag_2(4\text{-stilbz})_4][CO_2CF_3]_2$ was prepared by dissolving 25 mg of 4-stilbz and 15.2 mg of $AgCO_2CF_3$ (Sigma Aldrich) separately in ethanol. The compounds were simultaneously injected into 200 mL of hexanes and exposed to ultrasonic irradiation for two minutes.[127] The solid was filtered and coordination complex formation was confirmed via powder x-ray diffraction. Powdered sample of complex $[Ag_2(4\text{-stilbz})_4][CO_2CF_3]_2$ was exposed to broadband UV irradiation using a medium pressure Hg lamp for 20 hours. ^{1}HNMR was performed to ensure complete photodimerization.

Compound $[Ag_2(4\text{-stilbz})_4][SO_3CF_3]_2$was prepared by slow evaporation of a solution of 40 mg of 4-stilbz and 28.4 mg of $AgCF_3SO_3$ (Sigma Aldrich) in acetonitrile. Coordination complex formation was confirmed via powder x-ray diffraction. Powdered sample of complex $[Ag_2(4\text{-stilbz})_4][SO_3CF_3]_2$ was exposed to broadband UV irradiation using a medium pressure Hg lamp for 30 hours. ^{1}HNMR was performed to ensure complete photodimerization. Crystal data for $[Ag_2(4\text{-stilbz})_4][SO_3CF_3]_2$: monoclinic, space group C2/c, a = 22.057(2) Å, b = 12.7542(12) Å, c = 18.300 (2), β = 98.105(5)°, V = 5096.72(38) Å^3, Z = 4, ρ_{calc} = 1.61 g/cm^{3}and R_1 = X for X reflections with I > 2σ(I). Crystal data for $[Ag_2(4\text{-pyr-ph-cb})_2][CO_2CF_3]_2$: monoclinic, space group C2, a = 21.7680(44), b = 13.4980(27), c = 17.5700(35), β = 98.240(30)°, V = 5109.20(225) Å^3, Z = 4, ρ_{calc} = 1.58 g/cm^{3}and R_1 = X for X reflections with I > 2σ(I).

4.2.2 Substrate Preparation

The sample substrates were formed by thermally depositing Au on mica (V-I grade, SPI Supplies, Westchester, PA) substrates. Au modified mica substrates were fixed to a glass slide using epoxy (Epotek 377, Epoxy Technology, Billerica, MA). Crystals were then suspended in hexanes using 1 milligram of crystals per 0.5 milliliter of

hexane and sonicated for 30 seconds to evenly disperse the material. The crystal suspension was then added to the Au substrate added drops wise. Samples were air dried for 20 minutes until the solvent was evaporated and immediately used for measurements and characterization using conductive probe atomic force microscopy. In nanoindentations experiments samples were prepared under the same conditions and crystals were deposited on glass substrates.

4.2.3 Conductive Probe AFM Measurements

Topographic height imaging and current-voltage (*I-V*) measurements were performed using a commercially available atomic force microscope (MFP 3D, Asylum Research, Santa Barbara, CA) with a conducting probe module (ORCA, Asylum Research, Santa Barbara, CA). Samples were first imaged using AC mode imaging to determine crystal morphology. All imaging and measurements were collected using a diamond coated tip (NANOSENSORS, Switzerland) with an average radius of curvature of 150 ± 50 nm and average spring constant between 0.02 - 0.77 N/m. Crystal showing average morphology with heights between 20 and 200 nm were used for *I-V* measurements. All *I-V* measurements were performed in air. For these experiments force was held constant for all measurements at 50 nN. This force was found to be sufficient for a stable contact to obtain reproducible measurements. The bias was swept over various ranges, depending on the crystal thickness. For a thinner crystal a smaller bias range must be used to prevent saturation of the detector. High currents and biases can lead to sample deformations, therefore all crystal were imaged after measurements. Only crystals showing no sample deformation and morphology matching the initial image were used for the data analysis.

4.2.4 Nanoindentation Measurements

AFM nanoindentation measurements were collected at room temperature using silicon probes (Mikromasch, San Jose, CA, CSC37) with a nominal spring constant of 0.35 N/m and a typical tip radius of curvature of 10 nm. Actual spring constants were determined using built-in thermal noise method. Topographic images were collected using intermittent contact mode both before and after indentation experiments to compare crystal morphology. Force-displacement curves were recorded in an organic solvent, n-tetradecane (Sigma,), which served to minimize capillary adhesion between the probe and the surface in ambient conditions. In a single force-displacement curve the AFM probe approaches the crystal, and contacts the crystal face applying 10 nN, and subsequently, retracts from the surface recording the force as a function of vertical displacement from the sample. The applied force of 10 nN provides reproducible results without damaging the crystal surface. A total of 10 sample locations were collected per crystal recording 10 measurements per location to insure reproducibility. Similar measurements on the substrate were preformed to calibrate the deflection sensitivity of the AFM instrument, which is used to convert the force-displacement curve to force versus tip-sample separation plot. For these experiments roughly 30 different crystals and two different AFM tips were used for each crystal sample. All force-displacement plots used displayed no deviation between the approach and retract data, hence the indentation can be assumed purely elastic.[103]

4.3 Results and Discussion

4.3.1 Measuring Electrical Properties of Single Crystals

In our first experiments, we attempted to measure electrical properties of $[Ag_2(4\text{-stilbz})_4][CO_2CF_3]_2$ on prism-shaped single crystals of millimeter dimensions. A two-point probe technique capable of measuring resistances of 2000 kΩ was employed. In a typical experiment, two probes were contacted on opposite crystal faces and resistance was measured. All attempts, however, resulted in no measureable response. Moreover, all crystals cleaved during measurement attempts with cleavage occurring along no specific axis. We, thus, ascribe the inability to detect current to the crystals, in part, being fragile, which results in an accumulation of cleavage planes. It is possible these cleavages arise owing to shearing of the 1D arrays, which are likely disrupted.

4.3.2 Preparation and Characterization of Nanocrystals

Due to the cleavage of macro-sized crystals during two-point probe measurement, we turned to employ conductive probe atomic force microscopy (CP-AFM). CP-AFM is frequently used to characterize organic crystals and polymeric materials.[87,128-130] To measure the electrical properties of $[Ag_2(4\text{-stilbz})_4][CO_2CF_3]_2$, we expected that nano-sized crystals would likely have minimal crystal defects and crystal cleavage. Decreasing the size of the sample may yield to less cleavable crystals due to there large surface to volume ratio which permits a more efficient stress and strain relaxation mechanism.[107]

To form nanocrystals, we turned to sonochemistry. The utility of sonochemistry to afford crystals of nanoscale dimensions has been demonstrated in the synthesis of inorganic based nanocrystals[131] and nanocrystals unobtainable by other techniques.[132] The individual components 4-stilbz and $AgCO_2CF_3$ were, thus, dissolved separately in

minimal ethanol and simultaneously injected into a solution of hexanes under ultrasonic irradiation for two minutes.[127,133] The precipitate was filtered and coordination complex formation was confirmed via powder x-ray diffraction (PXRD). Scanning electron microscopy (SEM) was used to confirm formation of nano-sized crystals. SEM micrographs revealed prism shaped crystals in the range of 40-80 nm in diameter (Figure 4.2).

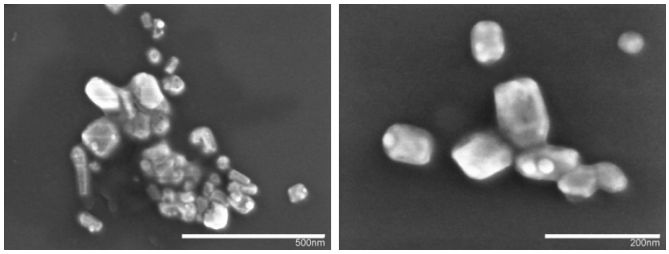

Figure 4.2. SEM micrograph of $[Ag_2(4\text{-stilbz})_4][CO_2CF_3]_2$ nanocrystals before UV irradiation. Crystal sizes are in the range of 40-80 nm in diameter.

4.3.3 Electrical Properties of $[Ag_2(4\text{-stilbz})_4][CO_2CF_3]_2$ nanococrystals

Conductive probe AFM (CP-AFM) was utilized to determine morphology of individual crystals followed by electrical measurements. Figure 4.3a shows representative height image of a $[Ag_2(4\text{-stilbz})_4][CO_2CF_3]_2$ nanocrystal; all crystals displayed similar morphology. All current-voltage (*I-V)* measurements were collected on individual crystals. The measurements were performed in air. Each measurement was collected under 50 nN of force, which provided stable electrical contact between the crystal and the tip, without damaging the crystal. The bias range was swept and the tip retracted from the surface. After 15-replicate *I-V* measurements, the sample was

reimaged and compared to the original image. Crystals with images deviating from the original images were not used in the data analysis. This crystal deformation occurs in 10% of the crystals used in these measurements. A representative *I-V* curve for $[Ag_2(4\text{-stilbz})_4][CO_2CF_3]_2$ crystal with a height of 95 nm is shown in Figure 4.3b. As can be seen from the figure, crystals display highly appreciable electrical current.

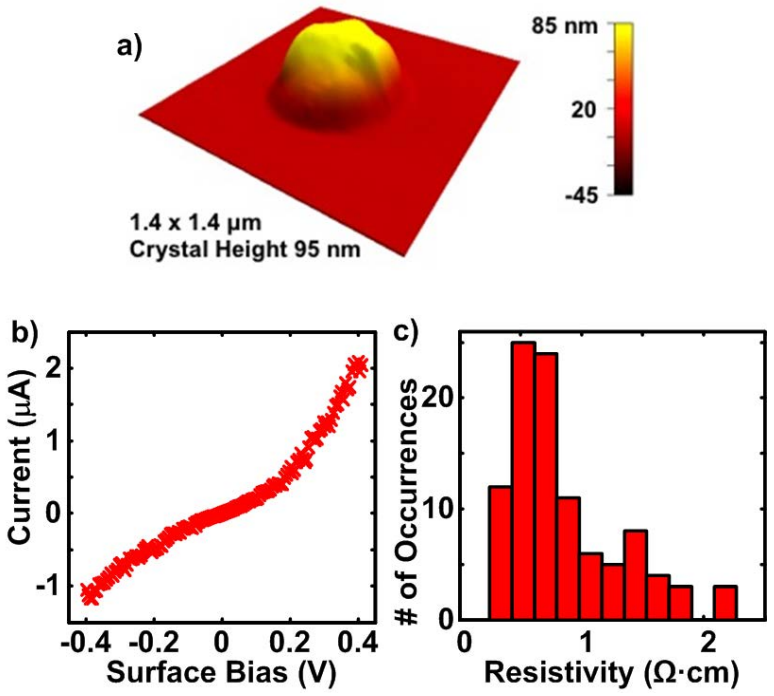

Figure 4.3. Representative height image for a) $[Ag_2(4\text{-stilbz})_4][CO_2CF_3]_2$, b) the representative IV curves for $[Ag_2(4\text{-stilbz})_4][CO_2CF_3]_2$ and c) distribution of resistivity values for $[Ag_2(4\text{-stilbz})_4][CO_2CF_3]_2$.

For more quantitative analysis of electrical properties, resistivities for each sample type were determined using linear Ohmic region of the *I-V* curve within ± 0.06 V. This bias range was fit using Ohm's Law and the resistance obtained, followed by the calculation of resistivity (ρ) as

$$\rho = R\left(\frac{a}{l}\right) \quad (1)$$

Resistivity was calculated using equation 1 where l is the crystal height and a is the contact area between the probe and the sample. Crystal height was measured directly from the AFM height images.[87] To calculate the contact area between the probe and the sample, the Hertzian elastic contact model was used as described previously.[107] The elastic modulus of the sample was directly measured using nanoindentation.[107] The Young's modulus of $[Ag_2(4\text{-stilbz})_4][CO_2CF_3]_2$ was found to be 350 ± 80 MPa with a corresponding contact area of 1850 ± 40 nm^2.

The resistivity of individual measurements was then calculated with distributions shown in Figure 4.3c. The mean resistivity was then found to be 0.86 ± 0.47 Ω•cm for $[Ag_2(4\text{-stilbz})_4][CO_2CF_3]_2$. The corresponding electrical conductivity of the material is 1.17 ± 0.41 $S \bullet cm^{-1}$. This value is appreciable for metal-organic coordination compounds, with only one silver organic compound ($[Ag_2(ophen_2)]$) in the literature which displays higher conductivity, 14 $S \bullet cm^{-1}$, making these Ag crystals of high interest in applications such as molecular electronics, and the development of new electrical materials.[122]

A unique feature of $[Ag_2(4\text{-stilbz})_4][CO_2CF_3]_2$ is its ability to undergo a [2+2] photodimerization in the solid state. To our knowledge, the conductivity of a material before and after photoreaction has not been reported. The photodimerization occurs via a single-crystal-to-single-crystal (SCSC) reaction in the solid state yielding the photoproduct $[Ag_2(4\text{-pyr-ph-cb})_2][CO_2CF_3]_2$. Crystals that undergo SCSC reactions are promising for applications in sensing devices.[134,135] The elastic modulus of the sample was again directly measured using nanoindentation. The Young's modulus of $[Ag_2(4\text{-pyr-ph-cb})_2][CO_2CF_3]_2$ was found to be 200 ± 40 MPa with a corresponding contact area

of 2690 ± 120 nm^2. This corresponds to a 40 percent decrease in the Young's modulus due to the photoreaction. This decrease is attributed to the large changes in the crystal structure (i.e. cyclobutane ring). The Young's modulus values for both the $[Ag_2(4\text{-stilbz})_4][CO_2CF_3]_2$ and its photoproduct are comparable to Young's moduli previously reported for nano co-crystals of 2(5-cyanoresorcinol)·2(trans-1,2-bis(4-pyridyl)-ethylene), where the Young's modulus was found to be 250 MPa. This sample also undergoes a [2+2] photodimerization and results in a 40 % increase in Young's modulus, 460 MPa for the photoproduct.[107] While the trend is opposite, the crystal composition and structure play a key role in the Young's modulus most likely impacting the changes in crystal stiffness.

Electrical properties of the material were then calculated as previously mentioned. The representative *I-V* curve of $[Ag_2(4\text{-pyr-ph-cb})_2][CO_2CF_3]_2$ is shown in Figure 4.4a. The data shows a slight decrease in the resistivity of the material upon photodimerization, as can be seen from the histograms (Fig. 4.4b) and mean values. The mean resistivity was then found to be 0.67 ± 0.58 Ω•cm for $[Ag_2(4\text{-pyr-ph-cb})_2][CO_2CF_3]_2$. The corresponding electrical conductivity of the material is 1.50 ± 0.84 $S•cm^{-1}$, corresponding to a 20% decrease in resistivity after the photoreaction. Before exposure to UV irradiation, the complex displays π-π interactions with an angle between the molecules of the dinuclear assembly at 1.49° and a close Ag···Ag interaction at 3.4 Å which contribute to the material's electrical conductivity. After photodimerization, the Ag···Ag distance increases and a new Ag···C(phenyl) interaction forms (2.647 Å) in addition to the cyclobutane ring. The interaction of the Ag with the neighboring phenyl group falls

within the limits for reported Ag(I)-aromatic compounds[136] and overcomes the increase in Ag···Ag distance which results in a slight increase in electrical conductivity.

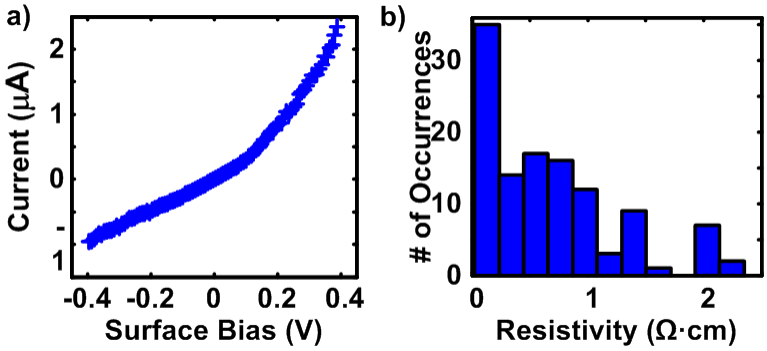

Figure 4.4. Representative IV curves for a) $[Ag_2(4\text{-pyr-ph-cb})_2][CO_2CF_3]_2$and b) distribution of resistivity values for $[Ag_2(4\text{-pyr-ph-cb})_2][CO_2CF_3]_2$

This observation led to further investigation into the source of the electrical current. Of interest was $[Ag_2(4\text{-stilbz})_4][CF_3SO_3]_2$ and its photoproduct $[Ag_2(4\text{-pyr-ph-cb})_2][CF_3SO_3]_2$, which are isostructural to $[Ag_2(4\text{-stilbz})_4][CO_2CF_3]_2$ and its photoproduct $[Ag_2(4\text{-pyr-ph-cb})_2][CO_2CF_3]_2$ barring the change in silver anion. The same measurements were repeated on these samples, which produced a significantly different outcome. While the $[Ag_2(4\text{-stilbz})_4][CO_2CF_3]_2$ and its photoproduct $[Ag_2(4\text{-pyr-ph-cb})_2][CO_2CF_3]_2$ nanocrystals showed appreciable conductivity for a metal-organic coordination compound, the isostructural crystals with the anion CF_3SO_3 showed no measureable current using our instrument. If we are incapable of measuring the current, the crystals' resistivities must be greater than $2.4 \bullet 10^6$ Ω•cm. In the complex $[Ag_2(4\text{-stilbz})_4][CF_3SO_3]_2$, the Ag···Ag distance is slightly larger at 3.927 Å. Additionally, the anions (CF_3SO_3) do not coordinate to the metal center and the closest Ag···O distance is 2.758 Å. In the complex with the trifluoroacetate anions, the anions coordinate to the

metal and the Ag···O distance is 2.593 Å. Therefore, changing the anion has turned the crystal into an insulator.[137]

4.4 Conclusions

The development of functional materials is at the forefront of crystal engineering. The tapestry of materials and functional groups give rise to a variety of new materials. The use of silver pyridine interactions forms $[Ag_2(4\text{-stilbz})_4][CO_2CF_3]_2$, a highly conductive solid. Interestingly, the conductivity increases when the material is photoreacted to 100% through a [2+2] photodimerization. This high conductivity makes it an ideal material for electronic applications. Through the developments in crystal engineering we may be able to tune material properties to enhance conductivity.

CHAPTER 5
PROBING MOLECULAR ENVIRONMENTS AND LOCALIZED REDOX TRANSITIONS AT METAL-SAM-METAL NANOJUNCTIONS USING CONDUCTIVE PROBE ATOMIC FORCE MICROSCOPY

5.1 Introduction

Self-assembled monolayers (SAMs) have been extensively studied to understand interfacial electron transfer through metal-SAM-metal nanojunctions for applications in the field of molecular electronics. Conductive probe atomic force microscopy (CP-AFM) is used to characterize the electrical and structural properties of metal-SAM-metal (m-SAM-m) junction through imaging capabilities and simultaneous collection and control of force, bias, and current.[138],[139] making it is possible to monitor electrochemical processes using force and current to detect redox changes of 11-ferrocenyl-1-undecanthiol (Fc) monolayers using CP-AFM.[139] Fc has been used extensively in electrochemistry studies due to their ability to undergo a reversible single-electron oxidation-reduction process. It was observed that Fc monolayers undergo negative differential resistance (NDR), or a large increase and decrease in current at surface biases around 1.6 V. At a surface bias of 1.6 volts the ferrocene endgroup is oxidized and subsequently reduced causing an increase and subsequent decrease in the current is observed (NDR). This observation is also paired with an increase in attractive electrostatic forces between the negatively charged tip and sample at the same bias.[139] These trends at the nanoscale where only a small number of molecules are probed are increasingly of interest, as well as, difficult to understand due to their complex nature.

However, by controlling the sample composition we can develop further insight into ways to control sample characteristic.

One of CP-AFM's strengths is its ability to probe a small number of molecules in a monolayer. Cyclic voltammetry studies on mixed monolayers of 11-ferrocenyl-1-undecanthiol (Fc) and 1-decanethiol show that change in the concentration of Fc or molecular environment has a strong effect of the electrochemical response of the monolayer. As the concentration becomes larger and the number of Fc molecule in direct neighboring contact increases, an increase in the electric potential required to oxidize the molecules is observed.[140] The formation of mixed SAMs of 11-ferrocenyl-1-undecanethiol (Fc) and decanethiol (C_{10}) would limit the number of electroactive Fc species in the junction and allow for further investigate the role of molecular environments on electrochemical processes (i.e. reduction-oxidation), at m-SAM-m nanojunctions. By controlling the compositions of the m-SAM-m junction, the localized reduction-oxidation transitions of Fc can potentially be characterized. Previous studies on this binary SAM report changes in work function,[141] cyclic voltammetry redox potential,[140,142]and monolayer tilt angle and structure[141,143] as concentrations ratios of the two components are varied. However, there is a limited knowledge of the redox properties of metal-SAM-metal nanojunction of mixed Fc-C_{10} SAMs which involve a limited numbers of redox molecules, as well as the ability to probe and quantify localized redox processes of Fc using CP-AFM.

In order to investigate redox processes at the nanoscale mixed SAMs of Fc and C_{10} were prepared by a simultaneous adsorption method,[140] where Au substrates were incubated in a mixture of Fc and C_{10}, and subsequently investigated using CP-AFM. The

bias-dependent adhesion forces between the tip and mixed SAMs under constant bias were used to investigate the role of intermolecular forces and environments on reduction-oxidation processes at the nanoscale. Understanding the impact of neighboring molecules on these processes will provide a greater understanding of redox reactions at the nanoscale. Additionally, the number of oxidized molecules at the nanoscale was quantified and compared to the number of molecules in the junction, offering a reliable way to detect and quantify localized reduction-oxidation transition at the nanoscale.

5.2 Experimental

5.2.1 Self Assembled Monolayers (SAMs) on ultraflat gold

Ultraflat gold (Au) surfaces were fabricated using the template-stripping method.[43] Briefly, thermally evaporated gold surfaces on freshly cleaved mica substrates (V-I grade, SPI Supplies, Westchester, PA) were glued facedown using an epoxy glue (Epotek 377, Epoxy Technology, Billerica, MA) on clean glass slides. The surfaces were then thermally cured in an oven for at least 2 hours at 150 °C. Finally, the ultraflat Au surfaces were obtained by stripping the mica from the gold in tetrahydrofuran solvent. The ultraflat Au surfaces so prepared were rinsed in ethanol and dried in a stream of nitrogen gas. Subsequent AFM height measurements of the ultraflat Au surfaces resulted in a typical root-mean-square roughness of less than 0.5 nm over 5 μm^2 area.

Uniform self-assembled monolayers (SAMs) of decanethiol ($C_{10,}$ Sigma, St. Louis, MO) and mixed SAMs of 11-ferrocenyl-1-undecanethiol (Fc, Dojindo Molecular Technologies, Inc., Rockville, MD) and C_{10} on ultraflat gold (Au) surfaces were produced by incubating the freshly prepared ultraflat Au surfaces in 2 mM ethanol solutions containing the two components in various concentration ratios. Five different

solution mixtures were prepared with molar ratios for Fc of 0, 0.1, 0.23, 0.33, 0.43, 0.55, and 1. The incubation time was at least 12 hours.[140] After assembly, the samples were rinsed in ethanol and sonicated to remove any unbound or physiosorbed molecules. Finally, samples were dried under an argon flow and used immediately for AFM characterization. All preparations were performed at room temperature under ambient conditions.

5.2.2 Cyclic Voltammetry Measurements

Cyclic Voltammetry was performed using CH instrument 760B potentiostat and a three-electrode cell, following previous work by Lee et al.[140] A saturated Ag/AgCl electrode and a platinum electrode was used as the reference and counter electrodes, respectively. The gold-working electrode was functionalized using the same procedure as for the ultraflat Au substrates described above. Each gold electrode was cleaned and incubated in the appropriate mixture solution for at least 12 hours. The sample cell was purged with N_2 gas for 30 minutes prior to each set of measurements. All measurements were carried out in 1 M $HClO_4$ aqueous solution at room temperature, under a constant N_2 gas flow. The electrochemical sweep range was from -0.2 to 0.8 V at a scan rate of 0.02 V/s, and five repeated sweeps were collected on each functionalized gold electrode.[140,142]

5.2.3 Conducting Probe AFM (CP-AFM) Measurements

Topographic height imaging and bias dependent force measurements were performed using a commercially available atomic force microscope (MFP 3D, Asylum Research, Santa Barbara, CA) with a conducting probe module (ORCA, Asylum Research, Santa Barbara, CA). Platinum-coated silicon cantilevers (Mikromasch, San

Jose, CA) with a tip radius of curvature of ~35 nm and a reported spring constant of ~0.63 N/m were used in these experiments. The actual cantilever spring constant was determined with the built-in thermal noise method.[44] Cantilevers were cleaned in piranha solution (1:3 of 30% H_2O_2/98% H_2SO_4) for 2 minutes then rinsed in ultrapure water (>18 mΩ/cm) for 2 minutes followed by drying under vacuum. *Caution! Piranha solution is a very strong oxidant and is extremely dangerous to work with: gloves, goggles, and a face shield should be worn.*

All force measurements were obtained by recording force as a function of vertical piezo displacement position at a fixed DC bias. A maximum tip loading force of 5 nN gave sufficient contact and was used for all force measurements. Multiple surface positions with uniform monolayer formation were determined by imaging and selected for the force measurements. All force measurements were performed in an insulating bicyclohexyl solvent (99.0%, Fluka, Switzerland) in order to reduce water contamination and decrease the adhesion force caused by capillary forces between the AFM probe and sample due to a water layer formation on the tip-surface interface.[144] The force-displacement plots, i.e. force as a function of piezo position, were obtained at different fixed surface biases between -3 and 3 Volts with 0.1 V bias intervals. At each interval 10 repeated force plots were collected consecutively. Here two SAMs at each concentration were investigated, using at least 2 AFM probes per sample. At high bias and high-applied force the tip can induce irreversible morphological sample changes at the point of contact. In order to insure our measurements were reproducible, an image was collected on each region before and after every set of measurements. Only sample regions that showed no morphological changes were used in this study.

5.3 Results and Discussion

5.3.1 Characterization of mixed monolayers using cyclic voltammetry

Each SAM was characterized using cyclic voltammetry on an Au electrode functionalized using simultaneous adsorption by submerging the electrode in mixtures of solution mole fraction 0, 0.1, 0.23, 0.33, 0.43, 0.55, and 1 Fc. The data obtained matches previous work by Lee et. al., showing and increase in the current as the number of Fc molecules increases, as well as the appearance of a double peak, which is attributed to variations in surface concentration and molecular interactions within each binary monolayer.[140] Most importantly, the technique allows for quantification of Fc absorbed on the Au surface. In order to quantify the surface coverage of Fc (Γ_{Fc}) was calculated using equation 1,

$$\Gamma_{Fc} = \frac{Q_{Fc}}{nFA} \qquad (1)$$

where n is the number of electrons involved in the electron transfer process, F is Faraday constant, A is the surface area of the electrode, and Q_{Fc} is the charge associated with the Fc oxidation. The charge, Q_{Fc}, is found by integrating the anodic peak of the current vs. potential plot. For the 0.1 solution molar fraction the surface coverage was determined to be $1.75 \bullet 10^{-6}$ mol•m^{-2}, which corresponds to 39% of the maximum theoretical value ($4.5 \bullet 10^{-6}$ mol•m^{-2}) based on hexagonal packing and the ferrocene end-group modeled as a sphere of radius $6.6 \bullet 10^{-2}$ nm^2 (each Fc molecule occupying 0.35 nm^2), assuming 0.21 nm^2 is occupied by each alkyl chain the surface mole fraction is obtained.[140] The surface mole fractions were calculated and compared to the previous work by Lee showing strong agreement. The surface mole fractions ($Y_{Fc\text{-}surf}$) were found to be 0, 0.21, 0.32,

0.43, 0.54, 0.80, and 1.0 Fc for the solutions mole fractions ($Y_{Fc\text{-}sol}$) of 0, 0.1, 0.23, 0.33, 0.43, 0.55, and 1.0 Fc respectively. All mixtures showed an increased Fc adsorption to the surface as compared to the amount of Fc in the solution.

5.3.2 Morphology of mixed monolayers

The formation of uniform self-assembled monolayers (SAMs) of decanethiol (C_{10}) and mixed SAMs of ferrocenyl-1-undecanethiol (Fc) and C_{10} on ultraflat gold (Au) surfaces was verified using intermittent-contact mode AFM imaging. All monolayers displayed similar morphology to that in Figure 5.1, which displays a representative image for a 0.43 $Y_{Fc\text{-}surf}$. Images show the formation of domain boundaries, which arise due to molecular tilt of the molecules[46,47] and vacancy islands appear as holes or gaps in the

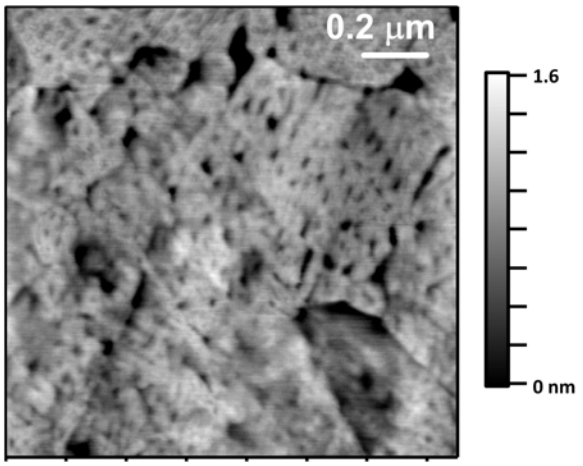

Figure 5.1. Representative height image of a 0.43 $Y_{Fc\text{-}surf}$ SAM. All SAM were of a similar morphology.

monolayer where the monolayer or Au substrate did not properly form.[31] The images also indicate that the monolayer is uniform and shows no physiosorbed material or aggregates

accumulated at the interface surface. The force displacement measurements were collected using regions where the surface was free of any aforementioned defects.

5.3.3 Capacitance force model for CP-AFM

Multiple force displacement curves were collected in an insulating bicyclohexyl organic solvent. Figure 5.2 shows a comparison of two force plots (retract data only) at 0 and 2 V bias collected on the pure C_{10} SAM. In a typical force measurement the tip approaches the surface until a predefined maximum loading force of 5 nN is reached and subsequently the probe retracts (plot shown in Fig. 5.2) to its original vertical position away from the surface. All force measurements were collected under a constant DC bias. The bar in the right side of the plot represents what we define as adhesion force at 2 V.

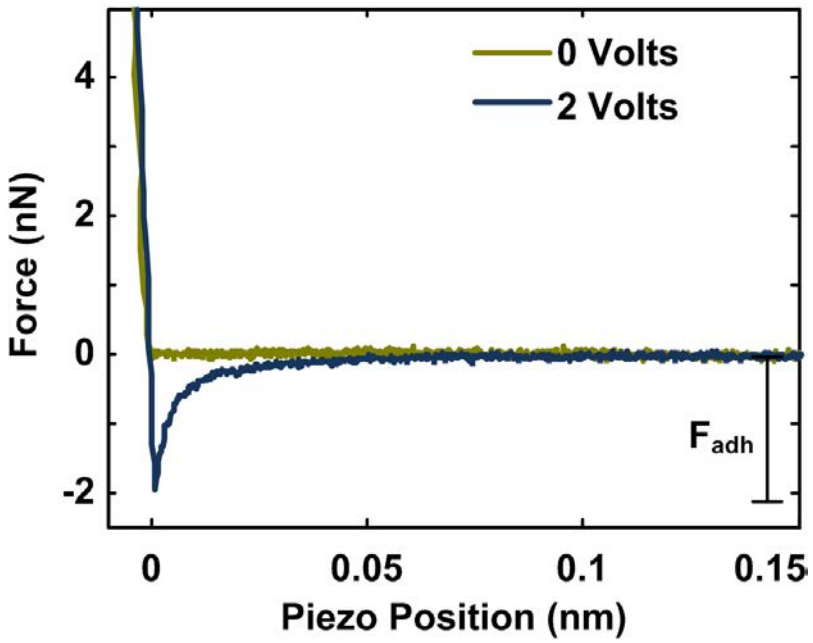

Figure 5.2. Representative force curves collected on pure C_{10} SAM, retract data only. Adhesion Force (F_{adh}) is the difference between the force far from the surface (200 nm) and the minimum interaction force (~2 nN for the measurement at a bias of 2 V).

The numerical value for adhesion force (F_{adh}) is defined as the average force away from the surface (~200 nm) minus the minimum force. At 0 bias (yellow-dashed line) the adhesion is due to intrinsic Van der Waals forces and is typically less that 0.2 nN whereas at 2 V (blue) the adhesion force increases to 2 nN due to the capacitance force between the biased tip and sample, adhesion force is bias-dependent.[32,145]

In order to probe the bias dependent adhesion forces, ten measurements at each bias were collected and the data averaged and the plot of the adhesion force *versus* bias for a pure C_{10} SAM is shown in Figure 5.3. Each cross is the average of ten replicate measurements. An increase in bias leads to a corresponding increase in force. As bias is applied across the junction between the tip and the conductive substrate there is a resulting electrostatic force, which is known as tip-sample capacitance force.[139] The conductive Au substrate and a truncated cone with a rounded apex (the tip) form a two-plate capacitor. The tip-sample capacitance can be approximated as the sum of three specific geometric contributions: the cantilever, tip body, and tip apex.[139] At large distances from the surface the contribution of the cantilever and tip body are relevant; however, they become negligible at short distances since the tip apex dominates the response.[139,146]When the tip and SAM are in contact the tip apex dominates the response and bias-dependent adhesion force (F_{adh}) can be described as[146]

$$F_{adh} = F_{\text{int}} + \mathrm{X}\left(V + V_{CPD}\right)^2 \qquad (2)$$

where X is,

$$\mathrm{X} = \pi\varepsilon_o \frac{R\varepsilon_r}{d} \qquad (3)$$

here F_{int} is the intrinsic adhesion force is primarily due to Van der Waals attractions, R is the radius of curvature of the tip, ε_0 is the permittivity of vacuum, ε_r is the relative

dielectric constant of the film, and d is the film thickness. The contact potential difference, V_{cpd}, would be zero if the work functions of both sample and tip were identical.[146,147]Contact potential difference is the bias required to null the electric field caused by the dielectric material in the junction, and changes due to the presence of surface dipoles and variations in surface packing of the distinctive monolayers.[146,148] The averaged data for the C_{10} SAM was fit using equation 2, returning values of F_{int} = 0.1 ± 0.01 nN, X = 0.44 ± 0.01 nN•V^{-2}, and V_{cpd} = 496 ± 7 mV. The data shows no deviations from the fit to equation 2. The contact potential difference corresponds to the molecules overall surface dipole moment pointing toward the surface causing a decrease in the workfunction.[141,149]These values are consistent with previous work on C_{10} SAMs.[141]

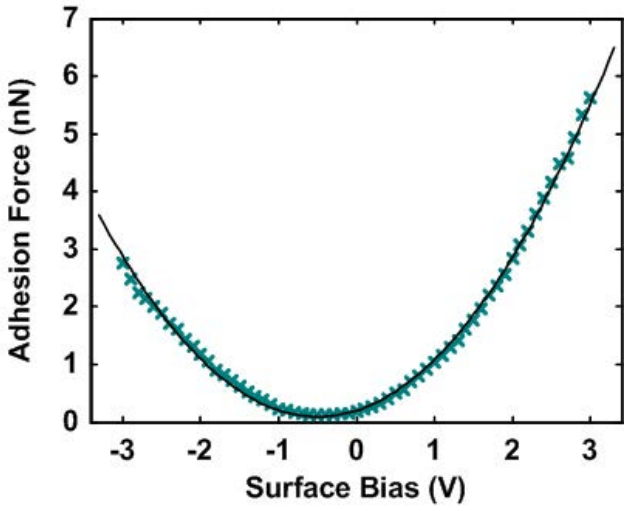

Figure 5.3. Adhesion force vs. bias for a pure C_{10} SAM.

Figure 5.4 shows six plots of adhesion force *vs.* bias for the 5 mixed fractions and pure Fc SAM. The standard deviation in these plots is equal to or smaller than the size of the crosses, the average standard deviation is less than 0.3 nN in all plots. All data was

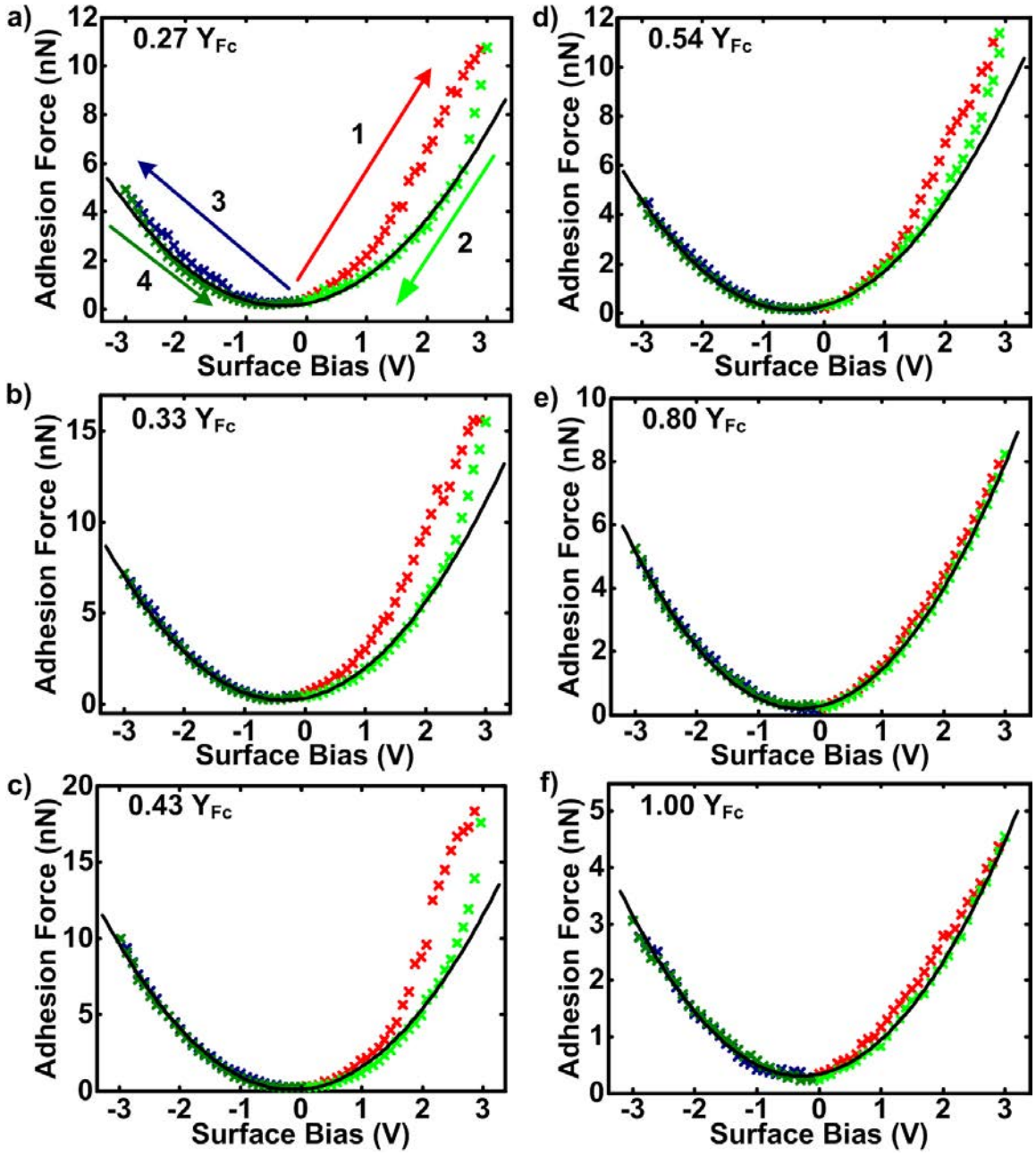

Figure 5.4. Adhesion force vs. surface bias for different $Y_{Fc\text{-}surf}$ a) 0.27, b) 0.33 c) 0.43 d) 0.54 e) 0.80 and f) 1.00. Numbered arrows in figure 4a represent the direction in which the bias was swept. Ten measurements were collected at each bias and the standard deviation was smaller than the size of the symbol.

collected as shown in figure 5.4a, where the bias was swept first from 0 to 3 V (red), then from 3 to 0 V (light green), followed by 0 to -3 V (blue) and finally from -3 to 0 V (dark green). The reverse collection was done as well, where first the bias was swept from 0 to -3 V showing similar trends. It is obvious that there are some significant concentration effects on the bias-dependant adhesion forces. Focusing on figure 5.4 a-c where the $Y_{Fc\text{-}surf}$ ranges from 0.27-0.43 we see that as the amount of Fc increase there is an increase in the adhesion force between the tip and sample. The maximum adhesion force at 3 V for the 0.27, 0.33, and 0.43 $Y_{Fc\text{-}surf}$ is 11.1, 15.8, and 22.3 nN, respectively. Additionally shown in Figure 5.4 a-c a deviation of the two sweeps at the positive bias is observed (red crosses), which only occurs when the bias is increasing from 0 to +3. However the opposite trend is observed in Figures 5.4 d-f, as the concentration increases to molar ratios greater than 50% Fc, the bias-dependent adhesion force decreases as the number of Fc molecules increases. This deviation only occurs at the positive surface bias and is observed on all Fc containing samples; therefore because this is not observed for the C_{10} SAM we attribute the deviation to the oxidation of the ferrocenyl moiety.

The data in figure 5.4 a-f represented as green crosses were fit to equation 2, using the portion from -3 to +3 V, which provided the best fit to the capacitance force model. For all samples the intrinsic adhesion force was less than 0.2 nN from all fits. Figure 5.5 shows the fit values both X and V_{cpd} as a function of ($Y_{Fc\text{-}surf}$). Figure 5a shows the fractions below 50 percent Fc show an increase in X with in increase in Fc followed by a decrease in X for fractions greater than 50 percent. Additionally, the V_{cpd} decreases as the amount of Fc increases, with a small increase in V_{cpd} at just greater than 50 percent, which then decreases again as the amount of Fc increases. These variations in the bias

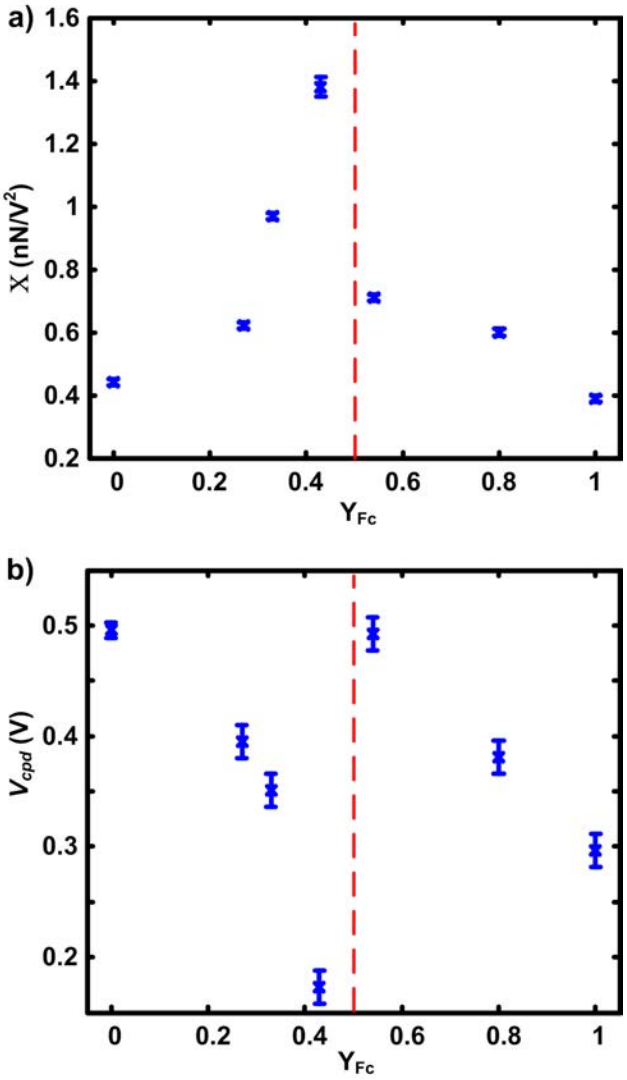

Figure 5.5. Plot of a) X (nN/V^2) vs. $Y_{Fc\text{-}surf}$ and b) V_{cpd} vs. $Y_{Fc\text{-}surf}$ obtained from the fits to equation 1. Red line represents 0.5 $Y_{Fc\text{-}surf}$.

dependent adhesion force can primarily be attributed to the permanent and induced overall dipole moments of the SAM as well as minor differences in the contact potential are due to variations in monolayer packing.[149] For example, a dipole perpendicular to the substrate pointing toward the surface corresponds to decrease V_{cpd}, one pointing away corresponds to a increase V_{cpd}.[149] The three major contributing dipoles are the Au-S

induced dipole, the alkane chain dipole, and of the ferrocene endgroup dipole. The induced dipole which arises from the charge transfer between the Au and S atom points negative toward the sulfur atom and has a small contribution to the V_{cpd}, while the hydrocarbon chain dipole moment points toward the sulfur dominating the response when C_{10} is considered.[141] This inclusion of increasing amounts of C_{10} causes a decrease in V_{cpd} as it is defined in this work. [141,149] Therefore, the intrinsic dipole moment of the ferrocene is pointing away from the surface, (toward the Ferrocene endgroup) causing the increase in the V_{cpd} as the amount of Fc in the junction increases.[141,149] Previously a shift in the work function for this binary system was also reported using Kelvin Probe Microscopy; similarly, as the number of ferrocenes present on the surface increased the work function of the sample increased.[141]

As the surface molar fraction becomes greater that 50% this trend is no longer observed. The primary difference being ferrocene endgroups are forced to contact neighboring ferrocene endgroups as the fraction of Fc increases. An increase in the X value is expected because the magnitude of the surface dipoles in the monolayer changes as the number of Fc increase on the surface and a decrease in the V_{cpd} because the there are more molecules perpendicular dipole moment pointing away from the surface, however this is not the case. When the Fc molecules proximity increases, depolarization effects start to occur,[150] and there is a decrease in attractive forces, as can be seen in figure 5.4 d-f.

5.3.4 Quantifying the number of oxidized molecules at the contact junction

The hysteresis, which is observed only at the positive bias when the bias is swept from 0 to +3 V, was an unexpected observation and has not been reported in previous literature. A significant increase in the adhesion force on the positive sweep from 0 to ±3 (red crosses) is attributed to the oxidation processes where the ferrocene moiety undergoes oxidation from a neutral oxidation state to a +1 oxidation state inducing a positive charge on the surface.[139,140] As can be seen the additional attractive force in observed only at the positive surface bias and is due to the oxidation of the Fc moiety.[139] This occur as a hole transfer from the gold to the HOMO level of the Fc, which oxidizes the molecule followed by hole tunneling from the molecular level to the tip (measured as current) or charge dissipation after the tip leaves the surface.[139] The molecule then returns to a neutral state. The positive surface bias provides a stabilization electric field for the formation of Fc cations; similar to counter ions in an electrolyte solution, which does not happen at negative surface biases, which is why there is no force increase on that side.[139] The adhesion force between the negatively biased tip and positively biased sample then increases due to attractive electrostatic forces between tip and sample and which increases as Fc concentration increases. This indicates that the attractive forces can be correlated with the number of oxidized species induced on the SAM surface. We note, however, that accurate quantification is possible only when molecules are well separated in surface molar ratios less than 50 % Fc, as discussed below.

The $Y_{Fc\text{-}surf}$ greater than 50% shows a decrease in redox force as the amount of ferrocene increase. For the samples the ferrocene end-groups are not separated and begin

to interact with each other. As the molecules become closer to each other, it becomes more difficult to induce a change in oxidation state on neighboring molecules.[140] Two positively charged ferrocene groups directly adjacent to each other would cause repulsions between molecules. With less molecules oxidized there is a decrease in the redox force as can be observed in Figure 5.4 d-f. Additionally as molecules become closer charge dissipation can occur. If charges dissipate from the contact area the interaction force would decrease as observed. Charge repulsion and dissipation contribute to the decrease in redox forces observed in monolayers containing more than 50 % Fc.

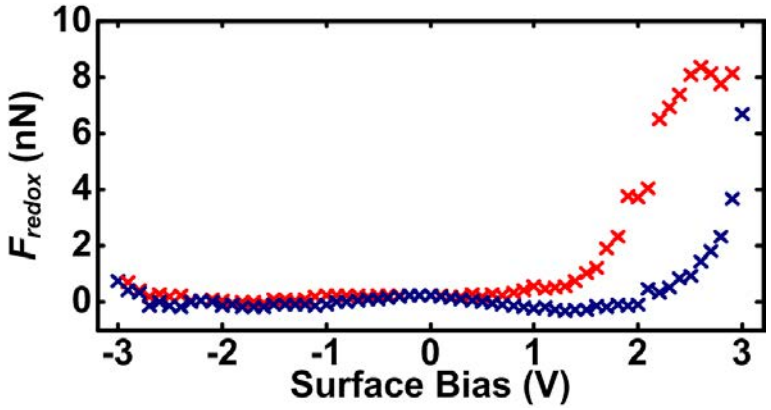

Figure 5.6. Redox adhesion force vs. surface bias for the 0.43 surface fraction Fc. Red crosses represent bias sweeps from 0 to ±3 V and blue crosses represent bias sweeps from ±3 to 0 V.

In all fractions the observation that this trend is dependent on the direct the bias is swept is very curious. As the bias is swept from +3 back to zero there is a decrease in the adhesion force. This indicates that the Fc endgroup is apparently locked in a state that can no longer undergo redox transitions. These measurements were completed multiple times over the same sample location indicating this is not sample degradation but that the

monolayer can recover and give the same interaction. The deviation at the positive bias will reappear in less than 60 seconds.

Redox adhesion force is defined as the difference between the fit to equation 1 and the data in Figure 5.5. In Figure 5.6, redox adhesion forces vs. surface bias are shown for the all mixed SAMs, the dots represent an increase in the bias from 0 to ±3 volts, and cross symbols denote a decrease in bias form ±3 volts to 0 same as Figure 5.5. This then is the force attributed to the electrostatic attract due to the presence of positively charged Fc endgroups. To address the extent of interface charging, number of charges, Q, induced or trapped on the surface can be quantified using equation 4,[151]

$$Q = \frac{F_{redox}\left(d/\varepsilon_r\right)}{2V} \tag{4}$$

where V is the bias, F_{redox} is the redox force at a specific bias, d is the film thickness and ε_r is the film relative dielectric constant. At a surface bias of 2.8 volts, molecular length of 2.37 nm and assuming a dielectric constant of 2,[139] we can determine the number of charges induced on the surface. Using the redox force as defined above, there are 6, 9, 12, 4, 1, and 1 charges are induced for the 0.27, 0.32, 0.43, 0.54, 0.80, and 1.00 $Y_{Fc\text{-}surf}$ respectively. At surface molar fractions greater than 50 percent the observed number of charges is an effective value as the actual number of charges may be larger due to charge dissipation and monolayer depolarization effects the actual number of induced charges can't be determined.

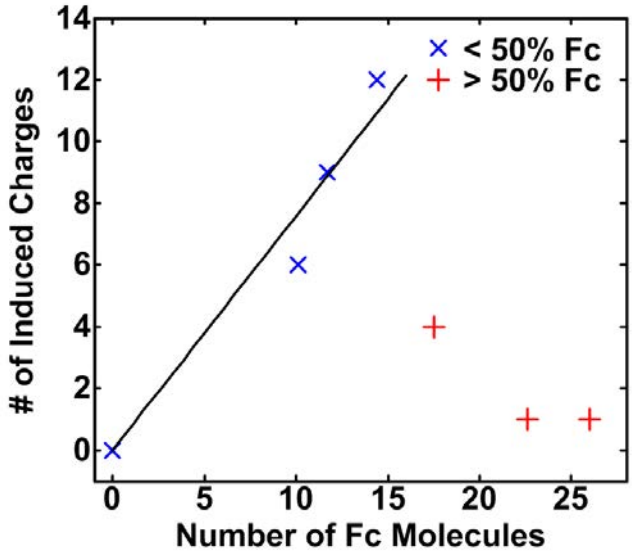

Figure 5.7. Number of molecules vs. number of charges induced on the SAM surface.

Using the Hertzian elastic contact model, which assumes a sphere of radius *r* indenting an elastic film, the contact area and therefore number of Fc molecules can be estimated.[58,59] According to the model, the mechanical contact radius *a* between a spherical tip of radius *r* penetrating into a uniform elastic film may be estimated as

$$a^2 = \left(\frac{Fr}{K}\right)^{2/3} \qquad (5)$$

where *F* is the loading force and *K* is an effective modulus equaling

$$K = \frac{4}{3}\left[\frac{1-\nu_{Pt}^2}{E_{Pt}} + \frac{1-\nu_S^2}{E_S}\right]^{-1} \qquad (6)$$

and E_s, ν_s, E_{Pt}, and ν_{Pt} are the Young's modulus and the Poisson's ratio of the sample and the Pt-coated AFM tip, respectively. The Poisson ratio for most materials is between 0.25 and 0.5,[139,31,58] and thus assuming $\nu_{Pt} \approx \nu_s \approx 0.33$, an effective modulus can be approximated as $K=1.5E_{Pt}E_s/(E_{Pt}+E_s)$. Although appropriate measured values for

elasticity modulus are not available, assuming E_{Pt}=170 GPa,[58] E_s=7 GPa,[31],[59] a force of 5 nN and effective tip radius of curvature calculated from C_{10} data from fit parameter X (assume a dielectric constant of 2) of 10.7 ± 0.2 nm, the estimated contact area is 9.5± 1.3 nm^2. Using the surface density of Fc obtained from cyclic voltammetry there are 10, 12, 14, 18, 23, and 26 Fc molecules in the contact area for the 0.27, 0.32, 0.43, 0.54, 0.80, and 1.00 $Y_{Fc\text{-}surf}$ respectively. Figure 5.7 shows the number of charges vs. the number of molecules in the contact junction. In samples below 50 percent Fc (blue crosses) only a fraction of the molecules are oxidized, as shown by the linear fit to the blue crosses, with a slope of 0.76, meaning approximately 76 percent of the molecules are oxidized in all cases. As expected, fractions greater than 50 percent (red crosses) show a large decrease in the number of induced charges as expected due charge dissipation and monolayer depolarization.

5.4 Conclusions

In summary, the CP-AFM has been used to probe localized redox transitions at the nanoscale for mixed SAMs of 11-ferrocenyl-1-undecanethiol (Fc) and 1-decanethiol (C_{10}). The mixed SAMs showed increase in adhesion forces and contact potential shifts as the fraction of Fc increased, which is attributed to changes in the perpendicular orientations of the surface dipoles of the molecules in the junction. The $Y_{Fc\text{-}surf}$ greater that 50% Fc SAMs do not follow this trend due to depolarization affects with neighboring ferrocene end-groups. Upon oxidation of the ferrocene moiety there is an increase in the adhesion force due to electrostatic forces between the tip and SAM. The number of charges induced on the surface has been quantified using the redox adhesion forces. This

model can be used to quantify localized redox transitions of electroactive species at nanoscale metal-SAM-metal junctions.

CHAPTER 6
SELF-ASSEMBLED ENZYMATIC MONOLAYER DIRECTLY BOUND TO A GOLD SURFACE: ACTIVITY AND MOLECULAR RECOGNITION FORCE SPECTROSCOPY STUDIES

6.1 Introduction

Molecular recognition force spectroscopy (MRFS) is a specific application of atomic force microscopy (AFM) measurements wherein the strength of ligand-receptor interactions, such as that between an enzyme and its inhibitor, is probed. In a typical experiment, the AFM probe and substrate are covalently modified to immobilize the ligands and receptors, respectively.[152,153] If the surface-bound receptor is a biomolecule such as a protein, a spacer is commonly used to assure separation between the biomolecule and surface.[43,154-156] These studies not only require a complex design and assembly, but the flexibility and dynamics of the spacer often interfere with the AFM or molecular tweezers measurements.[43,154,157,158] A potentially simpler design, however, can be envisioned wherein the biomolecule is immobilized on a surface directly forming a self-assembled monolayer (SAM) through a direct interaction with the surface. Furthermore, close proximity of biomolecules may provide a unique stabilization that is absent in the solution, and may better resemble the crowdedness cytosolic enzymes face

---

This chapter was published in the *Journal of the American Chemical Society* [Ditzler, L., Sen, A., Kohen, A. and Tivanski, A. (2011) *Self-assembled enzymatic monolayer directly bound to a gold surface: activity and molecular recognition force spectroscopy studies,* 133, pp. 13284] (Ditzler and Sen have contributed equally to this work)

in vivo. If the ligand of interest is also bound to the AFM tip, the interaction between a ligand and the receptor can be studied using MRFS by pulling the tip away from the ligand-receptor complex until the applied force overcomes the interaction force and leads to dissociation of the complex. Such direct surface functionalization could potentially offer advantages in other experiments that require minimal distance between the surface and an enzyme active site (e.g., electrical conductivity[159] or catalyzed redox reactions using the surface as an electrode.[160,161])

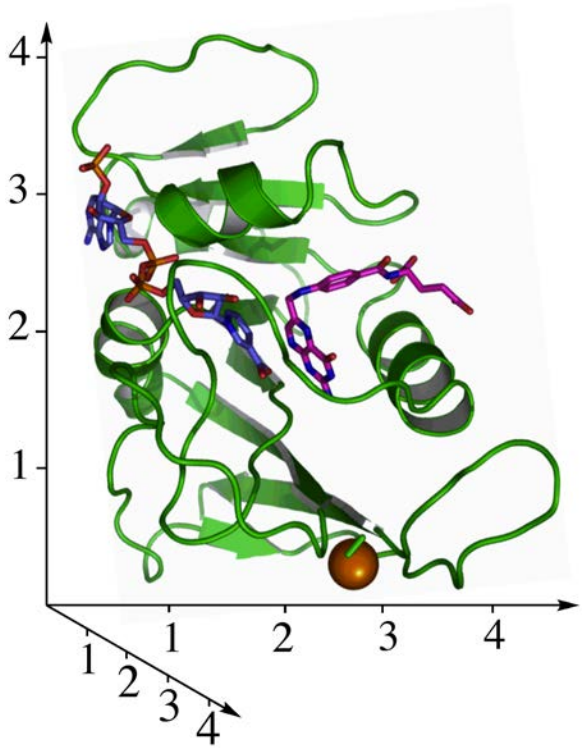

Figure 6.1. The dimensions in nm of ecDHFR in complex with $NADP^+$ (blue) and folate (magenta) (PDB ID 1RX2)[162]. The thiol bound to the gold (C152) is highlighted as sphere.

Here we present the use of MRFS to directly study the binding forces involved in the interaction of *E. coli* dihydrofolate reductase (ecDHFR) with a tight-binding inhibitor,

methotrexate (MTX). DHFR catalyzes the transfer of the pro-*R* hydride from C4 of reduced nicotinamide adenine dinucelotide phosphate (NADPH) to the *si*-face of 5,6-dihydrofolate (DHF), forming *S*-5,6,7,8,-tetrahydrofolate (THF) and $NADP^+$. This vital housekeeping enzyme is targeted by many chemotherapeutic and antibacterial agents. Due to its small size, lack of metals or S-S bonds, and simple catalyzed chemistry, ecDHFR has become a model system for studies of enzyme folding, activity, and dynamics, for both experimentalists and theoreticians.[163-170] Consequently, ecDHFR is a suitable and interesting candidate for the development of new MRFS studies. The wild type ecDHFR enzyme has a single cysteine (C152) on the outer surface opposite to and remote from the active site, and can, in principle, be used to bind the enzyme directly to a gold surface for use in MRFS experiments. The only other cysteine in the enzyme (C85) is located in an internal region of the protein and is unlikely to bind to the gold surface while the enzyme is folded in its globular conformation. Fig. 1 presents the dimensions (nm) of ecDHFR as it would be bound to the gold surface through C152. In studies of surface-immobilized proteins, the use of linkers such as polyethylene glycol (PEG) or DNA to tether the biomolecules to surfaces is widespread.[154-156,171-173] However, the use of these linkers can be disadvantageous in studies of enzyme folding, dynamics, or function as the response becomes convoluted and in some cases even limited by the linker itself.[43,154,156,157] In particular, the polydispersity and nonlinear elasticity of the linker can significantly affect the dissociation rates and magnitudes of unbinding interactions.[1] The rupture forces measured without a spacer are typically larger,[2] hence improving signal-to-noise ratio in MRFS experiments. Furthermore, the use of spacers has been shown to decrease lateral resolution, thus diminishing the likelihood of single-

molecule interactions.[174,175]The ability of ecDHFR to form a covalent bond between Cys152 and gold allows us to immobilize the enzyme onto the Au surface forming a SAM without the mediation of linkers or spacers. The SAM design results in closely spaced enzyme molecules that are more crowded than diluted enzyme used in most *in vitro* experiments. Nonetheless, it provides a closer approximation of crowded cell conditions.[176]

Proteins are conformationally labile molecules, and many studies indicate an important role of protein dynamics in the catalytic performance of enzymes.[177,178] AFM measurements on enzymatic SAMs can thus explore the effect of monolayer organization on enzymatic activity and conformational behavior.[179] Furthermore, the new method may provide insight into the effect of this unique environment (gold surface at the bottom, several neighboring proteins within the surface plane, and water molecules above) on the enzymatic function (*i.e.* enzyme catalysis and inhibition). To the best of our knowledge, direct demonstration of the catalytic activity in an enzymatic SAMs on gold surface has not been reported in the literature to date.

6.2 Experimental

6.2.1 Materials

All reagents were purchased from Sigma-Aldrich, unless otherwise noted. *E. coli* dihydrofolate reductase (ecDHFR) was expressed and purified according to the procedure of Cameron et al.[180] [carbonyl-^{14}C] $NADP^+$ was synthesized from [carbonyl-^{14}C] nicotinamide (55mCi/mmol from Moravek) and $NADP^+$ using porcine brain NADase and was then reduced to ^{14}C-NADPH with *Bacillus megaterium* glucose dehydrogenase. Reaction progress at each step of the synthetic procedure was quantified by analytical

RP-HPLC on a Beckman-Coulter System Gold instrument (model 126), using a Supelco Discovery C-18 column (250 x 4.6mm i.d., 5μm particle size) and the gradient elution method described elsewhere.[181] Separated peaks were analyzed by an online Beckman UV-vis detector (model 168) and a Packard 500TR Series flow scintillation detector. The semipreparative HPLC method described previously[181] was used to purify the final product. Purified material was divided into 300,000 DPM aliquots and stored at -80°C for short-term (15 days). Finally, 7,8-dihydrofolate was synthesized from folic acid by the method of Blakley.[182]

6.2.2 ecDHFR-functionalized gold surface preparation

Ultraflat gold (Au) surfaces were fabricated using the template-stripping method.[43] Briefly, thermally evaporated gold surfaces on freshly cleaved mica substrates (V-I grade, SPI Supplies, Westchester, PA) were glued face-down using an epoxy glue (Epotek 377, Epoxy Technology, Billerica, MA) on clean glass slides. The surfaces were then thermally cured in an oven for at least 2 hours at 150 °C. Finally, the ultraflat Au surfaces were obtained by stripping the mica from the Au in THF. The ultraflat Au surfaces were then rinsed in ethanol and dried in a stream of N_2 gas. Subsequent AFM height measurements of the ultraflat Au surfaces resulted in a typical root-mean-square roughness of less than 0.5 nm over 5 μm^2 area. ecDHFR was then self-assembled on ultraflat gold surface by submerging it into a 10 μM solution of ecDHFR in MTEN buffer (100mM NaCl, 50mM MES, 25mM Tris and 25mM ethanolamine; pH 7.5 at 25°C) for 1 hour followed by rinsing three times with MTEN buffer to remove any physisorbed enzymes. All samples were stored in MTEN buffer at 4 ˚C and used within 4 hours of preparations.

6.2.3 ecDHFR monolayer determination

To verify the formation of a ecDHFR monolayer on the gold surface, the AFM (Asylum Research, Santa Barbara, CA) was used to scratch a small region on the sample surface. Using a cantilever with a nominal spring constant of 0.65 N/m (Micromasch, San Jose, CA) and contact mode, a force of ~50 nN was used to scan a small area, removing enzymes bound to the surface. Then the less destructive AC mode scan was preformed on a larger area surrounding the scratched area. The image revealed a small box in the center of the image where all material had been removed (Fig. 3a). The scratched square area was then used to determine the thickness of the enzyme layer.[155,183,184] A height variation of ~4 nm, matching the hydrodynamic diameter, confirms the formation of a nicely packed self-assembled monolayer.

6.2.4 Assessment of k_{cat} for ecDHFR monolayer bound to ultraflat gold surface

All kinetic measurements were carried out in MTEN buffer (pH 7.5). Au-bound ecDHFR surface density was calculated assuming each enzyme is a sphere of 4 nm diameter (Fig. 1) occupying a surface area of 12.6 nm^2. The surface density was calculated to be 0.13 $pmol/mm^2$ for a uniform tightly packed monolayer of ecDHFR. The immobilized ecDHFR was allowed to react with 50 μM [carboynyl-^{14}C] NADPH and 1 mM dihydrofolate at 25°C in MTEN (pH 7.5), and aliquots were removed from the reaction mixture at different time-points and quenched with 0.5 mM methotrexate to yield samples with fractional conversions ranging from 1-10% (fractional conversion was determined from the distribution of ^{14}C between NADPH and $NADP^+$ peaks, Fig X.4). Samples were analyzed using a RP-HPLC (Supelco Discovery C-18 column used as noted in *Materials* section) with a Packard 500TR Flow Scintillator Analyzer (FSA). V_{max}

was determined by linear fit to at least three time points with fractional conversions below 10%, under saturation of both substrates, and was indeed the same at different concentrations ranging from 200 to 500μM of NADPH and 5.6 to 10mM of DHF. k_{cat} was calculated by dividing V_{max} by the concentration of enzyme that was determined as described above. All reactions were performed at least in triplicate, and rates determined from different samples were normalized to the surface area per sample.

6.2.5 AFM probe functionalization

AFM probes with a nominal spring constant of 0.06 N/m (Veeco, Santa Barbara, CA) were functionalized with methotrexate by first forming an amine-terminated Si_3N_4 tip followed the formation of an amide bond with methotrexate. A 5 M solution of ethanolamine in dry DMSO was heated to 70°C then cooled to room temperate and a few molecular sieve beads were added. The AFM probe was incubated in the ethanolamine solution overnight.[155,172,185] Subsequently, the amine-terminated tip was rinsed in DMSO for 5 minutes, followed by ethanol for 5 minutes. Next, methotrexate (0.66 mM) was first dissolved in 5 ml DMSO, then mixed with a 5 ml aqueous solution of EDC (5 mM) and NHS (1 mM), and the solution was adjusted to a pH of 8.2 using 1 M NaOH.[172,185] The AFM probe was exposed to the solution for 30 minutes, and then washed with DMSO and ethanol for 5 minutes each. All functionalized AFM probes were used the same day as prepared and never stored more than 24 hours.

6.2.6 MRFS experiments

Multiple force rupture measurements were performed on the ecDHFR-functionalized gold using the MTX-functionalized tip. The tip and sample were loaded into the AFM (Asylum Research, Santa Barbara) and the individual tip spring constant

was determined using a thermal noise calibration.[44] The measurements were performed using force-mapping mode, collecting measurement over a large area of the sample. First the dwell time was varied between 0 and 1 second until the maximum rupture force was discovered.[186] All measurements were collected at a tip velocity of 2 μm/sec, a loading force of 500 pN, and a force distance of 250 nm. All measurements were collected in MTEN buffer (pH 7.5) to reduce capillary adhesion and stabilize the enzyme.

Each data set was analyzed to acquire the most representative result. Multiple unbinding force measurements were collected on each sample and plotted as a distribution histogram. Before these distributions could directly be compared it was filtered to reduce poorly representative data. For the subsequent data sets any interaction which occurred at tip-sample separation greater than 20 nm was removed from the sample.[187] This removed 2 and 8 percent of the total data for the active enzyme interactions and MTX-blocked enzyme interactions, respectively. The obtained distributions were plotted and fit to a Gaussian distribution.[156,184,188-190]

6.2.7 Assessing the number of ecDHFR molecules probed per contact junction

Using the Hertzian elastic contact model, the contact area and therefore number of enzymes can be estimated.[31,58] According to the model, the mechanical contact radius a between a spherical tip of radius r penetrating into a uniform elastic film may be estimated as

$$a^2 = \left(\frac{Fr}{K}\right)^{2/3} \quad (1)$$

where F is the loading force and K is an effective modulus equaling

$$K = \frac{4}{3}\left[\frac{1-\nu_t^2}{E_t} + \frac{1-\nu_S^2}{E_S}\right]^{-1} \quad (2)$$

and E_s, v_s, E_t, and v_t are the Young's modulus and the Poisson's ratio of the sample and the silicon nitride AFM tip, respectively. The Poisson ratio for most materials is between 0.25 and 0.5,[31,58,144] and thus assuming $v_t \approx v_s \approx 0.33$, an effective modulus can be approximated as $K=1.5E_tE_s/(E_t+E_s)$. The elastic modulus of the silicon nitride tip is 285 ± 5 GPa.[191] The E_s was measured using the AFM nanoindentation technique and found to be 30 ± 10 MPa.[192] The tip radius of curvature was 10 ± 5 nm, estimated contact area is 72 ± 20 nm^2. Using the estimated surface density of ecDHFR as described above, there are 6 ± 2 enzymes in the contact junction.

6.3 Results and Discussion

6.3.1 Monolayer Formation

In order to use MRFS to measure the interaction between the ecDHFR and MTX we must first form and characterize the ecDHFR monolayer. Fig. 6.2 shows a schematic representation of the MRFS experimental setup utilized herein.

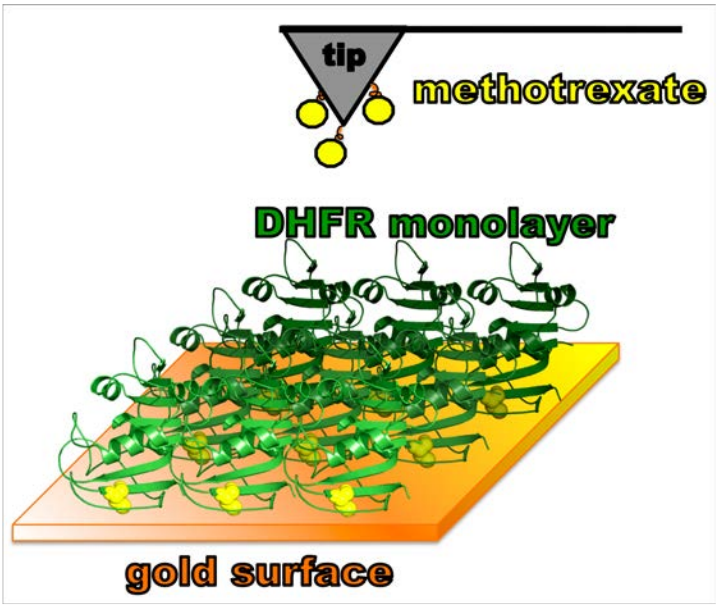

Figure 6.2. Schematic cartoon of the experimental setup.

For surface functionalization, ultraflat Au surfaces were immersed in a 10 μM ecDHFR solution in MTEN buffer (pH 7.5 at 25°C), allowing the enzyme to self-assemble and covalently bind to the gold substrate. Samples were incubated in that solution for 1 hour and then rinsed several times in MTEN buffer to remove any physisorbed, non-covalently bound protein. The formation of a homogenous monolayer was confirmed by AFM images (Fig. 6.3a,b). Prior to all MRFS and activity studies, the ecDHFR-functionalized surfaces were scratched with the AFM tip to confirm the presence of an ecDHFR monolayer and to determine its thickness, as shown in the AFM height image in Fig. 6.3a and the corresponding cross-section profile in Fig. 6.3b. The

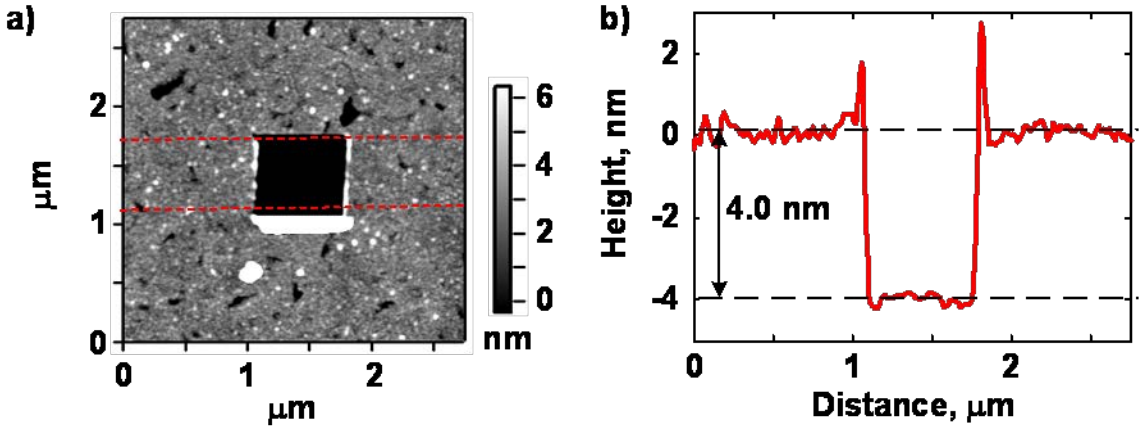

Figure 6.3. AFM height image of a) ecDHFR monolayer. The central region has been scratched to examine monolayer thickness. b) Averaged cross section of 60 horizontal line scans between the red lines shown in (b).

scratch test involved the application of a force greater than 50 nN and imaging in contact mode in order to remove all material in a specified region.[10,183,184] By comparing height variations of the monolayer in the scratched region versus the surrounding unscratched region, we found a height variation of approximately 4 nm, consistent with the size of

ecDHFR along the vertical dimension of Fig. 6.1. The scratch test therefore supported a single uniform monolayer of ecDHFR molecules formed in all samples used in this study.

6.3.2 Enzyme Activity

Enzyme-immobilization may alter enzyme activity and behavior significantly from the solution behavior of the same protein.[193] Furthermore, one of the main reasons for the use of spacers in surface-immobilization of enzymes is to address the effect of the surface on enzyme folding, dynamics, and consequently function. In this case, the direct immobilization of the ecDHFR on the gold surface required careful examination of the catalytic activity prior to investigating MTX dissociation *via* MRFS. To conduct the activity assay of the ecDHFR-functionalized Au surface, we labeled NADPH with ^{14}C at

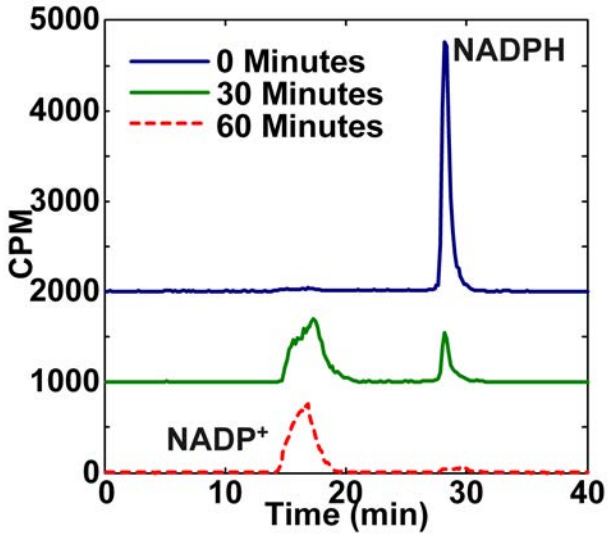

Figure 6.4. Radiogram showing RP-HPLC separation of products and reactants from kinetic assay of DHFR activity under monolayer conditions. Solid blue line is starting material (*i.e.* reaction mixture at 0 min); solid green line is the reaction mixture at 30 min; dashed red line is the reaction mixture at 60 min. Units on the *y*-axis are in counts per minute (CPM) and are shifted by 1000 and 2000 CPM for the 30 and the 60 min radiograms, respectively

the amide carbonyl to obtain [carbonyl-^{14}C] NADPH, and used this labeled substrate to follow ^{14}C-NADPH formation as a function of time, using HPLC and liquid scintillation analysis as described before.[181] Notably, a conventional UV-Vis activity measurements at 340 nm were not useful with the gold-immobilized enzyme due to the presence of the solid plate in the reaction mixture (i.e. heterogeneous, surface catalysis). Figure 6.4 show radiogram of the reaction over a period of an hour, as you can see there is significant formation of product $NADP^+$ confirming the enzyme is active. To better quantify the activity the fractional conversion (distribution of NADPH and $NADP^+$ in peaks, Fig 6.4 over time intervals with less than 10% were measured. V_{max} was then calculated from the data as descibed in section *6.2.4* and a k_{cat} value of 8.8 ± 1.2 per second was determined using an ecDHFR concentration of 10 pM.

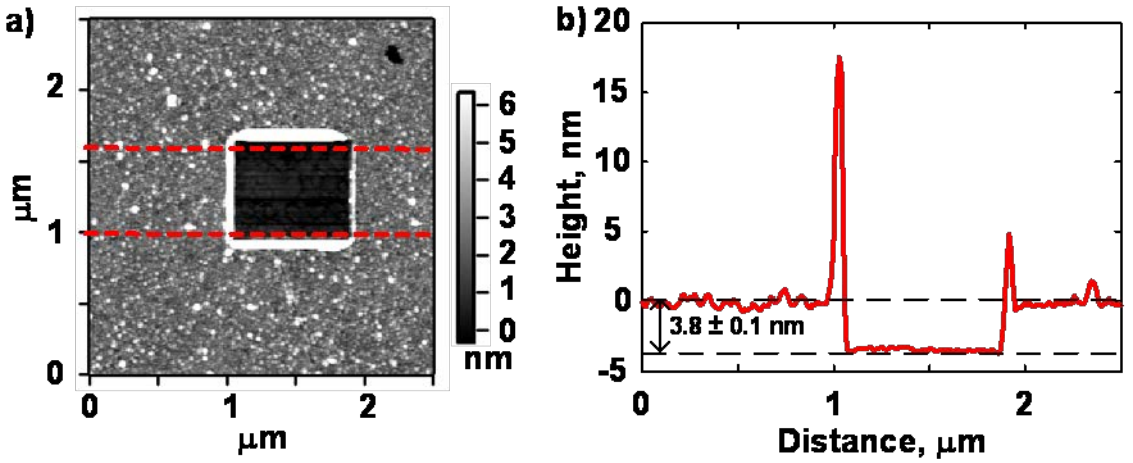

Figure 6.5. AFM height image of a) ecDHFR monolayer after activity test, center region has been scratched to examine monolayer thickness. b) Average cross section of scratched region in (a).

Remarkably, this rate is about the same k_{cat} as that measured for ecDHFR under the same conditions in solution (10-12 s^{-1}).[194] Since in solution the rate is determined by

dissociation of the product tetrahydrofolate,[194] the k_{cat} of the Au-immobilized enzyme suggests that the dissociation was not altered and the overall functionality of the enzyme is similar to that in solution. This is especially important as the MRFS experiments presented below examined the dissociation of this product's analog, MTX. Additionally, the scratch tests performed after the kinetic assay (Fig. 6.5) show no changes in monolayer structure. These tests further confirmed that the monolayer was stable throughout the activity measurements.

6.3.3 Probing Molecular Interactions Using MRFS

Once we had confirmed that the Au-bound ecDHFR monolayer was indeed active, we used MRFS to directly probe the interaction forces between ecDHFR and its pM inhibitor, MTX. Initially, three control measurements were conducted: 1. the interaction between a bare, unfunctionalized Si_3N_4 tip and gold-bound ecDHFR; 2. the same measurement for the MTX-functionalized tip; and 3. unfunctionalized Si_3N_4 tip and enzyme.[155,172,185] Then, the interaction between the tip-bound MTX and gold-bound ecDHFR was studied. Finally, the gold-bound ecDHFR was immersed in a 220 μM MTX solution in MTEN buffer and equilibrated for 20 minutes to saturate all active-sites with MTX, and then interaction forces between tip-bound MTX and the gold-bound ecDHFR-MTX complex were measured. The last experiment was critical to verify that the interaction between the MTX-tip and functionalized gold surface is active-site specific.

For MRFS studies, multiple force measurements at various sample positions were collected.[186] Upon retraction, the intermolecular contacts between gold-bound ecDHFR (or the DHFR-MTX complex) and the tip-bound MTX are ruptured as the probe moves away from the surface. The rupture force is defined as the maximum force required to

remove the probe from the contact with the sample. To establish an optimal dwell time for the tip in the contact with the sample, force measurements were performed at several dwell times ranging between 0 and 1s, while keeping the tip-velocity (2 μm/s) and maximum loading force (500 pN) constant. Fig. 6.6a shows representative force-plots (retract data only) for measured interactions at three selected dwell times of 0, 110 and 510 ms; Fig. 6.6b shows the corresponding distribution of rupture forces for these dwell times. Both figures clearly demonstrate the increase in rupture force with increasing

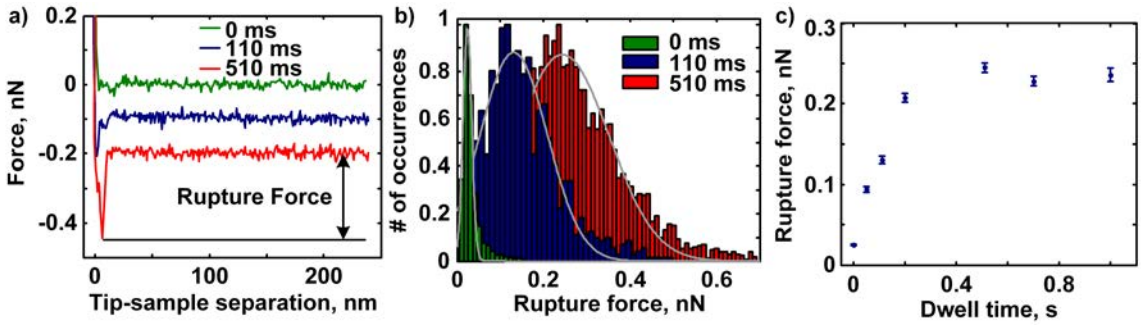

Figure 6.6. Representative force measurements (retract data only) of interactions at a) dwell times of 0(green), 110(blue) and 510(red) ms. b) Distributions of rupture forces at dwell times of 0, 110 and 510 ms. c) Mean rupture forces versus dwell time at a velocity of 2 μm/sec.

dwell time. Fig. 6.6c shows the mean rupture force as a function of dwell time. At dwell time of 0.51 s or greater, a maximum rupture force is reached for the interaction between ecDHFR and MTX. Hence, the dwell time of 0.51 s was selected as the optimal time for the MRFS experiments described below. We note the dependence of the rupture force as a function of the dwell time observed here is similar to that for vancomycin and D-Ala-D-Ala interactions, and can be used to estimate an apparent association rate constant.[9] Following similar approach, the interaction time for half-maximum probability of binding

was estimated as 0.08 sec, and the association constant k_{on}= 2.5 $M^{-1}s^{-1}$. The result is comparable with the rate constants measured for vancomycin and D-Ala-D-Ala interactions (5 $M^{-1}s^{-1}$).

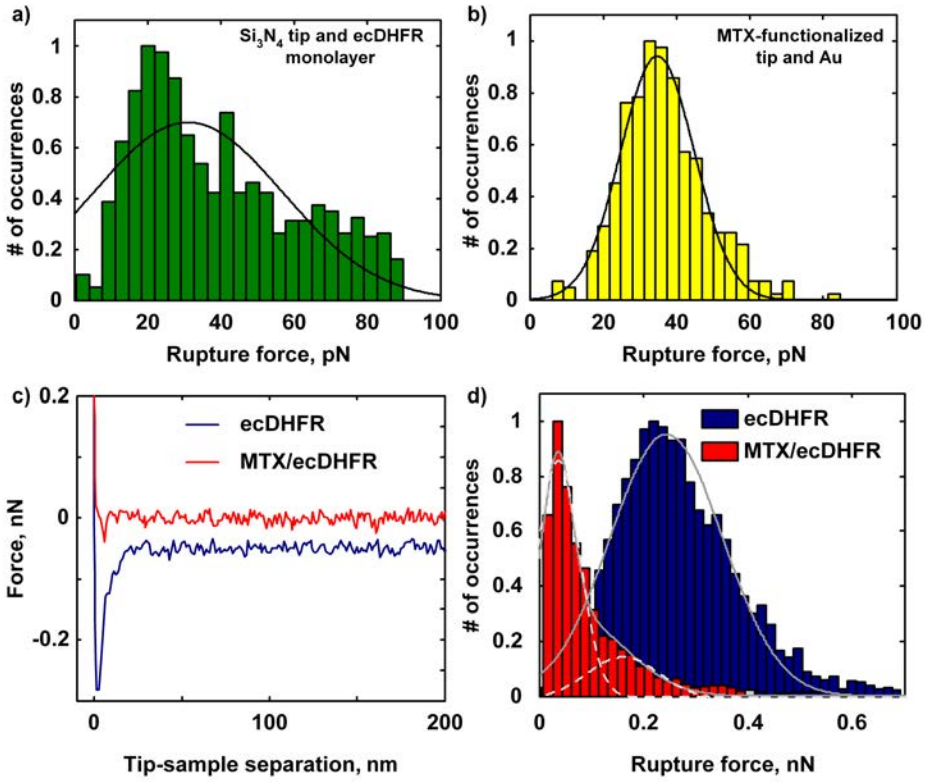

Figure 6.7. Distributions of rupture forces for control experiments a) unfunctionalized Si_3N_4 tip interacting with ecDHFR-functionalized gold and b) MTX-functionalized tip and a bare Au surface Solid lines are Gaussian fits. c) Representative force measurement (retract data only) of interactions between the enzyme and MTX-functionalized tip (blue), and MTX-bound enzyme with MTX-functionalized tip (red). d) Distributions of rupture forces for enzyme and MTX-functionalized tip (blue) and MTX-bound enzyme and MTX functionalized tip (red). All measurements collected at a dwell time of 510 ms and a velocity of 2 μm/sec. For measurements with the gold-bound ecDHFR, 4995 measurements were performed on two independent samples, Gaussian fit in gray. For control experiment wherein the MTX-blocked ecDHFR complex, 2304 measurements were performed on two independent samples. Individual Gaussian fits are shown with dashed lines, while the combined sum by solid gray line.

Fig. 6.7(a,b,c,d) shows representative force plots and the distribution of rupture forces measured for each experimental condition detailed above. The distributions are asymmetric, implying the occurrence of multiple binding events between MTX and ecDHFR.[156,188-190] Multiple-binding is probable since multiple MTX molecules are bound per tip and several enzyme molecules can be probed in the contact region between tip and substrate. Under the experimental conditions used herein, the estimated contact area includes 6 ecDHFR molecules, assuming the enzyme is a sphere 4 nm in diameter (Fig. 6.1). However, since the force-plot in Fig. 6.7c suggests a single rupture in each force measurement, it is likely that a single interaction between MTX and ecDHFR is ruptured per force measurement. The distribution of the interactions between DHFR and MTX, force measurements were fit to Gaussian distribution. The distributions for the control experiments for the Si_3N_4 and ecDHFR monolayer (Fig. 6.7a) and the MTX-functionalized tip and gold substrate show very weak rupture forces. Additionally, the interaction between the MTX blocked enzyme surface and MTX tip show much weaker interaction but similar asymmetric nature, and there is an appearance of a second distribution at higher forces, possibly due to unoccupied active sites, so a double Gaussian fit was used (Fig. 6.7d).

As expected, the bare Si_3N_4 tip shows little interaction between the ecDHFR monolayer, with a mean rupture force of 30 ± 25 pN (Fig. 6.7a), and similar small interactions are seen between an MTX-functionalized tip and the bare gold substrate (Fig. 6.7b). However, the interaction between the ecDHFR monolayer and the tip-bound MTX is substantially higher (mean rupture force of 245 ± 110 pN), indicating that a binding event has taken place between a tip-bound MTX and substrate-bound ecDHFR (Fig.

6.7d). A significantly reduced rupture force was measured between the tip-bound MTX and the gold-immobilized ecDHFR blocked by MTX, with an average value of 40 ± 20 pN with a second Gaussian distribution at 200 ± 100 pN. The second peak is similar to the specific MTX –DHFR interaction, suggesting that not all the active sites were blocked by MTX or, alternatively, the mechanical force induced by the AFM tip may remove MTX from the active site.[195] The significant difference in the rupture forces presented in Fig. 6.7c,d indicates that the interaction of the MTX-functionalized tip was mostly active-site specific with regard to the gold-immobilized ecDHFR. Therefore, with the MRFS technique described herein, one can distinguish with pico-Newton accuracy between active and inhibitor-bound enzyme. ecDHFR-MTX complex rupture forces are within the range of values excepted for receptor-ligand complexes. For example, streptavidin-biotin complex has a mean rupture force of 340 pN.[10] Comparatively,

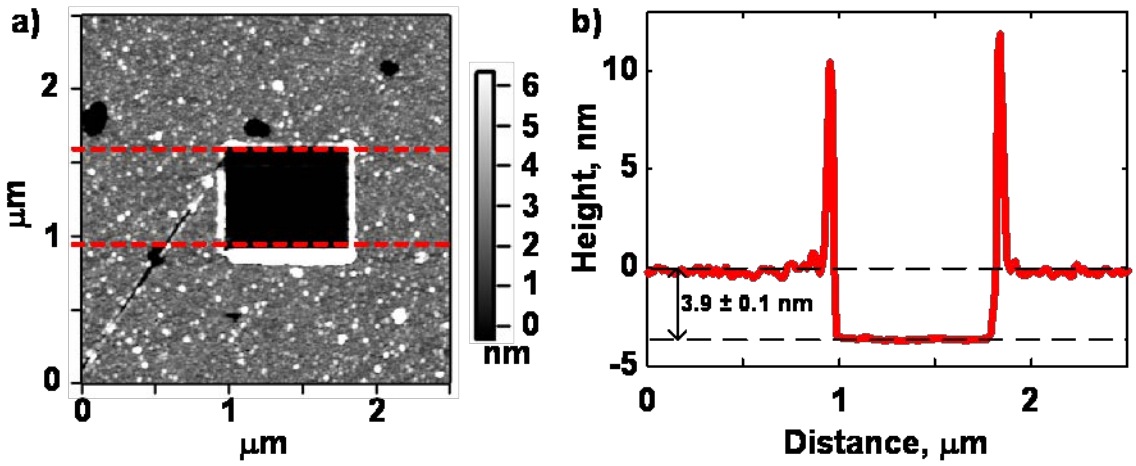

Figure 6.8. AFM height image of a) ecDHFR monolayer after treatment with 10 µM MTX in MTEN buffer (pH 7.5), center region has been scratched to examine monolayer thickness. b) Average cross section of the scratched region in (a).

vancomycin and D-Ala-D-Ala interaction strength is much weaker with a reported mean rupture force of 98 pN.[9] Additionally, the scratch tests performed after the treatment with MTX solution (Fig. 6.8), no changes in monolayer structure were observed. These tests further confirmed that the monolayer was stable throughout the MRFS measurements.

6.4 Conclusions

In summary, we have demonstrated the formation of a stable monolayer of active ecDHFR directly bound to an ultra-flat gold surface with limited disruption to the catalytic activity of the enzyme. Additionally, we have probed the rupture forces between the active-site of the immobilized enzyme and a tight-binding inhibitor, methotrexate. Our results indicate significant rupture forces (similar to streptavidin-biotin complex) upon dissociation of MTX from the enzyme's active site. Efforts are currently underway to extend these measurements to the natural substrates for ecDHFR (*i.e.* NADPH and dihydrofolate) to directly observe the forces involved with the dissociation of different enzymatic complexes. The SAM design described in this manuscript can be easily adapted for use with other enzymes provided a cysteine residue will be introduced onto the protein surface, away from the active site, *via* site directed mutagenesis. Natural surface reduced-cysteines will also have to be modified but these are rare, not conserved, and commonly should not affect activity. Introduction of a surface cysteine located away from the active-site in other enzymes will be used to evaluate the general applicability of the methodology developed here. If the ability of enzymes to form such functionalized monolayers will be found to be more general, enzymes catalyzing redox reactions will be tested.

CHAPTER 7

CONCLUSIONS AND FUTURE DIRECTIONS

The overall goal of this research has been to characterize the physical properties of materials and to develop further insight into processes such as electron transport in molecules and solids, electrochemical processes at the nanoscale, and ligand-receptor binding interactions. Probing interactions at this scale are complex and require the utilitization of the highly sensitive AFM. Future development of nanomaterials requires the further improvement of AFM to fully understand the utility and potential of these materials.

The work detailed in Chapter 2 encompasses monolayers of tetrathiafulvalene derivatives (TTF), wherein; the electrical properties were examined to determine how the contact geometry at metal-molecule-metal interfaces changes the properties of monolayer systems.[32,36] The results indicate that the self-assembled monolayers (SAMs) exhibit high electrical conductivity and a decrease in conductivity under compression. This lose of conductivity differs from typical results, and has potential applications as a mechanical switch. In this case, the material is conductive as small loading forces and exhibits a decrease in conductivity when the applied force is increased. The change in conductivity enables an on and off state to be alternated. Future work will focus on investigating molecules with functional groups that form new geometries at metal-molecule-metal junctions.[32]

Chapters 3 and 4 investigate the electrical properties of organic and metal-organic nanocrystals. The results demonstrated the tunable electrical properties of materials. In the case of tetrephenylethylene (TPE) molecules with a series of bispyridyl molecules, a

change in the composition of the pispyridyl molecules resulted in a lose of π overlap lead to a significant decrease in the electrical conductivity. Further research is being done to look at the crystallization of TPE molecules with additional bipyridines to impart different electrical properties. In chapter 4, variations in crystal compositions (i.e. silver counter ions), changed the solids from conductors to insulators. $[Ag_2(4stilbz)_4][CO_2CF_4]$ showed high electrical conductivity while a single crystal to single crystal (SCSC) reaction to form $[Ag_2(4\text{-pyr-ph-cb})_2][CO_2CF_4]$ increased the electrical conductivity of the material. Future work includes a systematic study on the impact of counter ions and organic ligands on the electrical conductivity of silver coordination complexes. Preliminary results suggest using a $SO_3CF_3^-$ anion imparts insulating properties, whereas, crystals with $CO_2CF_3^-$ anion show enhanced conductivity. The enhanced conductivity varies depending on the organic ligand in the coordination complex. These ongoing studies give valuable insight into the intermolecular interactions that facilitate electron transport in both organic and metal-organic solids.

Chapter 5 examines the redox processes of mixed monolayers of 1-decanethiol and 11-ferrocenyl-1-undecanethiol. The study specifically focused on localized environments and there impact of the oxidation of the 11-ferrocenyl-1-undecanethiol (Fc) molecules. By increasing the amount of Fc within monolayers, the molecules become depolarized and the ability to quantify the number of oxidized molecules decreases. A fundamental understanding of molecular environments on redox processes remains elusive, however, this work suggest the local environments of molecules strongly change the redox properties of molecules within monolayer. Future studies will strive to separate the force and dipole moment contributions to the trend observed in chapter 5. By using

ferrocene-terminated molecules of varying lengths, and therefore modulating the dipole moment of the molecules, the increase in force as a function of dipole moment can be quantified. Also, there are additional electroactive samples that can be probed. Preliminary results on ferrotin, a 24-subunit protein used for iron storage, show similar characteristics to Fc (i.e. increase in adhesion force at a positive bias of 2.5 Volts).[196-198] Significantly larger interaction forces between the probe and ferrotin sample have been observed, corresponding to roughly 250 oxidized iron atoms in the protein core. A fundamental understanding of electrochemical processes at the nanoscale can lead to the development of new and functional materials.

In chapter 6 the enzyme activity, binding, and interaction strength of gold bound dihydrofolate reductase (DHFR) and methotrexate (MTX) was measured using AFM. The results determined that by using a small linker we could readily investigate interactions between a probe immobilized ligand (MTX) and DHFR. Future work will investigate a variety of enzyme substrate interactions. Ongoing research on this project involves developing a protocol for the inclusion of a polyethylene glycol (PEG) linker between the tip and MTX; such a linker could enhance our detection of specific interaction. Inclusion of a longer PEG linker provides an additional separation distance between the tip and sample to identify a specific rupture.[153,199] This will allow us to characterize weaker interactions between different molecules, such as folate, and DHFR as well. Additionally literature demonstrates some enzyme mutations affect enzyme function and interactions. The impact of enzyme mutations on interaction strength is of interest and not yet studied. The ultimate goal being the development of a technique

wherein dynamic fluctuations of the enzyme can be monitored in real time using force spectroscopy.

In all chapters we use indentation to determine the Young's Modulus and contact area between the tip and sample. Current work in mechanical properties use one of two techniques, which vary based on the indenter and forces used in the study. In these studies, we used a nanoindenter (i.e. the AFM probe) to indent the sample using a small-applied force to cause elastic deformation.[106,107] The second indentation techniques use a larger pyramid-shaped macroindenter (typically berkovich indenter) and high forces (>500 nN) to inelastically deform the sample.[200-202] While these two techniques are widely used, no direct comparison has been completed. Future work will directly compare the Young's modulus of 4-chlorocinnamic acid determined using nanoindentation and macroindentation.

Understanding physical properties at the nanoscale is an ongoing focus of the research group. Probing and characterizing physical properties and interactions at the nanoscale using AFM is instrumental in accomplishing this goal. As the technique matures the ability to make precise measurements has evolved and lead to the discovery of unique physical properties. This work has focused on the electrical properties of monolayer systems (tetrathiafulvalene and decanethiol), organic and metal-organic semiconducting crystals (organic cocrystals and metal-organic complexes). Also, the electrochemical processes of mixed decanethiol and ferrocenyl-decanethiol monolayers, and lastly the measuring the strength of the specific interaction between the ligand-receptor complex, dihydrofolate reductase and methotrexate. Through these studies and the future endeavors of this work we hope to develop increased understanding of

nanoscale interactions and processes which can be functional in a broad range of applications.

REFERENCES

(1) Alessandrini, A.; Facci, P. *Meas Sci Technol* **2005**, *16*, R65.

(2) Zavala, G. *Colloid. Polym. Sci.* **2008**, *286*, 85.

(3) Hoppe, H.; Niggemann, M.; Winder, C.; Kraut, J.; Hiesgen, R.; Hinsch, A.; Meissner, D.; Sariciftci, N. S. *Adv. Funct. Mater.* **2004**, *14*, 1005.

(4) Wold, D. J.; Frisbie, C. D. *J. Am. Chem. Soc.* **2001**, *123*, 5549.

(5) Guo, S.; Akhremitchev, B. B. *Langmuir* **2008**, *24*, 880.

(6) Fu, L.; Liu, X.; Zhang, Y.; Dravid, V. P.; Mirkin, C. A. *Nano Lett.* **2003**, *3*, 757.

(7) Kinsella, J. M.; Ivanisevic, A. *Langmuir* **2007**, *23*, 3886.

(8) Li, Y.; Maynor, B. W.; Liu, J. *J. Am. Chem. Soc.* **2001**, *123*, 2105.

(9) Gilbert, Y.; Deghorain, M.; Wang, L.; Xu, B.; Pollheimer, P. D.; Gruber, H. J.; Errington, J.; Hallet, B.; Haulot, X.; Verbelen, C.; Hols, P.; Dufrene, Y. F. *Nano Lett.* **2007**, *7*, 796.

(10) Lee, G. U.; Kidwell, D. A.; Colton, R. J. *Langmuir* **1994**, *10*, 354.

(11) Linke, W.; Grützner, A. *Pflügers Archiv European Journal of Physiology* **2008**, *456*, 101.

(12) Gross, L.; Mohn, F.; Moll, N.; Liljeroth, P.; Meyer, G. *Science* **2009**, *325*, 1110.

(13) Mori, T.; Asakura, M.; Okahata, Y. *J. Am. Chem. Soc.* **2011**, *133*, 5701.

(14) Hinterdorfer, P.; Dufrene, Y. F. *Nat Methods* **2006**, *3*, 347.

(15) Binnig, G.; Quate, C. F.; Gerber, C. *Phys. Rev. Lett.* **1986**, *56*, 930.

(16) Binnig, G.; Rohrer, H.; Gerber, C.; Weibel, E. *Phys. Rev. Lett.* **1982**, *49*, 57.

(17) Lee, S.-w.; Sigmund, W. M. *Colloids and Surfaces A: Physicochemical and Engineering Aspects* **2002**, *204*, 43.

(18) Boland, T.; Ratner, B. D. *P Natl Acad Sci USA* **1995**, *92*, 5297.

(19) Grandbois, M.; Beyer, M.; Rief, M.; Clausen-Schaumann, H.; Gaub, H. E. *Science* **1999**, *283*, 1727.

(20) Tivanski, A. V.; Li, J. K.; Walker, G. C. *Langmuir* **2008**, *24*, 2288.

(21) Holmlin, R. E.; Haag, R.; Chabinyc, M. L.; Ismagilov, R. F.; Cohen, A. E.; Terfort, A.; Rampi, M. A.; Whitesides, G. M. *J. Am. Chem. Soc.* **2001**, *123*, 5075.

(22) Lu, X.; Li, M.; Yang, C.; Zhang, L.; Li, Y.; Jiang, L.; Li, H.; Jiang, L.; Liu, C.; Hu, W. *Langmuir* **2006**, *22*, 3035.

(23) Rampi, M. A.; Whitesides, G. M. *Chem. Phys.* **2002**, *281*, 373.

(24) Reed, M. A.; Zhou, C.; Deshpande, M. R.; Muller, C. J.; Burgin, T. P.; Jones, L.; Tour, J. M. *Ann. N.Y. Acad. Sci.* **1998**, *852*, 133.

(25) Van Hal, P. A.; Smits, E. C. P.; Geuns, T. C. T.; Akkerman, H. B.; De Brito, B. C.; Perissinotto, S.; Lanzani, G.; Kronemeijer, A. J.; Geskin, V.; Cornil, J.; Blom, P. W. M.; De Boer, B.; De Leeuw, D. M. *Nat. Nano.* **2008**, *3*, 749.

(26) Wynn, C. M.; Fedynyshyn, T. H.; Geis, M. W.; Kunz, R. R.; Lyszczarz, T. M.; Rothschild, M.; Spector, S. J.; Switkes, M. *Nanotechnology* **2004**, *15*, 86.

(27) Burtman, V.; Ndobe, A. S.; Vardeny, Z. V. *J. Appl. Phys.* **2005**, *98*.

(28) Francesco, G. M. n., H.; Lucia, G.; Ma, T. G.; Michel, C.; Christian, S.; Carlos, R. A.; Gabino, R. B.; Marisela, V.; Nicolas, A.; Nazario, M. *Chem. Commun.* **2007**, 4854.

(29) Ogawa, T. K., K.; Masuda, G.; Takase, T.; Shimizu, Y.; Maeda, S. *Trans. Mater. Res. Soc. Jpn.* **2001**, *26*, 733.

(30) Wang, J.-L.; Tang, Z.-M.; Xiao, Q.; Zhou, Q.-F.; Ma, Y.; Pei, J. *Org. Lett.* **2007**, *10*, 17.

(31) Gomar-Nadal, E.; Ramachandran, G. K.; Chen, F.; Burgin, T.; Rovira, C.; Amabilino, D. B.; Lindsay, S. M. *J. Phys. Chem. B* **2004**, *108*, 7213.

(32) Tivanski, A. V.; He, Y.; Borguet, E.; Liu, H.; Walker, G. C.; Waldeck, D. H. *J. Phys. Chem. B* **2005**, *109*, 5398.

(33) Joachim, C.; Ratner, M. A. *P Natl Acad Sci USA* **2005**, *102*, 8801.

(34) Nitzan, A.; Ratner, M. A. *Science* **2003**, *300*, 1384.

(35) Akkerman, H. B.; Blom, P. W. M.; de Leeuw, D. M.; de Boer, B. *Nature* **2006**, *441*, 69.

(36) Li, Z.; Kosov, D. S. *J. Phys. Chem. B* **2006**, *110*, 19116.

(37) Herranz, M. Å.; Sanchez, L.; Marten, N. *Phosphorus, Sulfur, and Silicon and the Related Elements* **2005**, *180*, 1133.

(38) Segura, J. L.; Martín, N. *Angewandte Chemie International Edition* **2001**, *40*, 1372.

(39) Simonsen, K. B.; Svenstrup, N.; Lau, J.; Simonsen, O.; Mork, P.; Kristensen, G. J.; Becher, J. *Synthesis-Stuttgart* **1996**, 407.

(40) Svenstrup, N.; Rasmussen, K. M.; Hansen, T. K.; Becher, J. *Synthesis-Stuttgart* **1994**, 809.

(41) Engelkes, V. B.; Beebe, J. M.; Frisbie, C. D. *J. Phys. Chem. B* **2005**, *109*, 16801.

(42) Wold, D. J.; Frisbie, C. D. *J. Am. Chem. Soc.* **2001**, *123*, 5549.

(43) Wagner, P.; Hegner, M.; Guentherodt, H.-J.; Semenza, G. *Langmuir* **1995**, *11*, 3867.

(44) Hutter, J. L.; Bechhoefer, J. *Rev Sci Instrum* **1993**, *64*, 1868.

(45) Beebe, J. M.; Engelkes, V. B.; Liu, J.; Gooding, J. J.; Eggers, P. K.; Jun, Y.; Zhu, X.; Paddon-Row, M. N.; Frisbie, C. D. *J. Phys. Chem. B* **2005**, *109*, 5207.

(46) O'Dwyer, C.; Gay, G.; Viaris de Lesegno, B.; Weiner, J. *Langmuir* **2004**, *20*, 8172.

(47) Tamada, K.; Hara, M.; Sasabe, H.; Knoll, W. *Langmuir* **1997**, *13*, 1558.

(48) Bain, C. D.; Troughton, E. B.; Tao, Y. T.; Evall, J.; Whitesides, G. M.; Nuzzo, R. G. *J. Am. Chem. Soc.* **1989**, *111*, 321.

(49) Ehler, T. T.; Malmberg, N.; Noe, L. J. *J. Phys. Chem. B* **1997**, *101*, 1268.

(50) Nuzzo, R. G.; Dubois, L. H.; Allara, D. L. *J. Am. Chem. Soc.* **1990**, *112*, 558.

(51) Porter, M. D.; Bright, T. B.; Allara, D. L.; Chidsey, C. E. D. *J. Am. Chem. Soc.* **1987**, *109*, 3559.

(52) Tian, W. D.; Datta, S.; Hong, S. H.; Reifenberger, R.; Henderson, J. I.; Kubiak, C. P. *J. Chem. Phys.* **1998**, *109*, 2874.

(53) Wold, D. J.; Frisbie, C. D. *J. Am. Chem. Soc.* **2000**, *122*, 2970.

(54) Davis, J. J.; Peters, B.; Xi, W. *J. Phys. Condens. Matter* **2008**, *20*, 374123.

(55) Simmons, J. G. *J. Appl. Phys.* **1963**, *34*, 1793.

(56) Sze, S. M. **1891**.

(57) Wang, W.; Lee, T.; Reed, M. A. *Phys Rev B* **2003**, *68*, 035416.

(58) Burnham, N. A.; Colton, R. J. *J Vac Sci Technol A* **1989**, *7*, 2906.

(59) Weihs, T. P.; Nawaz, Z.; Jarvis, S. P.; Pethica, J. B. *Appl. Phys. Lett.* **1991**, *59*, 3536.

(60) Gosvami, N. N.; Sinha, S. K.; Srinivasan, M. P.; O'Shea, S. J. *J. Phys. Chem. C* **2007**, *112*, 297.

(61) Ishida, T.; Mizutani, W.; Aya, Y.; Ogiso, H.; Sasaki, S.; Tokumoto, H. *J. Phys. Chem. B* **2002**, *106*, 5886.

(62) Lee, T.; Wang, W.; Klemic, J. F.; Zhang, J. J.; Su, J.; Reed, M. A. *J. Phys. Chem. B* **2004**, *108*, 8742.

(63) Vilan, A. *J. Phys. Chem. C* **2007**, *111*, 4431.

(64) Yokota, Y.; Fukui, K.-i.; Enoki, T.; Hara, M. *J. Am. Chem. Soc.* **2007**, *129*, 6571.

(65) Magoga, M.; Joachim, C. *Phys Rev B* **1999**, *59*, 16011.

(66) Desiraju, G. R. *Crystal Engineering – The Design of Organic Solids*; Elsevier, Amsterdam, 1989.

(67) Pigge, F. C. *Crystengcomm* **2011**, *13*, 1733.

(68) Tiekink, E. R. T.; Vittal, J. *Frontiers in Cystal Engineering*; John Wiley & Sons, Chichester, 2006.

(69) Bryce, M. R. *J. Mater. Chem.* **1995**, *5*, 1481.

(70) Fourmigue, M.; Batail, P. *Chem. Rev.* **2004**, *104*, 5379.

(71) Anthony, J. E. *Chem. Rev.* **2006**, *106*, 5028.

(72) Anthony, J. E. *Angewandte Chemie-International Edition* **2008**, *47*, 452.

(73) Baudron, S. A.; Avarvari, N.; Batail, P.; Coulon, C.; Clerac, R.; Canadell, E.; Auban-Senzier, P. *J. Am. Chem. Soc.* **2003**, *125*, 11583.

(74) Gsänger, M.; Oh, J.; Könemann, M.; Höffken, H.; Krause, A.-M.; Bao, Z.; *Angew. Chem. Int. Ed.* **2010**, *49*, 740.

(75) Lopez, J. L.; Atienza, C.; Seitz, W.; Guldi, D. M.; Martin, N. *Angewandte Chemie-International Edition* **2010**, *49*, 9876.

(76) Moon, H.; Zeis, R.; Borkent, E. J.; Besnard, C.; Lovinger, A. J.; Siegrist, T.; Kloc, C.; Bao, Z. N. *J. Am. Chem. Soc.* **2004**, *126*, 15322.

(77) Murata, T.; Morita, Y.; Fukui, K.; Sato, K.; Shiomi, D.; Takui, T.; Maesato, M.; Yamochi, H.; Saito, G.; Nakasuji, K. *Angewandte Chemie-International Edition* **2004**, *43*, 6343.

(78) Murata, T.; Morita, Y.; Yakiyama, Y.; Fukui, K.; Yarnochi, H.; Saito, G.; Nakasuji, K. *J. Am. Chem. Soc.* **2007**, *129*, 10837.

(79) Payne, M. M.; Parkin, S. R.; Anthony, J. E.; Kuo, C. C.; Jackson, T. N. *J. Am. Chem. Soc.* **2005**, *127*, 4986.

(80) Sokolov, A. N.; Friscic, T.; MacGillivray, L. R. *J. Am. Chem. Soc.* **2006**, *128*, 2806.

(81) Banerjee, M.; Emond, S. J.; Lindeman, S. V.; Rathore, R. *J. Org. Chem.* **2007**, *72*, 8054.

(82) Hong, Y. N.; Lam, J. W. Y.; Tang, B. Z. *Chem. Commun.* **2009**, 4332.

(83) Hünig, S.; Kemmer, M.; Wenner, H.; Barbosa, F.; Gescheidt, G.; Perepichka, I. F.; Bäuerle, P.; Emge, A.; Peters, K.; (2000), C. E. J., 6: 2618–2632. *Chem. Eur. J.* **2000**, *6*.

(84) Mori, T.; Inoue, Y. *J Phys Chem A* **2005**, *109*, 2728.

(85) Schreivogel, A.; Maurer, J.; Winter, R.; Baro, A.; Laschat, S. *Eur. J. Org. Chem.* **2006**, 3395.

(86) Wolf, M. O.; Fox, H. H.; Fox, M. A. *J. Org. Chem.* **1996**, *61*, 287.

(87) Kapadia, P. P.; Ditzler, L. R.; Baltrusaitis, J.; Swenson, D. C.; Tivanski, A. V.; Pigge, F. C. *J. Am. Chem. Soc.* **2011**, *133*, 8490.

(88) Becke, A. D. *J. Chem. Phys.* **1993**, *98*, 5648.

(89) Lee, C. T.; Yang, W. T.; Parr, R. G. *Phys Rev B* **1988**, *37*, 785.

(90) Gatti, C.; Saunders, V. R.; Roetti, C. *J. Chem. Phys.* **1994**, *101*, 10686.

(91) Civalleri, B.; D'Arco, P.; Orlando, R.; Saunders, V. R.; Dovesi, R. *Chem. Phys. Lett.* **2001**, *348*, 131.

(92) Doll, K. *Comput. Phys. Commun.* **2001**, *137*, 74.

(93) Doll, K.; Saunders, V. R.; Harrison, N. M. *Int. J. Quantum Chem.* **2001**, *82*, 1.

(94) Broyden, C. G. *IMA J. Appl. Math.* **1970**, *6*, 76.

(95) Fletcher, R. *Computer Journal* **1970** *13*, 317.

(96) Goldfarb, D. *Math Comput* **1970**, *24*, 23.

(97) Shanno, D. F. *Math Comput* **1970**, *24*, 647.

(98) Dovesi, R. O., R.; Civalleri, B.; Roetti, C.; Saunders, V. R.; Zicovich-Wilson, C. M. *Z. Kristallographie* **2005**, *220*, 571.

(99) Dovesi, R. S., V. R.; Roetti, R.; Orlando, R.; Zicovich-Wilson, C. M.; Pascale, F.; Civalleri, B.; Doll, K.; Harrison, N. M.; Bush, I. J.; D'Arco, P.; Llunell, M. *CRYSTAL'09* University of Torino, Torino, Italy.

(100) Schultz, A.; Diele, S.; Laschat, S.; Nimtz, M., Novel Columnar Tetraphenylethenes via McMurry Coupling. Adv. Funct. Mater., 11: 441–446. *Adv. Funct. Mater.* **2001**, 441.

(101) Rathore, R.; Lindeman, S. V.; Kumar, A. S.; Kochi, J. K. *J. Am. Chem. Soc.* **1998**, *120*, 6931.

(102) Dovesi, R.; Saunders, V. R.; Roetti, R.; Orlando, R.; Zicovich-Wilson, C. M.; Pascale, F.; Civalleri, B.; Doll, K.; Harrison, N. M.; Bush, I. J.; D'Arco, P.; Llunell, M. *CRYSTAL'09* University of Torino: Torino, Italy, 2009.

(103) Ditzler, L. R.; Karunatilaka, C.; Donuru, V. R.; Liu, H. Y.; Tivanski, A. V. *J. Phys. Chem. C* **2010**, *114*, 4429.

(104) Gomar-Nadal, E.; Ramachandran, G. K.; Chen, F.; Burgin, T.; Rovira, C.; Amabilino, D. B.; Lindsay, S. M. *J. Phys. Chem. B* **2004**, *108*, 7213.

(105) *Synth. Diamond: Emerging CVD Sci. Technol.* ; Wiley: New York, N. Y, 1994.

(106) Guo, S.; Akhremitchev, B. B. *Langmuir* **2007**, *24*, 880.

(107) Karunatilaka, C.; Bučar, D.-K.; Ditzler, L. R.; Friščić, T.; Swenson, D. C.; MacGillivray, L. R.; Tivanski, A. V. *Angewandte Chemie* **2011**, *123*, 8801.

(108) Masterson, V. M.; Cao, X. *Int. J. Pharm.* **2008**, *362*, 163.

(109) Tait, S.; White, E. T.; Litster, J. D. *Part. Part. Syst. Char.* **2008**, *25*, 266.

(110) Coropceanu, V.; Cornil, J. r. m.; da Silva Filho, D. A.; Olivier, Y.; Silbey, R.; Bradas, J.-L. *Chem. Rev.* **2007**, *107*, 926.

(111) Kao, K. C.; Hwang, W. *Electrical Transport in Solids*; Pergamon: Oxford, 1981.

(112) Brown, A. R.; de Leeuw, D. M.; Havinga, E. E.; Pomp, A. *Synth. Met.* **1994**, *68*, 65.

(113) Paasch, G.; Lindner, T.; Scheinert, S. *Synth. Met.* **2002**, *132*, 97.

(114) Molinari, A. S.; Alves, H.; Chen, Z.; Facchetti, A.; Morpurgo, A. F. *J. Am. Chem. Soc.* **2009**, *131*, 2462.

(115) Miao, Q.; Chi, X.; Xiao, S.; Zeis, R.; Lefenfeld, M.; Siegrist, T.; Steigerwald, M. L.; Nuckolls, C. *J. Am. Chem. Soc.* **2006**, *128*, 1340.

(116) Morita, Y.; Murata, T.; Fukui, K.; Yamada, S.; Sato, K.; Shiomi, D.; Takui, T.; Kitagawa, H.; Yamochi, H.; Saito, G.; Nakasuji, K. *J. Org. Chem.* **2005**, *70*, 2739.

(117) Desiraju, G. R. *J. Chem. Sci.* **2010**, *122*, 667.

(118) Braga, D.; D'Addario, D.; Giaffreda, S. L.; Maini, L.; Polito, M.; Grepioni, F. *Organic Solid State Reactions* **2005**, *254*, 71.

(119) Barbour, L. J. *Chem. Commun.* **2006**, 1163.

(120) Haynes, D. A. *Crystengcomm* **2011**, *13*, 4793.

(121) Xu, Z. *Coord. Chem. Rev.* **2006**, *250*, 2745.

(122) Zheng, S. L.; Zhang, J. P.; Wong, W. T.; Chen, X. M. *J. Am. Chem. Soc.* **2003**, *125*, 6882.

(123) Gao, J. H.; Xu, B. *Nano Today* **2009**, *4*, 281.

(124) An, B. K.; Gihm, S. H.; Chung, J. W.; Park, C. R.; Kwon, S. K.; Park, S. Y. *J. Am. Chem. Soc.* **2009**, *131*, 3950.

(125) Yao, Y. S.; Shen, W. T.; Nohra, B.; Lescop, C.; Reau, R. *Chem-Eur J* **2010**, *16*, 7143.

(126) Chu, Q. L.; Swenson, D. C.; MacGillivray, L. R. *Angewandte Chemie-International Edition* **2005**, *44*, 3569.

(127) Sander, J. R. G.; Bucar, D. K.; Henry, R. F.; Zhang, G. G. Z.; MacGillivray, L. R. *Angewandte Chemie-International Edition* **2010**, *49*, 7284.

(128) Kelley, T. W.; Frisbie, C. D. *J Vac Sci Technol B* **2000**, *18*, 632.

(129) Palermo, V.; Liscio, A.; Palma, M.; Surin, M.; Lazzaroni, R.; Samori, P. *Chem. Commun.* **2007**, 3326.

(130) Reid, O. G.; Munechika, K.; Ginger, D. S. *Nano Lett.* **2008**, *8*, 1602.

(131) Burda, C.; Chen, X. B.; Narayanan, R.; El-Sayed, M. A. *Chem. Rev.* **2005**, *105*, 1025.

(132) Bang, J. H.; Suslick, K. S. *Adv. Mater.* **2010**, *22*, 1039.

(133) Bucar, D. K.; MacGillivray, L. R. *J. Am. Chem. Soc.* **2007**, *129*, 32.

(134) Barbour, L. J. *Aust. J. Chem.* **2006**, *59*, 595.

(135) Sun, J.; Dai, F. N.; Yuan, W. B.; Bi, W. H.; Zhao, X. L.; Sun, W. M.; Sun, D. F. *Angewandte Chemie-International Edition* **2011**, *50*, 7061.

(136) Munakata, M.; Wu, L. P.; KurodaSowa, T.; Maekawa, M.; Suenaga, Y.; Sugimoto, K. *Inorg. Chem.* **1997**, *36*, 4903.

(137) Liu, S. Q.; Kuroda-Sowa, T.; Konaka, H.; Suenaga, Y.; Maekawa, M.; Mizutani, T.; Ning, G. L.; Munakata, M. *Inorg. Chem.* **2005**, *44*, 1031.

(138) Rawlett, A. M.; Hopson, T. J.; Nagahara, L. A.; Tsui, R. K.; Ramachandran, G. K.; Lindsay, S. M. *Appl. Phys. Lett.* **2002**, *81*, 3043.

(139) Tivanski, A. V.; Walker, G. C. *J. Am. Chem. Soc.* **2005**, *127*, 7647.

(140) Lee, L. Y. S.; Sutherland, T. C.; Rucareanu, S.; Lennox, R. B. *Langmuir* **2006**, *22*, 4438.

(141) Watcharinyanon, S.; Moons, E.; Johansson, L. S. O. *J. Phys. Chem. C* **2009**, *113*, 1972.

(142) Fujii, S.; Kurokawa, S.; Murase, K.; Lee, K. H.; Sakai, A.; Sugimura, H. *Electrochim. Acta* **2007**, *52*, 4436.

(143) Chidsey, C. E. D.; Bertozzi, C. R.; Putvinski, T. M.; Mujsce, A. M. *J. Am. Chem. Soc.* **1990**, *112*, 4301.

(144) Ditzler, L. R.; Karunatilaka, C.; Donuru, V. R.; Liu, H. Y.; Tivanski, A. V. *J. Phys. Chem. C* **2010**, *114*, 4429.

(145) Tivanski, A. V.; Bemis, J. E.; Akhremitchev, B. B.; Liu, H. Y.; Walker, G. C. *Langmuir* **2003**, *19*, 1929.

(146) Yokota, Y.; Fukui, K.; Enoki, T.; Hara, M. *J. Phys. Chem. C* **2007**, *111*, 7561.

(147) Sacha, G. M.; Sahagun, E.; Saenz, J. J. *J. Appl. Phys.* **2007**, *101*.

(148) Asadi, K.; Gholamrezaie, F.; Smits, E. C. P.; Blom, P. W. M.; de Boer, B. *J. Mater. Chem.* **2007**, *17*, 1947.

(149) Thomas, R. C.; Tangyunyong, P.; Houston, J. E.; Michalske, T. A.; Crooks, R. M. *J Phys Chem* **1994**, *98*, 4493.

(150) Sushko, M. L.; Shluger, A. L. *Adv. Funct. Mater.* **2008**, *18*, 2228.

(151) Schaadt, D. M.; Yu, E. T.; Sankar, S.; Berkowitz, A. E. *Appl. Phys. Lett.* **1999**, *74*, 472.

(152) Ray, C.; Brown, J. R.; Akhremitchev, B. B. *Langmuir* **2007**, *23*, 6076.

(153) Dufrene, Y. F.; Hinterdorfer, P. *Pflugers Archiv - European Journal of Physiology* **2008**, *256*, 237.

(154) Cecconi, C.; Shank, E.; Dahlquist, F.; Marqusee, S.; Bustamante, C. *Eur. Biophys. J.* **2008**, *37*, 729.

(155) Ebner, A.; Hinterdorfer, P.; Gruber, H. J. *Ultramicroscopy* **2007**, *107*, 922.

(156) Touhami, A.; Jericho, M. H.; Beveridge, T. J. *Langmuir* **2007**, *23*, 2755.

(157) Moffitt, J. R.; Chemla, Y. R.; Smith, S. B.; Bustamante, C. *Annu. Rev. Biochem.* **2008**, *77*, 205.

(158) Ratto, T. V.; Langry, K. C.; Rudd, R. E.; Balhorn, R. L.; Allen, M. J.; McElfresh, M. W. *Biophys. J.* **2004**, *86*, 2430.

(159) Xu, D.; Watt, G. D.; Harb, J. N.; Davis, R. C. *Nano Lett.* **2005**, *5*, 571.

(160) Alonso-Lomillo, M. A.; Rudiger, O.; Maroto-Valiente, A.; Velez, M.; Rodriguez-Ramos, I.; Munoz, F. J.; Fernandez, V. M.; De Lacey, A. L. *Nano Lett.* **2007**, *7*, 1603.

(161) Rüdiger, O.; Abad, J. M.; Hatchikian, E. C.; Fernandez, V. M.; De Lacey, A. L. *J. Am. Chem. Soc.* **2005**, *127*, 16008.

(162) Sawaya, M. R.; Kraut, J. *Biochemistry* **1997**, *36*, 586.

(163) Benkovic, S. J.; Hammes-Schiffer, S. *Annu. Rev. Biochem.* **2006**, *75*, 519.

(164) Clementi, C.; Jennings, P. A.; Onuchic, J. N. *P Natl Acad Sci USA* **2000**, *97*, 5871.

(165) Wang, L.; Goodey, N.; Benkovic, S. J.; Kohen, A. *P Natl Acad Sci USA* **2006**, *103*, 15753.

(166) Schnell, J. R.; Dyson, H. J.; Wright, P. E. *Annual Reviews of Biophysics and Biomolecular Structure* **2004**, *33*, 119.

(167) McElheny, D.; Schnell, J. R.; Lansing, J. C.; Dyson, H. J.; Wright, P. E. *P Natl Acad Sci USA* **2005**, *102*, 5032.

(168) Boehr, D. B.; McElheny, D.; Dyson, H. J.; Wright, P. E. *Science* **2006**, *313*, 1638.

(169) Pu, J.; Garcia-Viloca, M.; Gao, J.; Truhlar, D. G.; Kohen, A. *J. Am. Chem. Soc.* **2005**, *127*, 14879.

(170) Garcia-Viloca, M.; Truhlar, D. G.; Gao, J. *Biochemistry* **2003**, *42*, 13558.

(171) Kohler, N.; Fryxell, G. E.; Zhang, M. *J. Am. Chem. Soc.* **2004**, *126*, 7206.

(172) Kohler, N.; Sun, C.; Wang, J.; Zhang, M. Q. *Langmuir* **2005**, *21*, 8858.

(173) Shank, E. A.; Cecconi, C.; Dill, J. W.; Marqusee, S.; Bustamante, C. *Nature* **2010**, *465*, 637.

(174) Reiner, C. K.; Stroh, C. M.; Ebner, A.; Klampf, C.; Gall, A. A.; Romanin, C.; Lyubchenko, Y. L.; Hinterdorfer, P.; Gruber, H. J. *Anal. Chim. Acta* **2003**, *479*, 59.

(175) Willemsen, O. H.; Snel, M. M. E.; van der Werf, K. O.; de Grooth, B. G.; Greve, J.; Hinterdorfer, P.; Gruber, H. J.; Schindler, H.; van Kooyk, Y.; Figdor, C. G. *Biophys. J.* **1998**, *75*, 2220.

(176) Zhou, H. X.; Batra, J.; Xu, K.; Qin, S. B. *Biophys. J.* **2009**, *97*, 906.

(177) Boehr, D. B.; Nussinov, R.; Wright, P. E. *Nat. Chem. Biol.* **2009**, *5*, 789.

(178) Nagel, Z. D.; Klinman, J. P. *Nat. Chem. Biol.* **2009**, *5*, 543.

(179) Sasaki, Y. C.; Yasuda, K.; Suzuki, Y.; Ishibashi, T.; Satoh, I.; Fujiki, Y.; Ishiwata, S. *Biophys. J.* **1997**, *72*, 1842.

(180) Cameron, C. E.; Benkovic, S. J. *Biochemistry* **1997**, *36*, 15792.

(181) Markham, K. A.; Sikorski, R. S.; Kohen, A. *Anal. Biochem.* **2003**, *322*, 26.

(182) Blakley, R. L. *Nature* **1960**, *188*, 231.

(183) Porter-Peden, L.; Kamper, S. G.; Vander Wal, M.; Blankespoor, R.; Sinniah, K. *Langmuir* **2008**, *24*, 11556.

(184) Roes, S.; Mumm, F.; Seydel, U.; Gutsmann, T. *J. Biol. Chem.* **2006**, *281*, 2757.

(185) Klein, D. C. G.; Stroh, C. M.; Jensenius, H.; van Es, M.; Kamruzzahan, A. S. M.; Stamouli, A.; Gruber, H. J.; Oosterkamp, T. H.; Hinterdorfer, P. *ChemPhysChem* **2003**, *4*, 1367.

(186) Rigby-Singleton, S. M.; Allen, S.; Davies, M. C.; Roberts, C. J.; Tendler, S. J. B.; Williams, P. M. *J. Chem. Soc., Perkin Trans. 2* **2002**, 1722.

(187) Ainavarapu, S. R. K.; Li, L. Y.; Badilla, C. L.; Fernandez, J. M. *Biophys. J.* **2005**, *89*, 3337.

(188) Touhami, A.; Hoffmann, B.; Vasella, A.; Denis, F. A.; Dufrene, Y. F. *Microbiology* **2003**, *149*, 2873.

(189) Sotres, J.; Lostao, A.; Wildling, L.; Ebner, A.; Gomez-Moreno, C.; Gruber, H. J.; Hinterdorfer, P.; Baro, A. M. *ChemPhysChem* **2008**, *9*, 590.

(190) Bizzarri, A. R.; Cannistraro, S. *J. Phys. Chem. B* **2009**, *113*, 16449.

(191) Khan, A.; Philip, J.; Hess, P. *J. Appl. Phys.* **2004**, *95*, 1667.

(192) Guo, S.; Akhremitchev, B. B. *Langmuir* **2007**, *24*, 880.

(193) Hanefeld, U. In *Modern Biocatalysis: Stereoselective and Environmentally Friendly Reactions*; Fessner, W.-D., Anthonson, T., Eds.; Wiley-VCH Verlag GmbH & Co. KGaA: Weinheim, 2009, p 21.

(194) Fierke, C. A.; Johnson, K. A.; Benkovic, S. J. *Biochemistry* **1987**, *26*, 4085.

(195) Guo, S. L.; Li, N.; Lad, N.; Ray, C.; Akhremitchev, B. B. *J. Am. Chem. Soc.* **2010**, *132*, 9681.

(196) Dominguez-Vera, J. M.; Welte, L.; Galvez, N.; Fernandez, B.; Gomez-Herrero, J.; Zamora, F. *Nanotechnology* **2008**, *19*.

(197) Tang, Q.; Moon, H. K.; Lee, Y.; Yoon, S. M.; Song, H. J.; Lim, H.; Choi, H. C. *J. Am. Chem. Soc.* **2007**, *129*, 11018.

(198) Xu, D. G.; Watt, G. D.; Harb, J. N.; Davis, R. C. *Nano Lett.* **2005**, *5*, 571.

(199) Guo, S.; Lad, N.; Ray, C.; Akhremitchev, B. B. *Biophys. J.* **2009**, *96*, 3412.

(200) Chow, E. H. H.; Bucar, D.-K.; Jones, W. *Chem. Commun.* **2012**.

(201) Kiran, M. S. R. N.; Varughese, S.; Reddy, C. M.; Ramamurty, U.; Desiraju, G. R. *Cryst Growth Des* **2010**, *10*, 4650.

(202) Perkins, M. C.; Bunker, M.; James, J.; Rigby-Singleton, S.; Ledru, J.; Madden-Smith, C.; Luk, S.; Patel, N.; Roberts, C. J. *European Journal of Pharmaceutical Sciences* **2009**, *38*, 1.